

Characteristics, origins, and biosignature preservation potential of carbonate-bearing rocks within and outside of Jezero crater

J.D. Tarnas¹, K.M. Stack¹, M. Parente², A.H.D. Koepfel³, J.F. Mustard⁴, K.R. Moore¹, B.H.N. Horgan⁵, F.P. Seelos⁶, E.A. Cloutis⁷, P.B. Kelemen⁸, D. Flannery⁹, A.J. Brown¹⁰, K.R. Frizzell¹¹, P. Pinet¹²

¹NASA Jet Propulsion Laboratory, California Institute of Technology, ²University of Massachusetts at Amherst Department of Electrical and Computer Engineering, ³Northern Arizona University, Department of Astronomy and Planetary Science, ⁴Brown University Department of Earth, Environmental and Planetary Sciences, ⁵Purdue University Department of Earth, Atmospheric, and Planetary Sciences, ⁶Johns Hopkins University Applied Physics Lab, ⁷University of Winnipeg Department of Geography, ⁸Columbia University Lamont-Doherty Earth Observatory, ⁹Queensland University of Technology School of Earth and Atmospheric Sciences, ¹⁰Plancius Research, Severna Park, MD, ¹¹Rutgers University Department of Earth and Planetary Sciences, ¹²Institut de Recherche en Astrophysique et Planétologie.

Abstract

Carbonate minerals have been detected in Jezero crater, an ancient lake basin that is the landing site of the Mars 2020 Perseverance rover, and within the regional olivine-bearing (ROB) unit in the Nili Fossae region surrounding this crater. It has been suggested that some carbonates in the margin fractured unit, a rock unit within Jezero crater, formed in a

This article has been accepted for publication and undergone full peer review but has not been through the copyediting, typesetting, pagination and proofreading process, which may lead to differences between this version and the [Version of Record](#). Please cite this article as doi: [10.1029/2021JE006898](https://doi.org/10.1029/2021JE006898).

This article is protected by copyright. All rights reserved.

fluviolacustrine environment, which would be conducive to preservation of biosignatures from paleolake-inhabiting lifeforms. Here we show that carbonate-bearing rocks within and outside of Jezero crater have the same range of visible-to-near-infrared carbonate absorption strengths, carbonate absorption band positions, thermal inertias, and morphologies. Thicknesses of exposed carbonate-bearing rock cross-sections in Jezero crater are ~75-90 meters thicker than typical ROB unit cross-sections in the Nili Fossae region, but have similar thicknesses as ROB unit exposures in Libya Montes. These similarities in carbonate properties inside and outside of Jezero crater is consistent with a shared origin for all of the carbonates in the Nili Fossae region. Carbonate absorption minima positions indicate that both Mg- and more Fe-rich carbonates are present in the Nili Fossae region, consistent with the expected products of olivine carbonation. These estimated carbonate chemistries are similar to those in martian meteorites and the Comanche carbonates investigated by the Spirit rover in Columbia Hills. Our results indicate that hydrothermal alteration is the most likely formation mechanism for non-deltaic carbonates within and outside of Jezero crater.

Plain Language Summary

Spacecraft orbiting Mars can measure the composition of rocks that make up its surface. Understanding rock composition allows us to interpret past environmental conditions on Mars, including their likelihood to be habitable. Using data acquired from orbit, researchers have found carbonate minerals in Jezero crater and the surrounding region—called the Nili Fossae region. Jezero crater is the landing site of NASA’s Mars 2020 Perseverance rover and once contained a lake. The discovery of carbonates is exciting because on Earth they sometimes form

in habitable environments and preserve fossils. In this study, we used all available high resolution orbital datasets to look at similarities and differences between carbonate-bearing rocks within and outside of Jezero crater. We found that carbonate-bearing rocks within and outside of Jezero crater have similar orbital properties, implying that they formed by the same processes. We found that the range in chemistries (magnesium-rich versus iron-rich) for carbonates within and outside of Jezero crater is similar to carbonate chemistries found in martian meteorites and by other rovers on Mars. The carbonates within and outside of Jezero crater could have formed by the same water-rock interactions that formed carbonates discovered in martian meteorites and by other rovers on Mars.

1.0 Introduction

The Nili Fossae region lies immediately west of the ~3.96 Gyr old (Werner, 2008) Isidis impact structure on Mars and north of the Late Hesperian age (Greely and Guest, 1987) Syrtis Major volcano. Widespread occurrences of olivine were first reported in Nili Fossae using data from the Thermal Emission Spectrometer (TES; Christensen et al., 2001) aboard the Mars Global Surveyor spacecraft (Hoefen et al., 2003). Nili Fossae is one of the most mineralogically diverse exposures of the martian surface, with evidence for olivine, pyroxene (Mustard et al., 2009), phyllosilicates (Ehlmann et al., 2009; Mustard et al., 2008), carbonates (Ehlmann et al., 2008b), and sulfates (Ehlmann and Mustard, 2012; Quinn and Ehlmann, 2019) observed in orbital spectroscopic data. Here we focus primarily on the olivine-bearing unit present in Jezero crater and the surrounding Nili Fossae and Libya Montes regions (Kremer et al., 2019), which we term the regional olivine-bearing unit (ROB unit).

Previously proposed origins for the $\sim 3.82 \pm 0.07$ Gyr age (Mandon et al., 2020) ROB unit include an ultramafic ashfall deposit (Kremer et al., 2019; Mandon et al., 2020), an impact spherule deposit (Palumbo and Head, 2018) from an impact younger than Isidis (Mandon et al., 2020), or detrital sedimentary rock (Rogers et al., 2018). Spectral data interpreted by modeling suggest ~ 20 - 25% modal abundance of olivine in this unit (Edwards and Ehlmann, 2015) and average olivine grain sizes of 0.5 mm or larger (Brown et al., 2020). It has been variably altered to carbonate, phyllosilicate(s), and hydrated silica or Al-phyllosilicate (Bishop et al., 2013b; Bramble et al., 2017; Brown et al., 2010; Ehlmann et al., 2008b; Goudge et al., 2015; Mandon et al., 2020; Tarnas et al., 2019; Viviano et al., 2013) and has a fractured-to-rubby texture (Bramble et al., 2017; Kremer et al., 2019). Its compositional and thermal inertia properties are similar to the Algonquin olivine-rich tephra deposit and Comanche carbonate investigated by NASA's Spirit rover (Ruff et al., 2019), as well as other high thermal inertia clastic rocks on Mars (Rogers et al., 2018). The ROB unit drapes into the Jezero crater rim and is present on the modern-day crater floor (Goudge et al., 2015; Kremer et al., 2019; Mandon et al., 2020; Sun and Stack, 2020). It is also incised by rivers that flowed into Jezero crater (Goudge et al., 2015) and deposited the deltaic outcrops there (Fassett and Head, 2005; Goudge et al., 2017; Schon et al., 2012). The Jezero delta deposits contain low calcium pyroxene, olivine, phyllosilicate(s), carbonate, and possible hydrated silica (Ehlmann et al., 2009; Goudge et al., 2015, 2018; Horgan et al., 2020a), much of which is likely detrital (Goudge et al., 2015), but some of which may be authigenic (Bristow and Milliken, 2011).

Recent photogeologic mapping has defined 15 bedrock units in western Jezero crater (Stack et al., 2020). Five of these units are carbonate-bearing: the delta blocky unit, delta

truncated curvilinear layered unit, delta layered rough unit, crater floor fractured 2 unit, and margin fractured unit (Figure 1). Goudge et al., (2015) and Ehlmann et al., (2008) grouped the carbonate-bearing units exposed along the inner margin (margin fractured) and on the crater floor (crater floor fractured 2) of Jezero, and correlated these deposits within the crater with the surrounding ROB unit, due to their morphological and spectral similarities. Later work presented evidence consistent with a fluviolacustrine origin for carbonates in the margin fractured unit, highlighting in particular the association of deeper 2.5 μm absorptions and low 2.3/2.5 μm band depth ratios with the approximate maximum height of the Jezero paleolake (Horgan et al., 2020a). These authors also highlighted possible spectral trends with respect to distance from the inlet valley. An unknown amount of fluviolacustrine sediment was deposited along the crater rim during highstanding periods of the Jezero paleolake, and it is possible that these sediments were carbonate-bearing and have since been lithified, as is common along margins of alkaline lakes on Earth (Horgan et al., 2020a). The observation of strong VNIR spectral signals of carbonate near the former margin of the Jezero paleolake is therefore consistent with formation of these carbonates in a near-shore fluviolacustrine environment. Here we compare the evidence for the carbonate formation scenario presented by Goudge et al., (2015) and Ehlmann et al., (2008)—where carbonate formation in the margin fractured unit and ROB occurs via the same processes—versus the scenario proposed by Horgan et al., (2020a), where carbonates in the margin fractured unit form by different processes than carbonates in the ROB.

Determining the conditions of carbonate formation in Jezero crater is key to evaluating past habitability and potential for biosignature preservation in rocks explored by the

Perseverance rover. This must be undertaken using orbital data until the Perseverance rover encounters carbonate-bearing rocks, which it will be guided to via interpretations of orbital data. To evaluate the similarities and differences between carbonates within and outside of Jezero crater, and to estimate their chemistry, we integrated data from the Compact Reconnaissance Imaging Spectrometer for Mars (CRISM; Murchie et al., 2007), images and digital elevation models (DEMs; Beyer et al., 2018) from the High Resolution Imaging Science Experiment (HiRISE; McEwen et al., 2007) and Context Camera (CTX; Malin et al., 2007), as well as data from the Thermal Emission Imaging System (THEMIS; Christensen et al., 2004).

2.0 Background

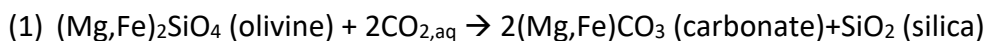
Phyllosilicates in the Nili Fossae region were first discovered using data from the Observatoire pour la Minéralogie, l'Eau, les Glaces et l'Activité (OMEGA; Bibring et al., 2004) instrument aboard Mars Express (Poulet et al., 2005), indicating that this landscape preserves evidence of past aqueous activity. Higher spatial resolution data from CRISM aboard the Mars Reconnaissance Orbiter (MRO) found evidence for phyllosilicates (Ehlmann et al., 2009; Mustard et al., 2008), carbonates (Ehlmann et al., 2008b), sulfates (Ehlmann and Mustard, 2012; Quinn and Ehlmann, 2019), and mafic minerals (Mustard et al., 2009) in Nili Fossae and showed that these minerals were correlated with specific units in a regionally extensive stratigraphy. From oldest to youngest, the Nili Fossae region includes a basement sequence, an olivine-bearing unit, a capping unit, and a sulfate-bearing unit (Ehlmann and Mustard, 2012). The basement sequence has been further subdivided into the Stratified Basement Unit, Blue Fractured Unit, Mixed Lithology Plains Unit, LCP-bearing Plateaus Unit, and Fe/Mg-smectite-

bearing Mounds Unit (Scheller and Ehlmann, 2020) and contains well-preserved martian crust older than 3.9 Gyr (Mustard et al., 2009), which has no comparably well-preserved analog in Earth's geologic record. The basement sequence contains widespread low calcium pyroxene and phyllosilicate VNIR spectral signatures (Scheller and Ehlmann, 2020), as well as outcrops containing kaolinite (Bramble et al., 2017; Ehlmann et al., 2009) and hydrated silica (Tarnas et al., 2019). The capping unit is associated with spectra consistent with mafic minerals (Bramble et al., 2017; Mustard et al., 2009) and glass (Cannon et al., 2017) and is interpreted to be volcanoclastic (Bramble et al., 2017; Hundal et al., 2020). The sulfate-bearing unit records evidence for standing bodies of water, diagenesis under acidic conditions, and fluvial activity (Quinn and Ehlmann, 2019). Spectral features attributed to the presence of specific minerals have previously been mapped in Jezero crater via calculation of band parameters (Ehlmann et al., 2008a, 2009; Goudge et al., 2015; Horgan et al., 2020a), linear VNIR spectral unmixing (Zastrow and Glotch, 2021), and Generative Adversarial Network based prototype spectrum mapping (Saranathan and Parente, 2021).

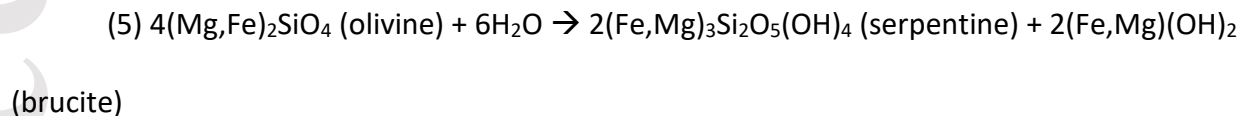
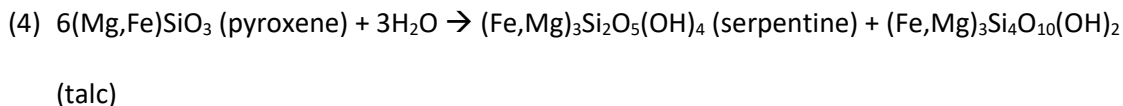
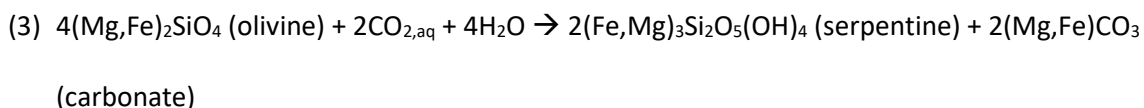
Proposed alteration hypotheses for the ROB unit, including the exposures on the Jezero crater floor and margin, are groundwater percolation under geothermal gradient-driven temperatures (Ehlmann et al., 2009), alteration under a thick CO₂ atmosphere (Edwards and Ehlmann, 2015; van Berk and Fu, 2011), simultaneous serpentinization and carbonation that occurred during dehydration of the underlying phyllosilicate basement (Brown et al., 2010; Viviano et al., 2013), carbonation of partially serpentinized olivine (Viviano et al., 2013), alteration under the conditions of the modern day martian atmosphere (Kelemen et al., 2020), low temperature water-rock alteration (Edwards and Ehlmann, 2015), low temperature

carbonate rind formation (Ehlmann et al., 2008b; Jull et al., 1988), or surface weathering to carbonate (Ehlmann et al., 2008b). Distinguishing between these hypotheses using orbital data alone is challenging, but mineral identifications and geologic context observed by the Mars 2020 Perseverance rover should be sufficient to constrain the causes of carbonation and other alteration, as mineral assemblages and their distributions can be used to constrain reaction conditions.

Carbonation of Fe, Mg, and Ca-bearing silicate material on Earth—including mafic and ultramafic rock—occurs via water-rock-gas reactions with high CO₂ activity/partial pressure in both high and low temperature and pressure conditions. Direct carbonation of olivine and pyroxene occurs via the reactions

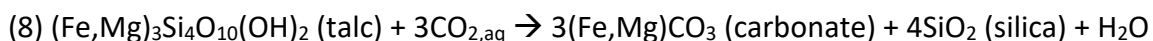
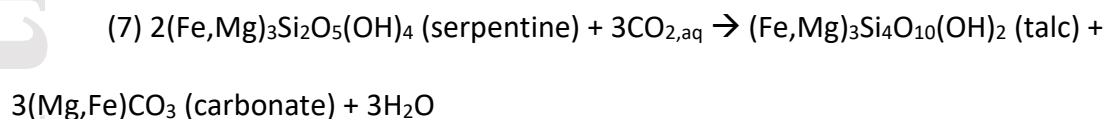
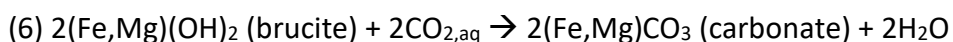


while carbonation can also follow or accompany alteration of pyroxene and olivine via the serpentinization reaction series



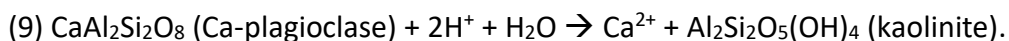
that produces serpentine, brucite, and talc, which can then be carbonated. Serpentinization is the oxidation of reduced silicates by water and includes partitioning of Fe³⁺ into magnetite at

temperatures > ~200 °C and Fe³⁺-bearing serpentine at temperatures < ~200 °C (Klein et al., 2014). Additional phases formed during serpentinization include fuchsite, Fe-hydroxides, and sulfides (de Obeso and Kelemen, 2018). The products of olivine and pyroxene serpentinization are carbonated by the reactions



which cause formation of carbonate and silica (Kelemen et al., 2011; Matter and Kelemen, 2009; Moody, 1976; Oelkers et al., 2008; Pens et al., 2016). If reactions 1-8 all proceed to completion, the resulting phases are carbonates and silica. Silica precipitated from water-rock interactions, such as carbonation, is typically amorphous hydrated silica (SiO₂·nH₂O) (Jones and Segnit, 1971). Silica crystallinity increases by more extensive interaction with water, forming opal-CT, opal-C, microcrystalline, and cryptocrystalline quartz (e.g., Kastner et al., 1977). In listvenite deposits, all primary minerals have been altered to form carbonate and hydrated silica, which is typically cryptocrystalline (e.g., Beinlich et al., 2020; Falk and Kelemen, 2015).

While ultramafic rocks contain primarily olivine and pyroxene, mafic rocks contain plagioclase, which can be altered to Al-phylosilicate via the reaction (Matter and Kelemen, 2009)



Al-phylosilicates are therefore common in carbonated mafic rocks, particularly when carbonation occurs at low pH and/or at high water:rock ratios (e.g., CarbFix drillcores in Iceland, Alfredsson et al., 2013; mafic dike in Colorado Plateau, Costello et al., 2020).

Carbonate can also abiotically precipitate independently of the presence of ultramafic materials, including in evaporite deposits (e.g., Kah et al., 2001), within carbonate-saturated water columns (e.g., Given and Wilkinson, 1985), and as pedogenic carbonate in soils (Zamanian et al., 2016). Evaporite deposits often contain other minerals in assemblage with carbonate, depending on the initial fluid composition, including various sulfates and chlorides (e.g., Kah et al., 2001). Biomediated precipitation of carbonate occurs in soils (e.g., Whiffin et al., 2007) and within water columns (e.g., Dupraz et al., 2004), or in structures such as microbial mats (e.g., Dupraz et al., 2009), shells, and reefs (e.g., Webb, 1996). Biomediated carbonate precipitation in the water column is not necessarily accompanied by precipitation of other minerals (e.g., Dupraz et al., 2009, 2004; Webb, 1996). Both abiotically and biotically precipitated carbonates preserve biosignatures on Earth. The habitability of conditions under which carbonates precipitate is therefore the most important control on carbonate biosignature preservation potential.

Martian carbonates have been identified in meteorites ALH 84001, Nakhla, Governor Valadares, Lafayette, and EETA 79001 at < 1 vol. % abundance (McSween, 1994; Niles et al., 2013), in the Comanche carbonate investigated by the Spirit rover at 16-34 wt. % abundance (Morris et al., 2010), in soil surrounding the Phoenix lander at 3-6 wt. % abundance (Boynton et al., 2009), possibly globally in Mars dust at 2-5 wt. % abundance (Bandfield et al., 2003) using TES—though sulfates could also explain this spectral signature (Lane et al., 2004), and in bedrock in multiple localities on the planet using CRISM (Amador et al., 2017; Bultel et al., 2019; Carrozzo et al., 2017; Carter et al., 2015; Ehlmann et al., 2008b; Jain and Chauhan, 2015; Michalski et al., 2017, 2013; Michalski and Niles, 2010; Wray et al., 2016) and TES (Glotch and

Rogers, 2013). Carbonate detections using CRISM are typically associated with mixed or proximal phyllosilicates (Bultel et al., 2019; Carrozzo et al., 2017; Michalski et al., 2017; Wray et al., 2016). Assuming equilibrium conditions, carbonates in ALH 84001 are estimated to have formed at 18 ± 4 °C (Halevy et al., 2011) 3.9-4.0 Gyr ago (Borg et al., 1999) and are present as concretions or as carbonate intergrown with feldspathic glass and orthopyroxene (Corrigan and Harvey, 2004; Steele et al., 2007), while Nahkla and Governor Valadares meteorites contain vein-filling carbonate (Gooding et al., 1991) and carbonate associated with silicate alteration zones (Bridges and Grady, 2000). Carbonates in martian meteorites are proposed to have formed either as hydrothermal alteration products (Steele et al., 2007; Treiman et al., 2002) or as evaporates (Bridges and Grady, 2000; Halevy et al., 2011; McSween and Harvey, 1998; Warren, 1998). Similarly, the Comanche carbonate has been proposed to form via hydrothermal alteration (Morris et al., 2010) or evaporite precipitation following alteration of the Algonquin volcanic tephra deposits (Ruff et al., 2014). In the evaporite precipitation hypothesis, the lack of sulfates and chlorides in assemblage with the Comanche carbonate is attributed to either spatial segregation during evaporation (Catling, 1999) or downward percolation of floodwaters through Algonquin-like rocks (Ruff et al., 2014), forming concretions without other salts, as is also suggested for carbonate formation in ALH 84001 (Warren, 1998).

3.0 Methodology

To characterize the properties of carbonate-bearing rocks within and outside of Jezero crater to the greatest extent possible from orbit, we integrated all orbital datasets that are at sufficiently high spatial resolution to investigate individual carbonate-bearing outcrops. We

used CRISM to identify VNIR spectra consistent with the presence of carbonate and minerals in assemblage with carbonate, images and DEMs from HiRISE and CTX to characterize morphology and place detections in their geologic and, if possible, stratigraphic contexts, as well as thermal inertia (TI) estimates from THEMIS measurements to evaluate dust cover and rock competency. We also used results from recent photogeologic mapping of Jezero crater by the Mars 2020 Rover Science Team (Stack et al., 2020) to determine which of these mapped units are carbonate-bearing. Finally, we compare the absorption minima positions for the 2.3 and 2.5 μm features in CRISM carbonate spectra to laboratory carbonate spectra, allowing for estimation of carbonate chemistry (Gaffey, 1987). This integrated approach permits a comprehensive comparison of carbonate within and outside of Jezero crater given all available high spatial resolution orbital datasets.

3.1 CRISM analysis

For the analysis within Jezero crater, we focused on CRISM images HRL000040FF (32 m/pixel), FRT000047A3 (18 m/pixel), and FRT00005C5E (18 m/pixel), which cover the Perseverance rover landing site, the geologic units mapped by Stack et al. (2020), and previously identified carbonates. We used CRISM data produced via three different processing techniques to identify spectral features consistent with the presence of carbonate and additional assemblage minerals. These included (1) the CRISM TRR3 pipeline, (2) the CRISM TER pipeline, and (3) the University of Massachusetts at Amherst (UMass) pipeline (Itoh and Parente, 2021). For analysis outside of Jezero crater, we used CRISM TRR3 data. RELAB IDs for the library spectra shown in Figures 3-12, 14, 18, S1-S10, and S12 are CACB08, CABE256,

CACB03, 397S013, C1SA51, C1RM34, and C1DH07, and these library spectra were compared to spectra extracted from within and outside of Jezero crater.

To identify regions with spectral signatures consistent with carbonate, we combined three separate mineral mapping approaches: (1) Band parameters (Viviano-Beck et al., 2014), (2) Dynamic aperture factor analysis/target transformation (DAFA/TT; Lin et al., 2021), (3) a Generative Adversarial Network based feature extraction technique (GAN; Saranathan and Parente, 2021). We compared the results from each of these techniques to test their validity. We also used DAFA/TT to locate unique spectra that are not present in the Minerals Identified through CRISM Analysis (MICA; Viviano-Beck et al., 2014) library that is employed during typical GAN mapping of CRISM data, then used those DAFA/TT-discovered spectra as prototypes for more detailed GAN mapping. After characterizing the spatial distribution of spectral signals in the three CRISM images analyzed, and interpreting the spectrally-dominant mineralogy consistent with those signals, we isolated CRISM pixels with similar spectral signals that outcropped over defined geologic units (e.g., dunes, differently textured bedrock, low thermal inertia material, high thermal inertia material, and specific geologic units) based on morphology, thermal inertia, and the mapping results from Stack et al. (2020).

Spectra were continuum-removed by fitting a hull to components of each spectrum that do not contain absorption features. The hulls were determined by fitting multiple line segments to local reflectance maxima of the spectra from 1-2.6 μm , with obvious artifacts removed from the spectrum, following the approach of Clark et al. (1987). We then interpreted the mineral assemblages consistent with spectra from these pixels via comparison to library spectra. Carbonate minerals are identified by the presence of absorptions centered at 2.3 and 2.5 μm ,

Fe/Mg-phyllsilicates by a narrow absorption centered at 2.3 μm , Al-phyllsilicate by a narrow absorption centered at 2.2 μm , hydrated silica by a broad absorption centered at 2.2 μm , and olivine by a broad absorption centered at 1.0 μm . This broad absorption centered at 1.0 μm could also be due to presence of Fe in carbonate if accompanying 2.3 and 2.5 μm features are present, as Fe^{2+} in FeCO_3 generates this 1.0 μm absorption. Integrating this information, we characterized the mineral composition of specific rock units or debris in Jezero crater to the greatest extent currently possible using orbitally-acquired VNIR hyperspectral data.

We compared carbonate spectral signals in Jezero crater with those in the ROB unit elsewhere in the Nili Fossae region using CRISM TRR3 images. For this analysis, we focused on CRISM images FRT00016A73 (18 m/pixel), FRT0000C968 (18 m/pixel), FRT0000C256 (18 m/pixel), FRT00009D96 (18 m/pixel), FRT000028BA (18 m/pixel), and FRT000095FE (18 m/pixel), which cover the ROB unit. We chose the last four images based on the strong carbonate absorption features in this area that were reported by Mandon et al., (2020). We used band parameters to highlight areas of the ROB in these CRISM images with strong carbonate absorptions, then extracted spectra from those areas for comparison to the carbonate spectra extracted from CRISM images covering the interior of Jezero crater. The shape, positions, and depths of absorptions are used for comparison of carbonate spectra. We compared the similarities of carbonate spectra within and outside of Jezero qualitatively via by-eye comparison, and quantitatively by measuring CRISM band parameters BD2290 and BD2500_2 (Viviano-Beck et al., 2014) for each spectrum, as well as the wavelength of the minima for the 2.3 and 2.5 μm absorptions. This latter measurement can also be used to estimate carbonate chemistry.

We estimated the chemistry of carbonates within and outside of Jezero crater by measuring the wavelength positions of the minima of the 2.3 and 2.5 μm absorptions, as MgCO_3 typically has absorptions centered at shorter wavelengths (2.295-2.310, 2.495-2.505) compared to FeCO_3 (2.320-2.325, 2.520-2.530) and CaCO_3 (2.340-2.350, 2.530-2.540) (Gaffey, 1987), all of which form solid solutions in natural carbonates. We fit a spline to each individual 2.3 and 2.5 μm absorption for each averaged CRISM spectrum to avoid minima position estimations being affected by high-frequency noise. We defined the shortest and longest wavelength for each of these absorptions based on the shortest and longest wavelengths used to measure the BD2290 and BD2500_2 CRISM band parameters, which measure these same absorptions (Viviano-Beck et al., 2014). Each spline fit was evaluated by-eye to ensure high-frequency noise was not overfit and the broader absorption trend was not underfit. These measured absorption minima wavelength positions were compared to those measured for every synthetic MgCO_3 (10 spectra), FeCO_3 (6 spectra), CaCO_3 (23 spectra), $(\text{Fe,Mg})\text{CO}_3$ (5 spectra), and $(\text{Ca,Mg})\text{CO}_3$ (14 spectra) spectrum in the Keck/NASA Reflectance Experiment Laboratory (RELAB) database, as well as spectra of MgCO_3 -nontronite-olivine mixtures (4 spectra) in this database. Spectra of synthetic samples were used to ensure sample purity and accuracy of sample chemistry characterization. We resampled all RELAB data to a spectral sampling of 5 nm, which compares to the 6.55 nm spectral sampling of CRISM (Murchie et al., 2007). We did not fit a spline to the absorption of RELAB spectra because they do not contain high frequency noise. We define the uncertainty in our absorption minima wavelength positions as \pm the spectral sampling, as the true absorption minimum could be between the individually sampled bands. Direct comparison of CRISM carbonate spectra absorption minima

wavelength positions to those of RELAB spectra from chemically-variable carbonates allows us to estimate the carbonate chemistries consistent with the measured CRISM spectra.

Following Horgan et al. (2020a), we mapped the value of the 2.3/2.5 μm absorption band depths in FRT0000C256 (18 m/pixel), FRT00009D96 (18 m/pixel), FRT000028BA (18 m/pixel), and FRT000095FE (18 m/pixel) to determine whether the carbonate absorption strength seen in the margin fractured unit is unique to Jezero, or is consistent with carbonate spectral signals in the ROB unit throughout the Nili Fossae region. We also used the Hyperspectral Subspace Identification (HySime) algorithm (Bioucas-Dias and Nascimento, 2008) to calculate endmembers imparting spectral variance in CRISM pixels covering outcrops of carbonate-bearing rocks in Jezero crater as well as in the CRISM images covering the ROB in the greater Nili Fossae region. We used information from band parameter mapping (Viviano-Beck et al., 2014) to isolate CRISM pixels used for spectral endmember extraction. If the endmembers resembled spectra characteristic of specific minerals, they were interpreted to reflect the composition of the surface covered by those CRISM pixels. This spectral endmember extraction and interpretation process is analogous to methods applied in past studies (e.g., Bandfield et al., 2002, 2000; Fischer et al., 2015; Glotch and Bandfield, 2006; Smith et al., 2000). It allowed us to extract clean mineral assemblage spectra from both Jezero crater and the surrounding Nili Fossae region CRISM images, even though the images from the surrounding region lacked spectrally bland pixels that would be required for spectral ratioing (e.g., Mustard et al., 2008). This allowed us to compare how relative 2.3 and 2.5 μm absorption strengths varied across CRISM images within and outside of Jezero crater.

3.2 HiRISE and CTX images and DEMs

We used the HiRISE and CTX image/DEM mosaics of Jezero crater generated by Ferguson et al., (2020), as well as HiRISE image/DEM mosaics and a global CTX mosaic generated by Dickson et al., (2020). HiRISE images were used to characterize unit morphology, distinguish between differently textured bedrock units, and differentiate between bedrock and aeolian bedforms or other clearly unconsolidated materials. This information was used to isolate specific CRISM pixels for spectral analysis and mineral assemblage interpretation (Section 3.1). We also used HiRISE DEMs to extract cross sections of CRISM detections and broader-scale geologic units for spectral and stratigraphic interpretations.

3.3 THEMIS thermal inertia mapping

To generate thermal inertia ($\text{J m}^{-2} \text{kg}^{-1} \text{s}^{-1/2}$) maps, we followed the methods and used the same input sources outlined in Edwards et al. (2018) for the KRC thermal model (Edwards et al., 2018; Ferguson et al., 2006; Kieffer, 2013), which was used to fit surface temperature estimates at each pixel to seasonally stable thermal inertia values. The inputs include observation time parameters (e.g., season, local time, solar azimuth, dust opacity, and modeled air temperatures), surface geometry (e.g., slope angle, aspect, and elevation) and estimates of material properties (e.g., albedo, emissivity, specific heat, and thermal conductivity; Kieffer, 2013; Putzig and Mellon, 2007). The thermal inertia map covering Jezero crater was produced by Edwards and Buz (2021) following these same methods. We used thermal inertia maps to help differentiate bedrock exposures from unconsolidated material. This information was used to isolate CRISM pixel clusters for spectral analysis and mineral assemblage

interpretation (Section 3.1). Thermal inertia maps were also used to compare the thermal inertia properties of carbonate-bearing rocks within and outside of Jezero crater.

4.0 Results

Combining the results of our mineral mapping with the photogeologic map of Jezero crater from Stack et al. (2020), we found VNIR spectra consistent with the presence of carbonate in (1) high TI bedrock in the margin fractured unit (Figure 3, S1-S5), (2) large aeolian bedforms proximal to the margin fractured unit (Figures 4, S6-S7), (3) the delta blocky unit (Figure 5), (4) the delta truncated curvilinear unit (Figure 6), (5) undifferentiated smooth material on the western delta (Figures 7, S8), (6) the delta layered rough unit (Figures 8, S9), (7) moderate TI bedrock in the crater floor fractured 2 (CFF 2) unit (Figures 9, S10-S11), and (8) low TI dunes and unconsolidated dark-toned material in the CFF 2 unit (Figure 10). We also report five newly discovered occurrences of hydrated silica in the same dark-toned material that Tarnas et al. (2019) and Dundar et al., (2019) reported hydrated silica in (Figures 11-12, S12).

Below we detail the VNIR spectral features of these carbonate- and hydrated-silica-bearing outcrops and associated mineral assemblage interpretations based on these spectral features. We also describe their morphology, thermal inertia properties, geologic context, and if possible their stratigraphic relationship to other units in Jezero crater. Diagnostic absorption features consistent with the presence of brucite and serpentine were not detected in any of the carbonate-bearing outcrops reported here, though this is not indicative of their absence, as demonstrated by groundtruthing of orbital observations in Gusev crater (Carter and Poulet, 2012; Morris et al., 2010), Meridiani Planum (Arvidson et al., 2015), and Gale crater (Fraeman

et al., 2016; Rampe et al., 2017). Hydrated silica is present in unconsolidated dark-toned material overlying the CFF 2 unit, and either hydrated silica or Al-phyllsilicate is present in CFF 2 unit bedrock (Section 4.1.1).

4.1 Crater floor fractured 2 unit

4.1.1 VNIR spectra

We find VNIR spectra consistent with the presence of carbonate in bedrock within the crater floor fractured 2 unit (Figures 9, S10-S11), as well as in dunes and dark-toned unconsolidated material directly overlying crater floor fractured 2 unit bedrock (Figure 10). The spectra are consistent with a mixture of carbonate, phyllosilicate(s), olivine, and possibly hydrated silica. The presence of carbonate is indicated by absorptions centered at 2.3 and 2.5 μm and has previously been mapped in this unit by Ehlmann et al., (2009) and Goudge et al., (2015). The higher 2.3/2.5 μm absorption band depth ratio of these spectra compared to spectra of pure carbonate, as well as the narrowing of the 2.3 μm feature relative to that of pure carbonate, indicates mixing with phyllosilicate (e.g., Figures 3e, S13). The broad absorption feature centered at 1.0 μm is consistent with the presence of olivine, but due to the presence of absorptions at 2.3 μm and 2.5 μm , is also consistent with FeCO_3 , or a mixture of FeCO_3 and olivine (e.g., Figures 3e, S13). Because the crater floor fractured 2 unit contains widespread spectra consistent with olivine, we interpret olivine—or olivine mixed with FeCO_3 —to be the more likely cause of the 1.0 μm centered broad absorption.

The presence of olivine, carbonate, and phyllosilicate(s) in the crater floor fractured 2 unit is consistent with past interpretations of the mineral assemblage in this unit in Jezero

crater (Horgan et al., 2020b) and the ROB unit in Nili Fossae (Brown et al., 2010). Based on the presence of a 2.2 μm feature (e.g., Figures 3e, S13 hydrated silica and montmorillonite spectra) that combines with the narrow 2.3 μm absorption (e.g., Figure 3e, S13 saponite, talc, and serpentine spectra), we interpret the presence of hydrated silica and/or Al-phyllsilicate, consistent with the interpretation of this same feature in a similar spectrum from the ROB unit in Tarnas et al. (2019). We reason that this feature is more likely to be caused by presence of hydrated silica rather than Al-phyllsilicate if the protolith material is ultramafic, as hydrated silica is ubiquitous in 100% carbonated olivine deposits (listvenites; e.g., Beinlich et al., 2020; Falk and Kelemen, 2015). However, if the protolith composition of this unit is mafic rather than ultramafic, Al-phyllsilicates may have formed via alteration of plagioclase during carbonation of olivine, as occurs during carbonation of mafic rocks on Earth (Matter and Kelemen, 2009).

We find five new outcrops of the smooth dark-toned hydrated-silica-bearing material reported by Tarnas et al. (2019) and Dundar et al. (2019) (Figures 11-12, S12). As reported by Tarnas et al. (2019), this smooth dark-toned material always outcrops immediately above the crater floor fractured unit. We also find an outcrop where smooth dark-toned material partially covers crater floor fractured unit bedrock, but does not cover it entirely, and over this area we find a stronger 2.2 μm absorption consistent with hydrated silica relative to the 2.5 μm absorption consistent with carbonate (Figure 12). This indicates that at least some of the 2.2 μm absorption signal from the crater floor fractured 2 unit is due to coverage of crater floor fractured 2 unit bedrock by hydrated-silica-bearing smooth dark-toned material. However, there is likely some material in crater floor fractured 2 bedrock bearing a 2.2 μm absorption feature consistent with hydrated silica and/or Al-phyllsilicate, as this absorption feature is

present even when there is no dark-toned material covering the outcrop (e.g., Figure 9). The origin and stratigraphic position of this smooth dark-toned hydrated-silica-bearing material remains ambiguous.

4.1.2 Morphology, thermal inertia, and geologic context

Crater floor fractured unit 2 bedrock outcrops containing carbonate-bearing mineral assemblages have fractures and linear ridges that are characteristic of this unit both within Jezero crater and regionally (Bramble et al., 2017; Goudge et al., 2017, 2015). This unit also contains larger-scale topographic features including broader ridges (Figure 9). Carbonate-bearing bedrock textures also include aeolian bedforms and dark-toned rubble overlying light-toned bedrock, which protrudes through this unconsolidated material (Figure 10). The morphology of crater floor fractured 2 unit bedrock with VNIR spectra consistent with carbonate at CRISM spatial scales is not appreciably different from outcrops of this unit with no clear VNIR carbonate spectral absorptions, nor is it appreciably different from the surface textures in much of the margin fractured unit. Parts of the crater floor fractured 2 unit with VNIR spectra consistent with the presence of carbonate are also not topographically higher than unit components that do not have clear VNIR spectral signatures of carbonate. Thermal inertia estimates of these outcrops are also consistent with both bedrock and overlying unconsolidated material containing VNIR spectra consistent with the presence of carbonate. The ROB unit is banded (Kremer et al., 2019) and some of this banding is visible in Jezero crater, but only unambiguously in the crater floor fractured 1 unit, with possible banding also in the margin fractured unit. None of these banded outcrops have VNIR spectra at CRISM spatial

scales consistent with the presence of carbonate. HiRISE images show no clear contacts between the crater floor fractured 1 and 2 units and the margin fractured unit.

4.2 Deltaic units

4.2.1 VNIR spectra

There are CRISM VNIR spectra consistent with the presence of carbonate in the delta blocky unit (Figure 5), the delta truncated curvilinear unit (Figure 6; Goudge et al., 2017), undifferentiated smooth material on the western delta (Figures 7, S8), and the delta layered rough unit (Figures 8, S9). The spectra are consistent with a mixture of carbonate, phyllosilicate, and either hydrated silica and/or Al-phyllosilicate (Figures 5d, 6c, 7d, 8d, S8d, S9e). The presence of carbonate is indicated by absorptions centered at 2.3 and 2.5 μm (Figures 5d, 6c, 7d, 8d, S8d, S9e). All VNIR spectra containing carbonate absorptions in the deltaic units have higher 2.3/2.5 μm ratios compared to carbonate-bearing VNIR spectra in the crater floor fractured 2 and margin fractured units (e.g., Figure 5d versus Figure 3e), indicating a higher spectral abundance of Fe/Mg-phyllosilicates mixed with carbonate in the deltas. The 2.2/2.3 μm absorption depth ratios are also lower in the deltaic outcrops of carbonate-bearing assemblages compared to those in the crater floor fractured 2 unit (e.g., Figure 5d versus Figure 9e), indicating a higher spectral abundance of Fe/Mg-phyllosilicate relative to the phase imparting the 2.2 μm absorption. It is unclear if the 2.2 μm absorptions in VNIR spectra of carbonate-bearing assemblages are caused by hydrated silica and/or Al-phyllosilicate (Figures 5d, 6c, 7d, 8d, S8d, S9e, S13). As noted by previous studies (Goudge et al., 2015) carbonate

spectral absorptions are more spatially widespread in the northern fan deposit relative to the western delta deposit (Figures 8 and S9 compared to Figures 5-7 and S8).

4.2.2 Morphology, thermal inertia, and geologic context

The morphological properties and stratigraphic relationships between the individual units in the Jezero delta are detailed in Stack et al. (2020). The units are, from stratigraphically youngest to oldest, the delta blocky, thickly layered and truncated curvilinear layered, thinly layered, and layered rough units. In the western delta, clear bedrock exposures of carbonate-bearing material at spatial resolutions measurable using CRISM are present in the delta blocky (Figure 5) and delta truncated curvilinear (Figure 6) units. These carbonate-bearing outcrops have previously been reported by (Ehlmann et al., 2009, 2008b; Goudge et al., 2015). Other locations with VNIR spectra consistent with the presence of carbonate are undifferentiated smooth, dark-toned material (Figures 7, S8). Light-toned bedrock exposures of carbonate-bearing material also have moderate thermal inertia (Figures 5-6) while carbonate-bearing undifferentiated smooth material has low thermal inertia (Figures 7, S8), consistent with the interpretation that the undifferentiated smooth material is unconsolidated relative to the light-toned bedrock. In the northern fan deposit, carbonate-bearing rock is widespread, both in moderate thermal inertia (Figure 8) and low thermal inertia (Figure S9) material. All outcrops of deltaic carbonate-bearing rocks are not morphologically distinct from other rocks within their units, nor do they show notable stratigraphic relationships with other rocks in their units. It is unclear whether the undifferentiated smooth material is eroded unconsolidated material from

the deltaic bedrock units, or if it has experienced a different authigenic or detrital formation history compared to those deltaic bedrock units.

4.3 Margin fractured unit and proximal aeolian bedforms

4.3.1 VNIR spectra

Outcrops of bedrock in the margin fractured unit have VNIR absorption features consistent with a mixture of carbonate, phyllosilicate, and possible olivine, as has been reported by previous studies (Goudge et al., 2015; Horgan et al., 2020a). The presence of carbonate is indicated by absorptions centered at 2.3 and 2.5 μm . While spectra of the margin fractured unit have the lowest 2.3/2.5 μm absorption band depth ratios within Jezero crater, their relative strength is consistent with a mixture of carbonate and phyllosilicate (Figures 3, S1-S5). This is further supported by the narrow shape of the 2.3 μm feature relative to that typical of pure carbonate (Bishop et al., 2013a) (Figures 3, S1-S5). Variations in relative grain sizes, modal abundances, and mixing regimes can affect the relative depth and shape of 2.3 μm and 2.5 μm absorptions in mineral mixtures. The low 2.3/2.5 μm band depth ratio values in the margin fractured unit are also found in the ROB unit elsewhere in Nili Fossae (Figures 3, S14), including in the ROB unit immediately outside of Jezero crater (Figure 13a), indicating that the carbonate spectral strength in the margin fractured unit is nonunique in a regionally context. As indicated by Horgan et al., (2020a), the broad absorption feature centered at 1.0 μm is consistent with the presence of olivine, but due to the presence of absorptions at 2.3 μm and 2.5 μm is also consistent with FeCO_3 , or a mixture of FeCO_3 and olivine (Figures 3e, S1d, S2d, S3c, S4c, S5d, S13) The lack of clear contacts between the ROB unit draping into Jezero crater

and the margin fractured unit does favor the interpretation that the 1.0 μm absorption in the margin fractured unit is due to olivine, which is present throughout the ROB unit, or a mixture of olivine and FeCO_3 .

The large aeolian bedforms immediately proximal to the margin fractured unit contain similar VNIR spectra to margin fractured bedrock (Figures 4, S6-S7), indicating that they may be locally sourced sediments composed of the same carbonate-phyllsilicate-possible olivine mixture as the margin fractured unit. Many aeolian bedforms in Jezero crater have similar VNIR spectral properties as proximal bedrock, indicating that they are often locally sourced from erosion of that bedrock (Arvidson and Christian, 2020). A reported example of this phenomenon is the presence of olivine-bearing aeolian bedforms near olivine-bearing bedrock (Brown et al., 2020; Edwards and Ehlmann, 2015).

4.3.2 Morphology, thermal inertia, and geologic context

The margin fractured unit has a fractured, sometimes rubbly, and occasionally ridged appearance similar to the crater floor fractured 2 unit (Figures 3b-d, S1b-c, S2b-c, S3b, S5b-c). It has high thermal inertia compared to other units in Jezero crater (e.g., Figure S15). There are no visible contacts between the margin fractured unit and the crater floor fractured 2 unit, nor the margin fractured unit and the ROB unit that drapes into Jezero crater (Goudge et al., 2015), with cross sections showing a gradational relationship in all cases (Figure S16). The VNIR spectral signatures (Figures 14-15), morphology (Figure 16), and thermal inertia (Figures 17, S15) of the margin fractured unit resemble the ROB unit (Goudge et al., 2015), including the ROB component immediately north of the crater rim from the margin fractured unit, and the

component of the ROB that drapes into Jezero crater (Figure S16). Many of the strongest carbonate absorption features in this unit are associated with elevation of the estimated maximum Jezero lake level (Horgan et al., 2020a). The delta blocky unit outcrops stratigraphically above the margin fractured unit and there are clear contacts in many locations (e.g., Figure 3c). In one area, a cross-section exposure of the margin fractured unit shows possible banding similar to that seen in the crater floor fractured 1 unit (Figures 18, S3), though these may actually be diagenetically-generated ridges rather than beds. The largest margin fractured unit outcrops contain either plateaus (e.g., Figures 3, S1, S4) or mounds of bedrock bearing the characteristic fractured morphology of the unit (e.g., Figure S2, S3, S5).

The large aeolian bedforms proximal to the margin fractured unit have low thermal inertia—which is expected for unconsolidated material—and overlie margin fractured bedrock in many locations (e.g., Figures 4, S7). These aeolian bedforms are longer wavelength than those in lower elevations of western Jezero crater, likely due to a combination of physical properties of the unconsolidated grains and the predominant wind patterns in Jezero crater (Day and Dorn, 2019).

4.4 ROB unit outside of Jezero crater

4.4.1 VNIR spectra

Comparison of carbonate spectra from the margin fractured and CFF 2 units to carbonate spectra from the ROB elsewhere in the Nili Fossae region demonstrates that the variability in carbonate absorption strength in Jezero crater is also found outside of Jezero crater (Figures 14-15), as are variations in carbonate absorption minima wavelength positions

(Figure 15). Both qualitative (Figure 14f) and quantitative (Figure 15) analyses demonstrate that the spectral properties of carbonates inside of Jezero crater are matched by spectral properties of carbonates outside of Jezero crater in the greater Nili Fossae region. Band parameter measurements show that carbonate spectra inside of Jezero crater have the same 2.3 and 2.5 μm band depth trend as carbonate spectra from the ROB unit, and fall within the range of band depth values measured in the ROB unit (Figure 15a). The 2.3 and 2.5 μm absorption minima wavelength positions within and outside of Jezero crater also show the same distribution (Figure 15b).

The 2.3/2.5 μm band depth ratios in carbonate-bearing rocks outside of Jezero crater are equivalent to those found in the margin fractured unit (Figures 13, 15a, S14). This is true in outcrops of the ROB 100-200 km northeast of Jezero crater (Figures 13b, 15a, S14) and outcrops of the ROB immediately northwards of the Jezero crater rim from the margin fractured unit (Figure 13a). These low 2.3/2.5 μm band depth ratios span extensive amounts of outcrop regionally (Figure 13, S14), and indeed may be present in many outcrops without CRISM FRT, HRL, FRS, HRS, or ATO image coverage. The spectral endmembers associated with CRISM pixels with BD2500_2 values greater than 0.005 inside and outside of Jezero crater are similar and contain absorptions consistent with the presence of carbonate, Fe/Mg-phylllosilicate, and olivine (Figure 13e). Overall, these results show no appreciable differences between carbonate VNIR spectra within and outside of Jezero crater.

4.4.2 Morphology, thermal inertia, and geologic context compared to inside Jezero crater

The ROB unit has a fractured, rubbly, and often ridged morphology outside of Jezero crater, which resembles margin fractured and CFF 2 unit rocks inside of Jezero crater (Figure 16). As described in Section 4.3.2, the ROB unit drapes into Jezero crater and transitions into the margin fractured unit with no clear contacts, implying that they are likely the same unit, as past photogeologic mapping has also indicated (Goudge et al., 2015; Sun and Stack, 2020). The thermal inertia values of carbonate-bearing rocks in the ROB unit outside of Jezero crater cover a range that encompasses the thermal inertia values of carbonate-bearing rocks inside of Jezero crater (Figure 17). The most common thermal inertia values for carbonates within and outside of Jezero crater are also the same (~ 330 versus $\sim 290 \text{ J m}^{-2} \text{ kg}^{-1} \text{ s}^{-1/2}$), respectively; Figure 17). The interior of Jezero crater has more low thermal inertia carbonate-bearing rocks relative to the ROB unit outside of Jezero crater, likely corresponding to the aeolian bedforms (e.g., Figures 4, S6, S7) and unconsolidated material (Figure 10) containing carbonates there. Comparison of morphologies (Figure 16) and thermal inertia values (Figure 17) of carbonate-bearing rocks within and outside of Jezero crater show striking similarities between these rocks. An ashfall origin has been proposed for the ROB unit (Kremer et al., 2019; Mandon et al., 2020), and its high thermal inertia both within and outside of Jezero crater is similar to other olivine-bearing clastic rocks on Mars (Rogers et al., 2018), consistent with this hypothesis.

4.5 Thickness of carbonate-bearing rocks inside and outside of Jezero crater

The margin fractured unit is at least ~ 100 meters thick in some locations in Jezero crater, as demonstrated by exposed cross sections of carbonate-bearing outcrop (Figure 18). Since the shape of Jezero crater prior to emplacement of the ROB is unknown, variations in

topography spanned by the ROB (e.g., Figure S16) cannot be used as definitive evidence for unit thickness. It is possible that the margin fractured unit is thicker than ~100 meters in Jezero crater, but there are no exposed cross sections of carbonate-bearing outcrop to definitively demonstrate this. Measured thicknesses of the ROB range from ~1-25 meters in Nili Fossae and from ~1-110 meters in Libya Montes (Kremer et al., 2019). As such, while the margin fractured unit is thicker than the ROB typically is in Nili Fossae, its thickness more closely resembles the upper observed limit of ROB thicknesses in cross sections of the unit in Libya Montes, where carbonates have also been detected (Bishop et al., 2013b).

4.6 Carbonate chemistry

Carbonates in the Nili Fossae region—including in Jezero crater—have 2.3 μm and 2.5 μm absorption minima wavelength positions consistent with Mg-rich carbonate (Ehlmann et al., 2008b). The presence of Fe-rich carbonates in Jezero crater has also recently been proposed based on linear unmixing (Zastrow and Glotch, 2021). In nature, Fe/Mg-carbonates are a solid solution between FeCO_3 and MgCO_3 . The results presented here are consistent with the presence of Fe/Mg-carbonates within and outside of Jezero crater based on variability in the 2.3 μm and 2.5 μm absorption minima wavelength positions in extracted spectra (Figure 15b). The absorption minima positions of carbonate spectra inside and outside of Jezero crater show a clear trend between more Mg- and Fe-rich phases (Figure 15b), particularly via the variability of the 2.5 μm absorption minimum wavelength position. Mixing of carbonates with Fe/Mg-phyllsilicates will likely affect their 2.3 μm absorption minimum positions. Within and outside of Jezero crater, the presence of Fe/Mg-phyllsilicates in carbonate-bearing assemblages may

limit variability in the 2.3 μm absorption minimum position, which could affect estimates of carbonate chemistry. However, there is no indication of mixing between carbonates and phases with 2.5 μm absorptions, meaning the 2.5 μm absorption minimum position is likely a strong indicator of carbonate chemistry (Figure 15b). The range in estimated carbonate chemistry is similar to that of the Comanche carbonate, which was characterized as Fe/Mg-carbonate (Morris et al., 2010), and is a composition expected from carbonation of olivine, which typically contains both Mg and Fe. Estimates for the Mg and Fe content of olivine in the Nili Fossae ROB unit range from ~25-75% Fe-olivine and ~25-75% Mg-olivine (Clenet et al., 2013; Koeppen and Hamilton, 2008), with the most recent estimates ranging from 60% Fe and 40% Mg to 35% Fe and 65% Mg (Brown et al., 2020). Therefore, carbonation of the ROB should produce both Mg- and Fe-bearing carbonate phases, which explains the absorption minima positions consistent with both Mg- and Fe-bearing carbonate in the spectra extracted here.

5.0 Discussion

Stark similarities in the VNIR spectral properties (Section 5.1), morphologies (Section 5.2), thermal inertias (Section 5.3), and thicknesses (Section 5.4) of non-deltaic carbonates within Jezero crater and in the ROB outside of Jezero crater indicate that non-deltaic carbonate-bearing rocks in Jezero crater are likely components of the ROB unit. Qualitatively, the VNIR spectra (Figure 14) and morphologies (Figure 16) of non-deltaic carbonate-bearing rocks within and outside of Jezero crater are alike. Quantitatively, the values and variability of carbonate absorption band depths in VNIR spectra (Figure 15a), carbonate absorption minimum wavelength positions in VNIR spectra (Figure 15b), and estimated thermal inertias (Figure 17)

are similar for these rocks within and outside of Jezero crater. The margin fractured unit appears to be at least ~100 meters thick in some locations in Jezero crater, which is thicker than the ~1-25 meters typical of the ROB in Nili Fossae, but similar to the ~1-100 meters typical of the ROB in Libya Montes (Kremer et al., 2019), where this unit is also carbonated (Bishop et al., 2013b). Overall, our results demonstrate that no appreciable differences exist between carbonates within Jezero crater and the ROB unit given all available high resolution orbital datasets. This similarity implies that both units were emplaced and altered by the same processes, and that no additional fluviolacustrine process need be invoked to explain the properties of the margin fractured unit. Estimated carbonate chemistries within and outside of Jezero crater span a solid solution ranging from MgCO_3 to $(\text{Fe,Mg})\text{CO}_3$ (Figure 15b) which is expected from carbonation of olivine that is a solid solution between forsterite and fayalite. This estimated carbonate chemistry is similar to that of the Comanche carbonate in Columbia Hills (Morris et al., 2010) and carbonates in martian meteorites (Steele et al., 2007), implying that these carbonates may form through similar water-rock alteration processes.

5.1 Similarity of non-deltaic carbonates within and outside of Jezero crater

Non-deltaic carbonate-bearing rocks within Jezero crater resemble the ROB unit in every metric that is observable from orbit, including VNIR spectral properties, morphology, thermal inertia, and thickness given observations of the ROB unit in Libya Montes. The ROB unit also drapes into Jezero crater, directly connecting to the margin fractured unit with no visible contacts (Sun and Stack, 2020). It is therefore unlikely that these practically identical rock units were deposited and altered by different mechanisms. Rather, the simplest explanation is that

non-deltaic carbonate-bearing rocks in Jezero crater are components of the ROB unit, and that both were carbonated by the same process. This finding is consistent with hypotheses presented by Goudge et al., (2015). While the results presented here are consistent with this simplest explanation, they cannot definitively rule out formation of carbonates in the margin fractured unit in a fluviolacustrine environment. Observations by the Mars 2020 Perseverance rover mission in Jezero crater can determine the mechanisms through which these carbonates formed both within and outside of Jezero crater.

5.2 Thickness of marginal fractured unit

Some margin fractured unit outcrops show possible banding (e.g., Figure S3b, S5b) and are ~100 meters thick (e.g., Figure 18), similar to ROB outcrops in Libya Montes (Kremer et al., 2019). If the ROB was originally deposited in the Nili Fossae region as a similarly thick deposit to that found in Libya Montes, it may have been eroded to <10% of its original thickness in most of the Nili Fossae region. This interpretation is consistent with the typical material properties of high TI clastic rocks on Mars, which are interpreted to be friable, eroding faster than surrounding rocks to expose relatively dust-free surfaces (Rogers et al., 2018). Olivine sands are commonly seen surrounding the ROB unit inside and outside of Jezero crater (Brown et al., 2020; Edwards and Ehlmann, 2015; Ehlmann et al., 2009), and carbonate aeolian bedforms are observed next to outcrops of margin fractured bedrock (Figures 4, S6, S7), showing these units have eroded to some extent. Observed thickness variations in the ROB unit are consistent with deposition as an airfall deposit, with measured thicknesses decreasing with increased distance from Syrtis Major (Kremer et al., 2019). If erosion rates of the ROB unit were consistent

everywhere in the unit except for in Jezero crater, where it is shielded by a crater rim, then it would maintain this observed thickness trend.

If the ROB unit has experienced little erosion since its original emplacement, then the observation of a carbonate-bearing rock unit in Jezero crater that is ten times thicker than nearby ROB deposits implies a difference in deposition mechanism or environment. Possible differences include that deposition into an impact crater caused the ROB to build into a thicker deposit relative to surrounding terrain, or that at least ~90 meters of lacustrine sediments were deposited to form the margin fractured unit. Deposition of hundreds of meters of lacustrine sediment has been observed at Mount Sharp (Rapin et al., 2021). However, a simpler explanation is that the ROB unit has experienced differential erosion within and outside of Jezero crater, with erosion being lessened in the margin fractured unit via buttressing against mass wasting and protection from aeolian weathering by the Jezero crater rim.

5.3 Implications for hydrated silica or Al-phyllsilicate detections

The 2.2 μm feature detected in spectra extracted from the CFF 2 and ROB units can be attributed to either hydrated silica or Al-phyllsilicate, both of which contain an absorption feature centered at 2.2 μm (e.g., Figure 3e). Hydrated silica has also been reported in smooth dark-toned material in Jezero crater that overlies the CFF 2 unit (Tarnas et al., 2019), and here we report five new occurrences of hydrated silica in this same material. Variability in the 2.2 μm feature band depth has previously been mapped by Horgan et al. (2020). In some carbonate-bearing CFF 2 outcrops, the 2.2 μm absorption can be attributed to partial CFF 2 bedrock coverage by this unconsolidated dark-toned material (e.g., Figure 12), while other CFF 2

outcrops that lack such coverage (e.g., Figure 9) also contain a 2.2 μm absorption, implying that this absorption is also associated with CFF 2 bedrock. Large exposures of the smooth dark-toned material exhibit clear enough absorptions to diagnostically determine the presence of hydrated silica (e.g. Figure 11, S12), but the 2.2 μm absorption in CFF 2 bedrock is always part of a spectral mixture dominated largely by carbonate, Fe/Mg-phyllsilicate, and possible olivine (e.g. Figure 9). The 2.2 μm feature in this CFF 2 bedrock can therefore be attributed to either hydrated silica or Al-phyllsilicate.

On Earth, carbonation of ultramafic rocks is accompanied by formation of hydrated silica (Beinlich et al., 2020; Falk and Kelemen, 2015), while carbonation of mafic rocks is accompanied by formation of Al-phyllsilicate (Alfredsson et al., 2013; Costello et al., 2020; Matter and Kelemen, 2009). The CFF 2 protolith composition is likely what dictates the formation of hydrated silica versus Al-phyllsilicate in these bedrock outcrops. The widespread presence of olivine in the ROB and CFF 2 units is consistent with an ultramafic composition, and if this interpretation is correct, then the 2.2 μm feature is likely caused by hydrated silica that coprecipitated with carbonate during water-rock alteration of olivine under high $p\text{CO}_2$. If the ROB and CFF 2 units are instead mafic in composition, then the 2.2 μm feature is likely caused by Al-phyllsilicate formation via alteration of plagioclase (Alfredsson et al., 2013; Matter and Kelemen, 2009).

5.3 Viable carbonate formation hypotheses

It is likely that the carbonates within and outside of Jezero crater all formed via the same processes, as they exhibit the same VNIR spectral properties (Figures 14-15), thermal

inertias (Figure 17), morphologies (Figure 16), and thickness ranges (Figure 18) as the ROB unit.

Given all available orbital observations, hydrothermal alteration (Alfredsson et al., 2013; Falk and Kelemen, 2015) carbonate rind formation (e.g., Jull et al., 1988), and evaporation (e.g., Ruff et al., 2014) remain viable mechanisms for carbonate formation in the Nili Fossae region, including in Jezero crater. While it remains possible that a subset of these carbonates formed in a lacustrine environment in Jezero crater, the simplest explanation is that all carbonates in the Nili Fossae region formed via the same mechanism, and this mechanism did not involve the lacustrine activity in Jezero crater. This conclusion is supported by the non-uniqueness of the margin fractured unit relative to the ROB in terms of VNIR spectra, morphology, thermal inertia, and thickness.

The composition, thermal inertia properties, and age of the ROB unit is similar to the Comanche carbonate and Algonquin tephra observed by the Spirit rover (Ruff et al., 2019). An ashfall origin has been proposed for the ROB (Kremer et al., 2019; Mandon et al., 2020), which is also the favored hypothesis for deposition of the Algonquin and Comanche rock units (McCoy et al., 2008; McSween et al., 2008; Morris et al., 2010; Ruff et al., 2014). Both the ROB unit and Columbia Hills rocks were likely deposited during the Noachian (Greeley et al., 2005; Mandon et al., 2020; McCoy et al., 2008) and have high thermal inertias similar to other olivine-bearing rocks on Mars that are likely clastic (Rogers et al., 2018). These similarities imply that carbonates in the ROB unit may have formed via the same carbonation process as the Comanche carbonate. Formation hypotheses for carbonates in Comanche and in martian meteorites include hydrothermal alteration (Morris et al., 2010; Steele et al., 2007; Treiman et al., 2002) and evaporation under low temperatures and low water/rock ratios (Bridges and

Grady, 2000; Halevy et al., 2011; McSween and Harvey, 1998; Ruff et al., 2014; Warren, 1998).

The Comanche carbonates were originally proposed to have formed via hydrothermal alteration (Morris et al., 2010), given similarities with basalt-hosted magnesite in Earth analog environments (Morris et al., 2011), and evidence for volcanic activity and hydrothermal alteration elsewhere in Columbia Hills (McCoy et al., 2008; McSween et al., 2008; Squyres et al., 2008). However, these carbonates were later proposed to have formed via minor leaching of Algonquin-composition rocks in CO₂-rich fluids and carbonate precipitation during evaporation of these fluids (Ruff et al., 2014). Carbonates in both orthopyroxenite (ALH 84001) and nakhlite martian meteorite lithologies are also proposed to have formed via hydrothermal alteration (Steele et al., 2007; Treiman et al., 2002) or as evaporites precipitated from small amounts of infiltrating water (Bridges and Grady, 2000; Halevy et al., 2011; McSween and Harvey, 1998; Warren, 1998), indicating that such processes are viable formation mechanisms for both the Comanche and ROB unit carbonates. Given the similarities in mineralogy, thermal inertia, and age between the Algonquin/Comanche deposits and the ROB unit within and outside of Jezero crater (Ruff et al., 2019), proposed formation mechanisms for the Comanche carbonate (Morris et al., 2010; Ruff et al., 2014), and evidence for similar processes in martian meteorites (Bridges and Grady, 2000; Halevy et al., 2011; McSween and Harvey, 1998; Niles et al., 2013; Steele et al., 2007; Treiman et al., 2002; Warren, 1998), either hydrothermal alteration or evaporating surface fluids could also explain carbonate formation in Nili Fossae.

Hydrothermal alteration is the simplest explanation for carbonate formation in the ROB unit, particularly if this unit is an ashfall deposit (Kremer et al., 2019), which would have been deposited as hot material atop a basement unit of hydrated minerals from which water would

be liberated to alter this unit (Brown et al., 2010). Alternatively, olivine-bearing rocks could be altered by later water-rock interactions under a variety of temperatures, similar to those that form listvenite deposits (Beinlich et al., 2020; Falk and Kelemen, 2015) and carbonated mafic rocks (Alfredsson et al., 2013; Costello et al., 2020; Morris et al., 2011; Treiman et al., 2002) on Earth. Hydrothermal alteration is also consistent with the (Fe,Mg)-carbonate solid solution composition ranges (Ehlmann et al., 2008b; Horgan et al., 2020a; Zastrow and Glotch, 2021; Figure 15b) estimated for carbonates in the ROB unit, which would be expected from carbonation of ROB unit olivine with an estimated composition of ~25-75% Fe-olivine and ~25-75% Mg-olivine (Brown et al., 2020; Clenet et al., 2013; Koeppen and Hamilton, 2008).

Infiltration of small quantities of water from surface ice melting or snowfall/rainfall could also result in evaporite carbonate formation in the ROB unit. Surface ice melting is the most viable of these mechanisms, since Mars experienced obliquity variations of $\sim 30^\circ$ and eccentricity variations of ~ 0.1 in the last 20 Myr alone, and experienced even more extreme obliquity/eccentricity variations during the last ~ 4 Gyr (Laskar et al., 2004). Obliquity variations cause redistribution of ice on the surface, while eccentricity variations could cause seasonal melting during the Noachian (Palumbo et al., 2018). Water from these melting events could have infiltrated the surface and evaporated to form carbonate. This same process forms carbonate in basaltic terrains on Earth (Knauth et al., 2003) and is a viable carbonate formation hypothesis for martian meteorites that does not require large volumes of water (Bridges and Grady, 2000; Halevy et al., 2011; McSween and Harvey, 1998; Warren, 1998). Small amounts of carbonate could also form via low temperature rind formation (Ehlmann et al., 2008b)—similar to processes that form carbonate rinds in meteorites in Antarctica (Jull et al., 1988)—or under

the conditions of the modern-day martian atmosphere (Kelemen et al., 2020). Given that such low water:rock ratio evaporative/alteration processes form < 1 vol. % carbonate in martian meteorites (McSween, 1994; Niles et al., 2013) and meteorites with carbonate rinds (El-Shenawy et al., 2020; Jull et al., 1988), they may not generate sufficient quantities of carbonate to be detected in CRISM VNIR data. Surface water infiltration and evaporation generates carbonate layers in basaltic rocks on Earth (e.g., Knauth et al., 2003), but this process would likely not generate the 20-25% carbonate modal abundance estimated for the entire ROB unit using CRISM (Edwards and Ehlmann, 2015). This indicates that hydrothermal alteration is a more viable carbonate formation hypothesis than evaporation of infiltrating surface fluids.

ROB unit carbonates could form as evaporites in the presence of region-scale surface water, which would require the presence of large water bodies covering the surface. Nili Fossae and Libya Montes are covered in some proposed martian ocean shorelines, but estimates for the distribution of these shorelines varies widely, and evidence for the presence of these oceans is inconclusive (Sholes et al., 2021). An ocean in the northern hemisphere of Mars would not need to exist for long periods of time for evaporite carbonate formation to occur, and in fact low temperature playa environments from rapidly receding floodwaters are more conducive to Mg-carbonate precipitation relative to the presence of long-lived ocean margins (McSween and Harvey, 1998; Niles et al., 2013; Warren, 1998). This is consistent with carbonate formation at the evaporating margins of martian oceans formed through episodic flooding events (Fairén et al., 2003). Deposition of a Late Noachian-Early Hesperian-aged layered sulfate sequence up to ~600 meter thick in the Nili Fossae stratigraphy indicates that there was widespread surface water coverage in this region (Quinn and Ehlmann, 2019). Quinn and

Ehlmann, (2019) proposed that the presence of this sulfate unit could indicate that the Nili Fossae region was at the margin of a martian ocean shoreline, or that ice-dammed regional lakes may have been stable for sufficiently long periods for sediment deposition. Ice-damming has controlled fluvial activity in the Nili Fossae region in multiple episodes (Matherne et al., 2020), increasing the viability of ice-dammed regional lakes in this area. However, the modern-day topography of the Nili Fossae region indicates that carbonate evaporites should not have formed exclusively in the ROB unit, as the underlying basement unit often forms topographic lows (Scheller and Ehlmann, 2020) where evaporating fluids would be concentrated. If the ROB unit covered the entire Nili Fossae region while it was submerged under regional scale surface waters, it would explain the lack of carbonate detections in the basement unit. While this is theoretically possible, the distribution of carbonate and precise requirements for the relative timing of ROB unit emplacement, erosion, and regional scale surface water coverage make this carbonate formation mechanism unlikely compared to hydrothermal alteration of the ROB unit.

Overall, hydrothermal alteration is the most viable hypotheses for carbonate formation in the ROB unit, particularly given that estimated carbonate chemistries in Nili Fossae (Ehlmann et al., 2008b; Horgan et al., 2020a; Zastrow and Glotch, 2021; Figure 15b) are exactly those expected from carbonation of estimated ROB unit olivine chemistries (Brown et al., 2020; Clenet et al., 2013; Koeppen and Hamilton, 2008), and that the ROB unit was deposited on a basement that contains hydrated minerals (Brown et al., 2010). Low levels of surface water infiltration from ice melting may not evaporatively precipitate sufficient abundances of carbonate to be detected using CRISM—as it is proposed to have formed <1 vol. % carbonate in martian meteorites (McSween, 1994; Niles et al., 2013)—making it a less likely origin

hypothesis than hydrothermal alteration. For ROB unit carbonates to be evaporites from regional scale water bodies, the ROB unit would need to have covered the underlying basement unit when region scale surface waters were present, as carbonates are not observed in the basement unit, which forms topographic lows in the Nili Fossae region (Scheller and Ehlmann, 2020). This is not impossible, but requires an alignment in deposition, erosion, and surface water timing that hydrothermal alteration does not, making it a more complicated and less likely carbonate formation hypothesis compared to hydrothermal alteration. Therefore, while both hydrothermal and evaporite carbonate formation are viable formation hypotheses for carbonates in the ROB unit, hydrothermal alteration is the hypothesis most favored by Ockham's razor.

5.4 Biosignature preservation potential

Hydrothermal carbonate formation may have occurred under habitable conditions within and outside of Jezero crater, which makes biosignature preservation possible. Since the margin fractured and ROB units are likely the same rock unit, then carbonates in the margin fractured unit likely have effectively the same material biosignature preservation potential as carbonates in the ROB unit, although local conditions would dictate the likelihood for biosignatures to exist within different carbonate-bearing outcrops. Low temperature hydrothermal systems in ultramafic and mafic rock carbonate olivine on Earth and can constitute habitable environments (e.g., Rempfert et al., 2017) that preserve biosignatures (e.g., Ivarsson et al., 2018, 2012; Klein et al., 2015; Newman et al., 2020). Carbonate-bearing facies in seafloor altered mafic and ultramafic rocks preserve biosignatures (Ivarsson et al.,

2018, 2012; Klein et al., 2015), as do carbonates in terrestrial serpentinites formed by groundwater alteration of ophiolites (Newman et al., 2020), and cross-cutting alteration veins in terrestrial mafic and granitic sedimentary rocks that have been altered by groundwater (Drake et al., 2017; McKinley, 2000; Onstott et al., 2019). If hydrothermal alteration occurred long after ROB unit emplacement, then near-subsurface groundwaters that connect to deep subsurface groundwater through liquid veins that cross-cut the cryosphere could introduce life from deep subsurface refugia (Michalski et al., 2013; Tarnas et al., 2018) into near-surface environments, potentially entombing it in mineralized veins. This possible connectivity to deep subsurface refugia makes groundwater-derived carbonates particularly compelling targets for biosignature preservation in Jezero crater. Minerals precipitated around surface springs from subsurface fluid systems also preserve biosignatures on Earth (Hays et al., 2017), and spring-fed carbonate precipitants in Jezero crater would have high biosignature preservation potential (McMahon et al., 2018). This makes the ROB unit a compelling target for biosignature investigation.

6.0 Conclusions

Here we detect carbonates in multiple geologic units in Jezero crater (Figure 1) as well as the ROB unit outside of and draping into Jezero crater (Figure 14). The results presented here show that carbonates within Jezero crater and in the ROB unit outside of Jezero crater have the same VNIR spectral properties—including 2.3 and 2.5 μm band depths (Figures 14f, 15a), 2.3 and 2.5 μm band depth ratios (Figures 13, 15a, S14), range in 2.3 and 2.5 μm band positions (Figure 15b)—, thermal inertia ranges (Figure 17), morphologies (Figure 16), and thicknesses

(Figure 18). The thickness of carbonate-bearing rocks in Jezero crater (at least ~ 100 m; Figure 18) is thicker than is typical of the ROB unit in the Nili Fossae region, but consistent with ROB unit thicknesses in Libya Montes (Kremer et al., 2019). These combined observations from all available high spatial resolution orbital datasets implies that carbonates within and outside of Jezero have the same emplacement and alteration history. Estimated carbonate compositions range from Mg-carbonate to (Fe,Mg)-carbonate (Figure 15b), in agreement with past estimations (Ehlmann et al., 2008b; Horgan et al., 2020a; Zastrow and Glotch, 2021). Hydrated silica in smooth dark-toned material (Figures 11, S12) sometimes covers carbonate-bearing outcrops in Jezero crater (Figure 12), imparting a $2.2 \mu\text{m}$ absorption. Minerals detected in assemblage with carbonate in relatively uncovered, high thermal inertia bedrock outcrops include Fe/Mg-phyllosilicates, olivine, and either Al-phyllosilicate or hydrated silica (Figures 3e, 4d, 5d, 6c, 7d, 8e, 9e, 10e, 12e, S1d, S2d, S3c, S4c, S5d, S6c, S7c, S8d, S9d, S10d, S13). The combination of evidence presented here is consistent with carbonate formation in the ROB unit via hydrothermal or evaporative processes, as has been proposed for Comanche carbonate formation in Columbia Hills (Morris et al., 2010; Ruff et al., 2014) and carbonate formation in martian meteorites (Bridges and Grady, 2000; McSween and Harvey, 1998; Steele et al., 2007; Treiman et al., 2002; Warren, 1998). The conclusions of this study are summarized below.

1) Carbonate and hydrated silica-bearing units in Jezero crater. There are VNIR spectral absorptions consistent with carbonate in CRISM data covering (1) high TI bedrock in the margin fractured unit (Figure 3, S1-S5), (2) large aeolian bedforms proximal to the margin fractured unit (Figures 4, S6-S7), (3) the delta blocky unit (Figure 5), (4) the delta truncated curvilinear

unit (Figure 6), (5) undifferentiated smooth material on the western delta (Figures 7, S8), (6) the delta layered rough unit (Figures 8, S9), (7) moderate TI bedrock in the crater floor fractured 2 (CFF 2) unit (Figures 9, S10-S11), and (8) low TI dunes and unconsolidated dark-toned material in the CFF 2 unit (Figure 10). We also find five previously unreported outcrops of hydrated silica in the same dark-toned material that Tarnas et al. (2019) and Dundar et al. (2019) reported hydrated silica in (Figures 11-12, S12).

2) Minerals in assemblage with carbonate in Jezero crater. Carbonate-bearing rocks in the crater floor fractured 2 unit also have absorption features consistent with a mixture of olivine, carbonate, Fe/Mg-phyllsilicate(s), and hydrated silica and/or Al-phyllsilicate (Figures 9-10, S10-S11). VNIR spectra with carbonate absorptions in the deltaic unit have deeper and narrower 2.3 μm absorptions compared to carbonate spectra elsewhere in the crater (Figures 5-8, S8-S9), implying a higher spectral abundance of Fe/Mg-phyllsilicate(s). These spectra also have 2.2 μm absorption features consistent with hydrated silica and/or Al-phyllsilicate and a broad 1.0 μm band consistent with olivine and/or siderite (Figures 3e, 4d, 5d, 6c, 7d, 8e, 9e, 10e, 12e, S1d, S2d, S3c, S4c, S5d, S6c, S7c, S8d, S9d, S10d, S13). The margin fractured unit and proximal aeolian bedforms have spectra consistent with a mixture of olivine and/or siderite, carbonate, and Fe/Mg-phyllsilicate(s) (Figure 3-4, S1-S7). As reported by Horgan et al. (2020a), rocks in the margin fractured unit have the lowest 2.3/2.5 μm band depth ratios in Jezero crater, consistent with a higher spectral abundance of carbonate (Figure 13a).

3) Carbonates in the Nili Fossae region have the same VNIR spectral properties inside and outside of Jezero crater. Qualitatively, the carbonate VNIR spectra extracted from inside and outside of Jezero crater show the same variability in absorption depth, shapes, and position (Figure 14f). Quantified 2.3 and 2.5 μm band depths also show the same trend and variability within and outside of Jezero crater (Figure 15a), and demonstrated that the band depth variability of carbonates in Jezero is subtended by band depth variability of carbonates in the ROB unit outside of Jezero. The absorption minima wavelength positions of the 2.3 and 2.5 μm absorptions also have the same values and variability within and outside of Jezero crater (Figure 15b). Carbonates in the margin fractured unit have the lowest 2.3/2.5 μm band depth ratios observed inside Jezero crater, and there are widespread outcrops with similar 2.3/2.5 μm band depth ratios in the ROB unit 100-200 km NNE of Jezero crater (Figures 13, S14), as well as immediately outside of Jezero crater (Figure 13a). Overall, the VNIR spectral properties of carbonates within and outside of Jezero crater are highly similar, showing that Jezero carbonates are not unique in a regional context.

4) Carbonate chemistries range from Mg-rich to Fe/Mg-rich. Carbonate chemistry can be estimated using the wavelength positions of the minima of the 2.3 and 2.5 μm absorption features (Gaffey, 1987). The wavelength positions of these absorption minima for carbonates within and outside of Jezero crater fall within the range expected for Mg-carbonate and (Fe,Mg)-carbonate (Figure 15b), demonstrating that carbonates in this region span a solid solution from more Mg-rich to more Fe-rich, as commonly occurs in nature. This carbonate chemistry is also consistent with that expected from carbonation of olivine with the range of

compositions estimated for olivine in the ROB unit of ~25-75% Fe-olivine and ~25-75% Mg-olivine (Brown et al., 2020; Clenet et al., 2013; Koeppen and Hamilton, 2008). Such Mg-rich carbonates could likely only precipitate as evaporites in low temperature playa environments formed by rapidly receding floodwaters (McSween and Harvey, 1998; Niles et al., 2013; Warren, 1998). The Fe/Mg-carbonate chemistries estimated here are similar to those estimated for the Comanche carbonate in Columbia Hills (Morris et al., 2010). Along with the similarities in proposed ashfall origins for the olivine-bearing components of both the ROB unit (Kremer et al., 2019; Mandon et al., 2020) and the Algonquin/Comanche rocks (McCoy et al., 2008; McSween et al., 2008; Morris et al., 2010; Ruff et al., 2014), high thermal inertia values of both rock units consistent with other clastic rocks on Mars (Rogers et al., 2018), and estimated Noachian ages for both rock units (Greeley et al., 2005; Mandon et al., 2020; McCoy et al., 2008), this similarity in estimated carbonate chemistries provides further evidence of similar emplacement and alteration histories for these rocks.

5) Carbonates in the Nili Fossae region have the same thermal inertia properties inside and outside of Jezero crater. Non-deltaic carbonates within and outside of Jezero crater share the same distribution of thermal inertia values (Figure 17), indicative of similar physical rock properties and levels of dust coverage (Rogers et al., 2018). This range in thermal inertia values is similar to other bedrock exposures on Mars interpreted to be clastic (Rogers et al., 2018)—including Columbia Hills—which is consistent with an ashfall hypothesis for the ROB unit (Kremer et al., 2019; Mandon et al., 2020). There is higher areal coverage of low thermal inertia carbonate-bearing rocks within Jezero crater compared to outside of Jezero crater (Figure 17)

due to the presence of carbonate-bearing dunes in Jezero crater (Figures 4, 10, S6-S7), which are not detected elsewhere in the Nili Fossae region. This is likely indicative of variability in aeolian processes within and outside of Jezero crater, which affect the redistribution of unconsolidated material on the Amazonian martian surface. Overall, the matching range and distribution of thermal inertia values for non-deltaic carbonate-bearing materials within and outside of Jezero crater implies a shared depositional origin and alteration history for these rocks.

6) Outcrops of the margin fractured unit are at least 100 meters thick. An exposed cross-section of carbonate-bearing rocks in Jezero crater, which shows possible banding, is at least ~100 meters thick (Figure 18). This is atypical of the ROB unit in the Nili Fossae region, which typically has exposed cross-sections thicknesses ranging from 1-25 meters (Kremer et al., 2019), but similar to exposures of the ROB unit in Libya Montes, where outcrop cross-sections reach thicknesses of ~100 meters (Kremer et al., 2019). The ROB unit is also carbonated in Libya Montes (Bishop et al., 2013b). The ROB unit has high thermal inertia, which is characteristic of friable clastic rocks on Mars (Rogers et al., 2018), and is surrounded by both olivine- (Brown et al., 2020; Edwards and Ehlmann, 2015) and carbonate-bearing (Figures 4, S6-S7) aeolian bedforms, indicating that it has undergone substantial erosion. As such, it is likely that the ROB unit was originally deposited as a thicker rock unit than it is today, meaning the thickness difference between ROB unit outside of Jezero crater and the margin fractured unit along the crater rim interior could be explained by differential erosion. The crater rim may have

protected this part of the ROB unit from erosion via buttressing against mass wasting and protection from aeolian weathering.

7) Non-deltaic carbonate bearing rocks in Jezero crater are likely components of the ROB unit.

The stark similarities between the ROB unit outside of Jezero crater and non-deltaic carbonate-bearing rocks inside of Jezero crater implies that these rocks share the same emplacement and alteration history, and thus are part of the same unit. This is the same hypotheses presented by Goudge et al. (2015), who also determined that the properties of carbonate-bearing rocks in Jezero crater were nonunique in the context of the surrounding region.

8) Hydrothermal alteration is the most viable formation hypothesis for carbonate in the ROB unit. Hydrothermal and/or evaporitic processes have been proposed as origins for the Comanche carbonate (Morris et al., 2010; Ruff et al., 2014)—which shares many characteristics with the ROB unit—as well as in ALH 84001 and nakhlite martian meteorites (Bridges and Grady, 2000; Halevy et al., 2011; McSween and Harvey, 1998; Steele et al., 2007; Treiman et al., 2002; Warren, 1998). If carbonate formation conditions were habitable, as occurs on Earth in both evaporitic and hydrothermal settings, biosignatures could be preserved in either carbonate evaporites (Bosak et al., 2021) or hydrothermal precipitants (e.g., Drake et al., 2017; McKinley, 2000; Newman et al., 2020; Onstott et al., 2019). Evaporation of low amounts of infiltrating surface water (e.g., Knauth et al., 2003) is a viable formation hypothesis for non-deltaic carbonates within and outside of Jezero crater, but would likely not generate the 20-25% carbonate modal abundances estimated for the entire ROB unit using CRISM (Edwards and

Ehlmann, 2015). Evaporite carbonate formation could also be possible if a martian ocean or ice-dammed regional scale lakes covered the Nili Fossae region, and if the ROB unit covered the entire region during the time that these large surface water bodies were present. Some estimates for Mars ocean shorelines show the Nili Fossae and Libya Montes regions on the margins of these hypothesized oceans (Sholes et al., 2021), and layered sulfate deposits up to ~600 m thick are evidence for large surface water bodies in the Nili Fossae region (Quinn and Ehlmann, 2019), making this a theoretically viable hypothesis. However, the timing of ROB unit emplacement, erosion, and the presence of regional scale surface water bodies would need to precisely align for evaporite carbonate precipitation exclusively in the ROB unit, making this carbonate formation hypothesis unlikely compared to surface water infiltration or hydrothermal alteration.

Hydrothermal alteration could have occurred during emplacement of the ROB unit, particularly if this unit is an ashfall deposit (Kremer et al., 2019; Mandon et al., 2020), with volatiles being assimilated from the underlying hydrated basement unit (Brown et al., 2010) and/or assimilated from the atmosphere (Edwards and Ehlmann, 2015). Carbonation under hydrothermal conditions could also occur after emplacement of the unit, similar to what forms listvenite (e.g., Beinlich et al., 2020; Falk and Kelemen, 2015) and many carbonated mafic rocks (e.g., Alfredsson et al., 2013; Costello et al., 2020; Morris et al., 2011; Treiman et al., 2002) on Earth. Estimated Nili Fossae carbonate chemistries are solid solutions of FeCO_3 and MgCO_3 (Figure 15b), similar to the Fe/Mg solid solution olivine chemistry in the Nili Fossae region (Brown et al., 2020; Clenet et al., 2013; Koeppen and Hamilton, 2008). Carbonate chemistries within and outside of Jezero crater are therefore those expected from carbonation of the ROB

unit olivine, consistent with a hydrothermal olivine carbonation process. We therefore conclude that hydrothermal carbonation of olivine within the ROB unit likely formed non-deltaic carbonates within and outside of Jezero crater.

Observations by the Mars 2020 Perseverance rover will definitively identify the emplacement and alteration mechanisms that formed these carbonate-bearing rocks within and outside of Jezero crater, as well as their potential to host biosignatures.

Acknowledgments

Many thanks to Benjamin Bultel and Paul Niles for reviews that substantially improved the quality of this manuscript. J.D.T. was funded by a NASA Postdoctoral Fellowship to work at the NASA Jet Propulsion Laboratory. E.A.C. thanks the Canadian Space Agency, the Natural Sciences and Engineering Research Council of Canada, the Canada Foundation for Innovation, and the Manitoba Research Innovation Fund for supporting this work. This research was carried out at the Jet Propulsion Laboratory, California Institute of Technology, under a contract with the National Aeronautics and Space Administration (80NM0018D0004). © 2021. All rights reserved.

Data availability

CRISM, THEMIS, and HiRISE images are available on NASA's Planetary Data System (PDS) archive (<https://pds.nasa.gov/>). Orthorectified CTX and HiRISE image and digital terrain map mosaics of Jezero crater are generated by and available from USGS (HiRISE mosaic:

doi.org/10.5066/P9QJDP48; HiRISE DTM: doi.org/10.5066/P9REJ9JN; CTX mosaic:

doi.org/10.5066/P9GV1ND3; CTX DTM: doi.org/10.5066/P906QQT8; Ferguson et al., 2020).

Orthorectified CTX and HiRISE image and digital terrain mosaics of Jezero crater and its watershed rock units are generated by and available from The Murray Lab at the California Institute of Technology (<http://murray-lab.caltech.edu/Mars2020/index.html>), as is a global CTX mosaic used in this study (<http://murray-lab.caltech.edu/CTX/index.html>; Dickson et al., 2020). The THEMIS thermal inertia mosaic covering Jezero crater is generated by and available from Northern Arizona University (Edwards and Buz, 2021). Atmospherically corrected CRISM data, CRISM data processed through the University of Massachusetts at Amherst correction pipeline (Itoh and Parente, 2021), derived spectral products, regions of interest (ROIs) used to extract CRISM spectra and THEMIS thermal inertia estimates, THEMIS thermal inertia data, library spectra, and codes used in this study are available at <https://zenodo.org/record/5525282#.YV9vXBDMKHF>. Some codes used in this study were downloaded from Dr. Honglei Lin's GitHub page (<https://github.com/linhoml?tab=repositories>; Lin et al., 2020). Other library spectra used in this study are available from the RELAB PDS database (<https://pds-geosciences.wustl.edu/spectrallibrary/default.htm>).

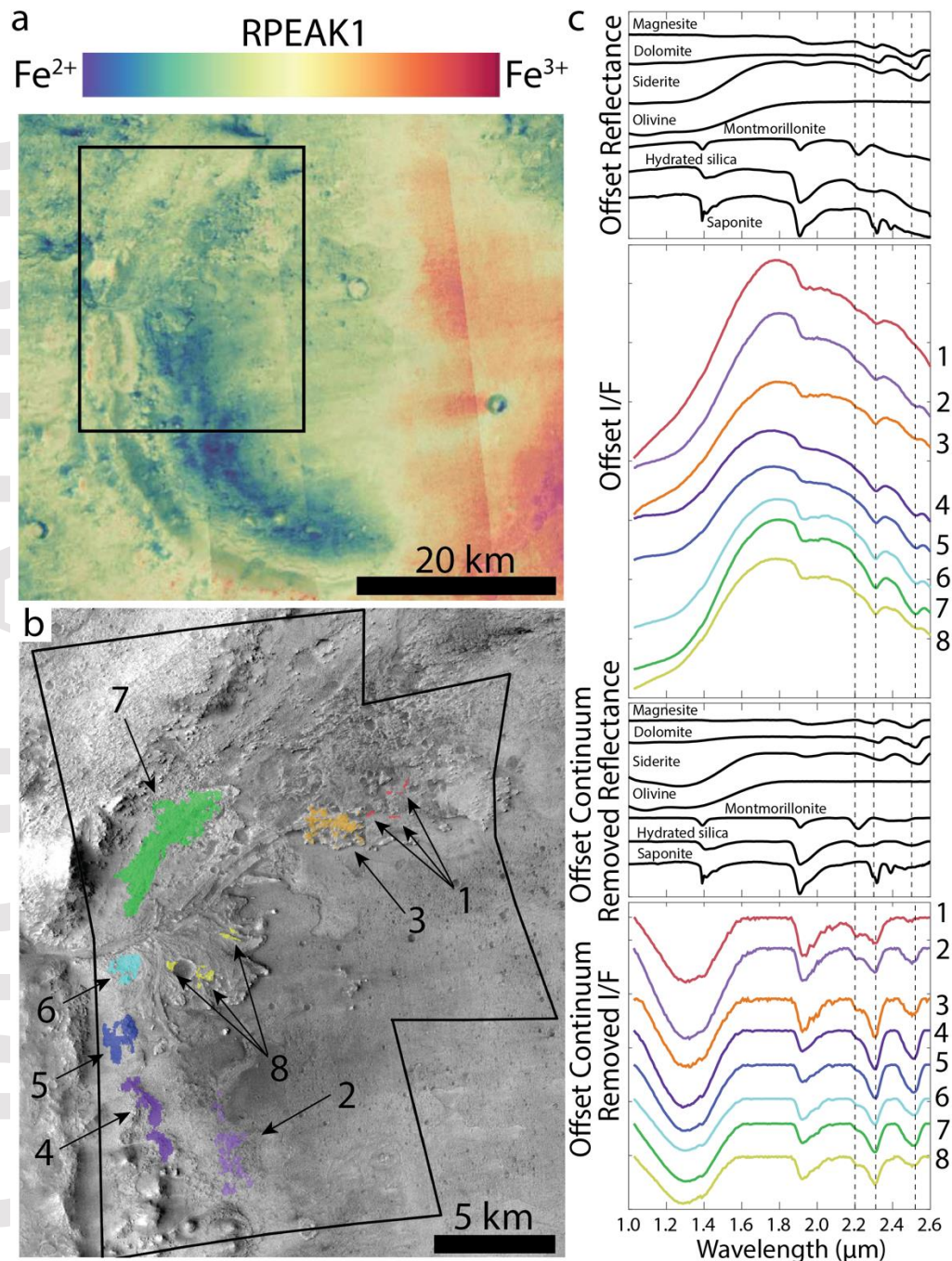


Figure 1 | Overview of Jezero crater carbonate-bearing rocks. (a) RPEAK1 parameter map of CRISM Multispectral TRDR image mosaic, which corresponds to presence of ferric (red color) and ferrous (blue color) Fe. Ferric iron is attributed to presence of martian dust, which occludes spectral signals in the visible-to-near-infrared wavelengths measured by CRISM. The western region of Jezero crater has lower dust coverage, and therefore be less spectrally dominated by dust. (b) Carbonate-bearing rocks are present in the delta truncated curvilinear layered, delta blocky, and undifferentiated smooth units (8), the delta layered rough unit (3), the crater floor fractured 2 unit (2), the margin fractured unit and proximal large aeolian bedforms (4-7) described in Stack et al. (2020). Silica-bearing material is identified in the smooth dark-toned

material described in Tarnas et al. (2019). The combined footprints of CRISM images HRL000040FF and FRT000047A3 are shown as black lines. The regions of interest from which these spectra were extracted are analyzed in greater detail in Figures 3-12, S1-S12. CTX mosaic from Dickson et al. (2018). The colors show the pixels from which the spectra shown in (c) were extracted. Colors and numbers correlate between (b) and (c). (c) Spectra from the University of Massachusetts at Amherst processed CRISM data shown with (bottom) and without (top) continuum removal. RELAB IDs for the library spectra are CACB08, CABE256, CACB03, 397S013, C1SA51, C1RM34, and C1DH07, and these same library spectra are used in Figures 3-12, 14, 18, S1-S10, and S12.

Accepted Article

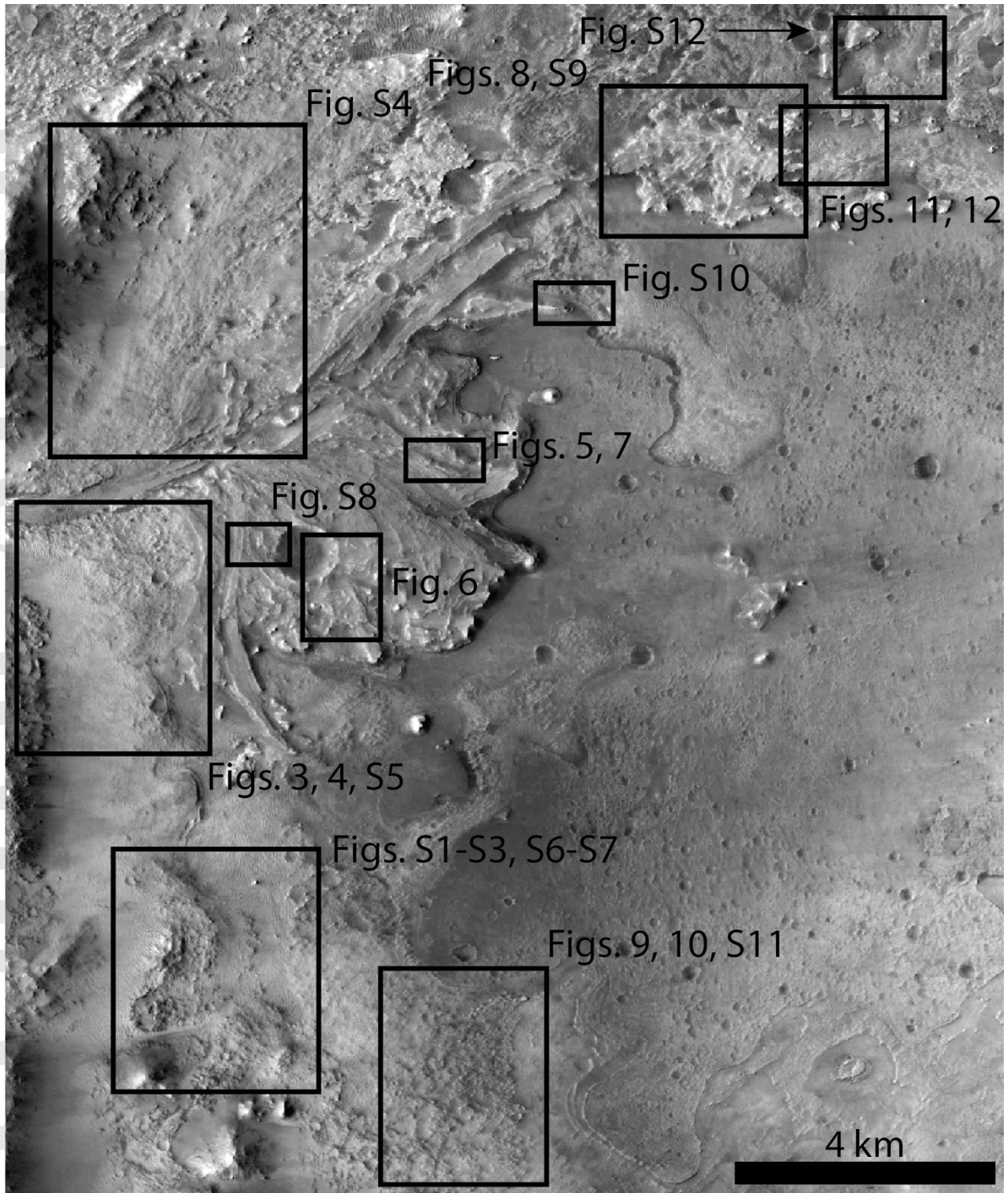


Figure 2 | Locations of Jezero crater sites characterized in this study.

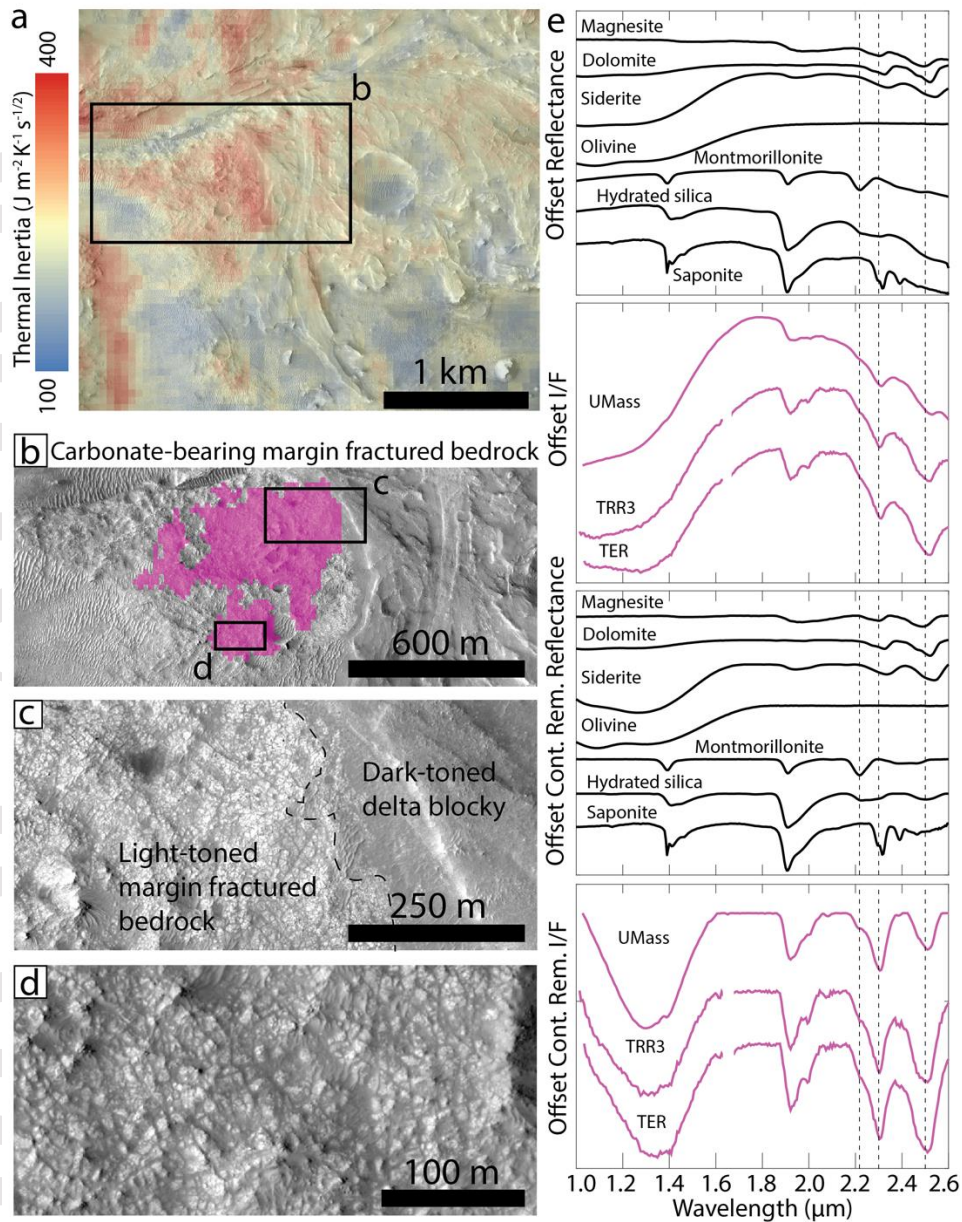


Figure 3 | Carbonate and phyllosilicate-bearing bedrock in the margin fractured unit. (a) THEMIS thermal inertia map from Edwards and Buz, (2021) covering region of interest. (b) CRISM pixels (pink) for spectra shown in (e). These CRISM pixels cover light-toned fractured bedrock with notably high thermal inertia. (c) Enlarged view of light-toned margin-fractured unit bedrock and contact with dark-toned delta blocky unit material. (d) Enlarged view of light-toned margin fractured unit bedrock. (e) UMass, TRR3, And TER CRISM spectra of pink pixels shown in (b). The 2.3 and 2.5 μm features are consistent with the presence of carbonate-bearing rock. The ratio of the 2.3/2.5 μm absorptions is consistent with presence of some phyllosilicate-bearing material. The absorption centered at 1.0 μm may be due to presence of olivine or presence of siderite.

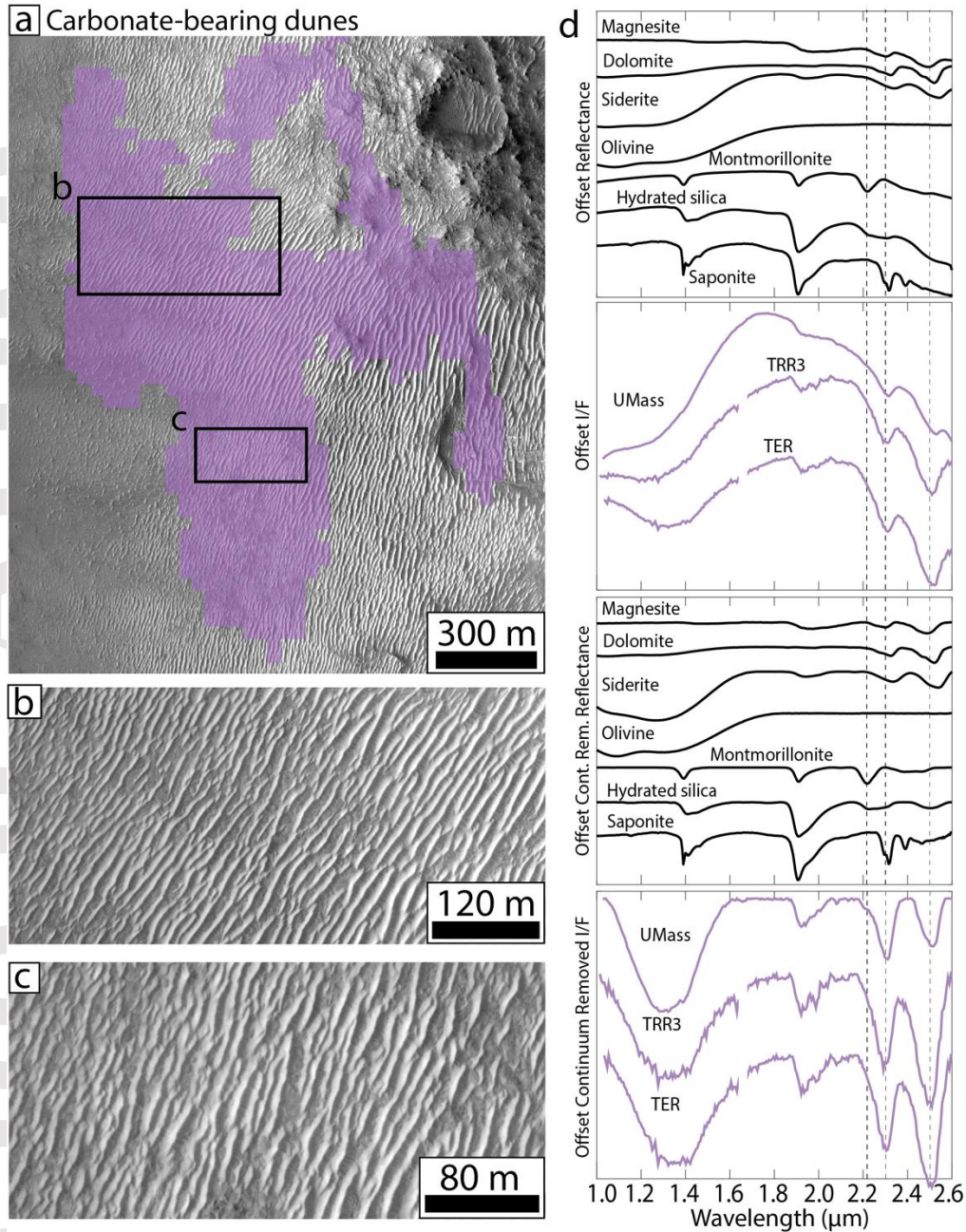


Figure 4 | Carbonate and phyllosilicate-bearing aeolian bedforms proximal to margin fractured unit. (a) CRISM pixels (purple) for the spectra shown in (d). These pixels cover aeolian bedforms immediately west of the margin fractured bedrock shown in Figure S5. (b-c) Enlarged views of carbonate and phyllosilicate-bearing aeolian bedforms. (d) UMass, TRR3, and TER CRISM spectra from purple pixels shown in (a). The spectral interpretation is the same as described in Figure 3. This aeolian material is therefore interpreted to derive from the proximal margin fractured unit bedrock.

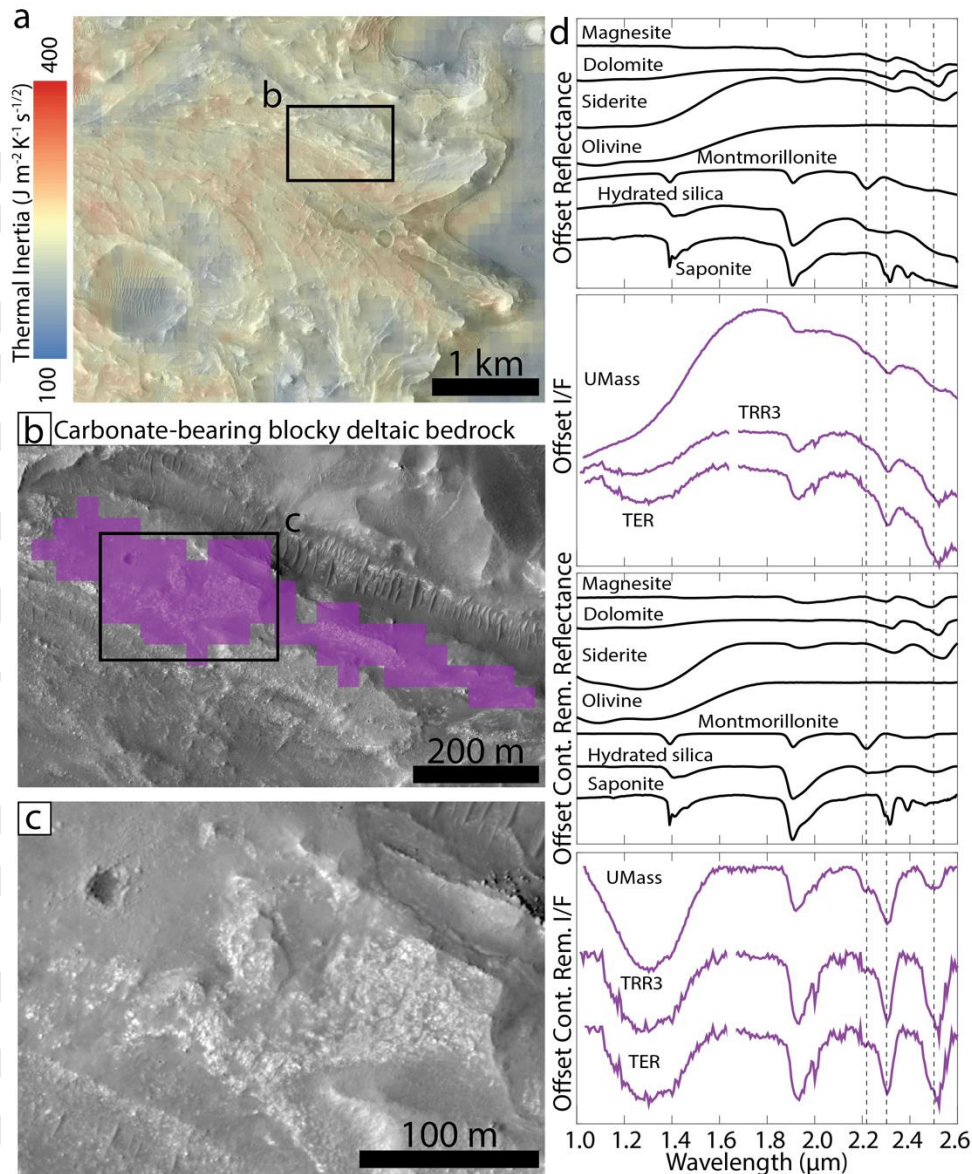


Figure 5 | Carbonate and phyllosilicate-bearing rock in the western Jezero delta blocky unit. (a) THEMIS thermal inertia map from Edwards and Buz, (2021) covering region of interest. (b) CRISM pixels (purple) for spectra shown in (d), which cover light and dark-toned bedrock in the delta blocky unit. (c) Enlarged view of light and dark-toned bedrock. (d) UMass, TRR3, And TER CRISM spectra from purple pixels shown in (b). The 2.3 and 2.5 μm absorptions are consistent with the presence of carbonate-bearing rock. The 2.3/2.5 μm absorptions are consistent with the presence of phyllosilicate-bearing material. The small absorption at 2.2 μm is consistent with the presence of either hydrated silica and/or Al-phyllosilicate. Overall, this composition resembles the crater floor fractured 2 unit, but with a stronger 2.3 μm feature, consistency with stronger spectral presence of phyllosilicates.

a Carbonate-bearing truncated curvilinear layered deltaic unit

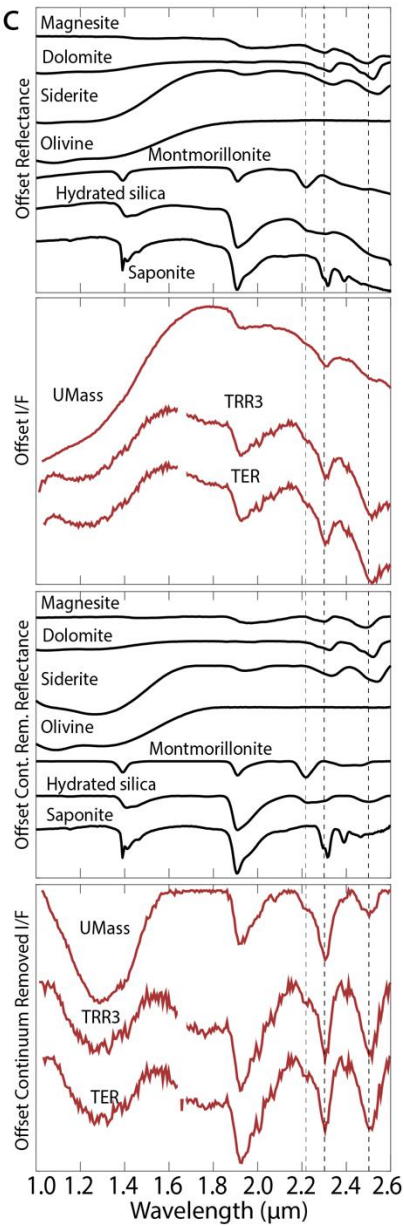
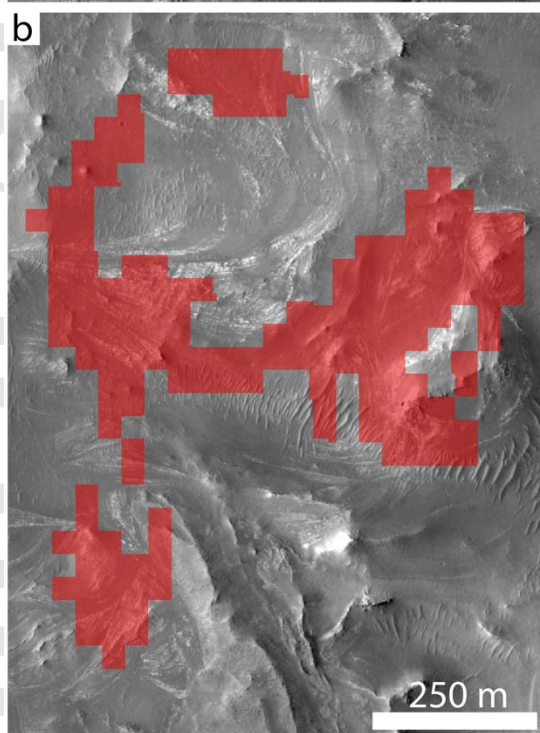
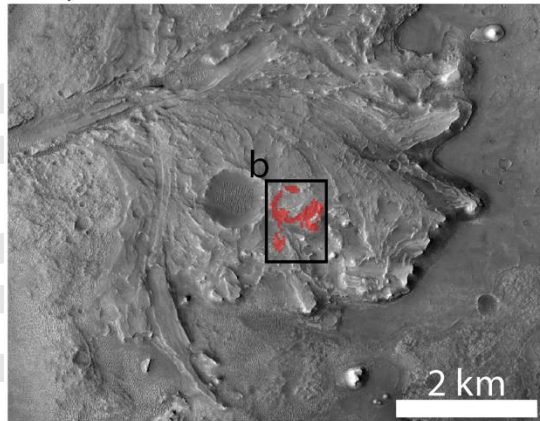


Figure 6 | Carbonate and phyllosilicate-bearing rock in the western Jezero delta truncated curvilinear layered unit. (a) Regional view of reported compositional detections from CRISM pixels shown in red. (b) CRISM pixels (red) for spectra shown in (c), which cover possible point bar strata in the delta truncated curvilinear layered unit (Goudge et al. 2018). (c) UMass, TRR3, And TER CRISM spectra from red pixels shown in (a & b). The spectral interpretation is the same as described in Figure 5, but is present on a different deltaic unit.

a Carbonate-bearing undifferentiated smooth deltaic unit cover

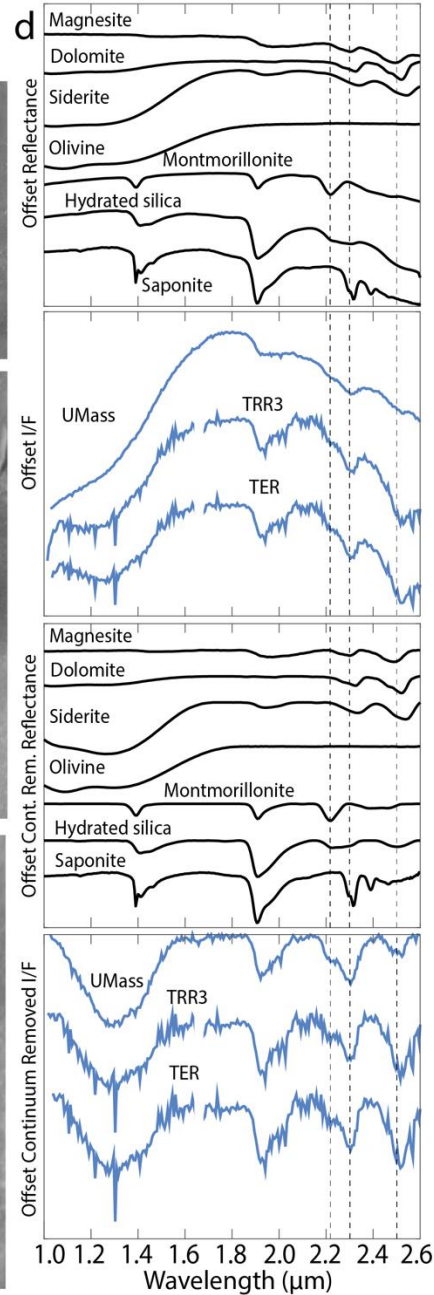
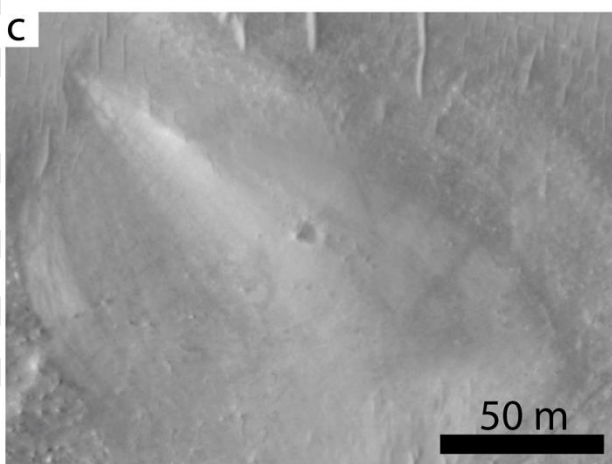
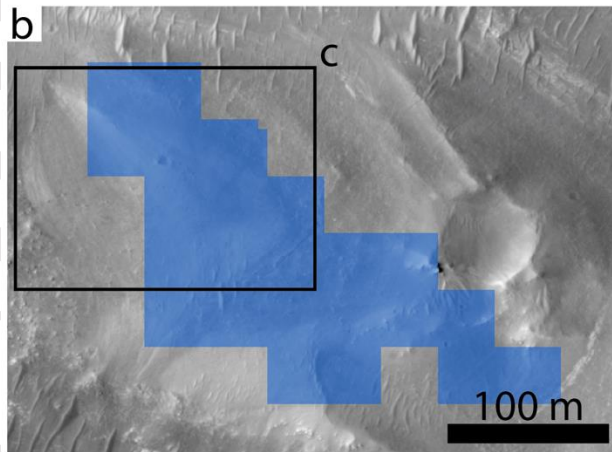
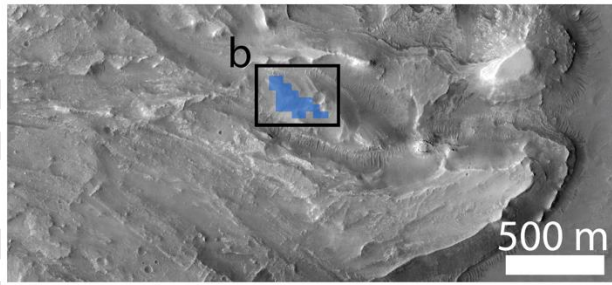


Figure 7 | Carbonate and phyllosilicate-bearing rock in the western Jezero delta undifferentiated smooth unit.

(a) Regional view of reported compositional detections from CRISM pixels shown in blue. (b) CRISM pixels (blue) for spectra shown in (c), which cover primarily dark-toned bedrock in the delta undifferentiated smooth unit. (c) UMass, TRR3, and TER CRISM spectra from blue pixels shown in (a & b). The spectral interpretation is the same as described in Figure 5, but is present on a different deltaic unit.

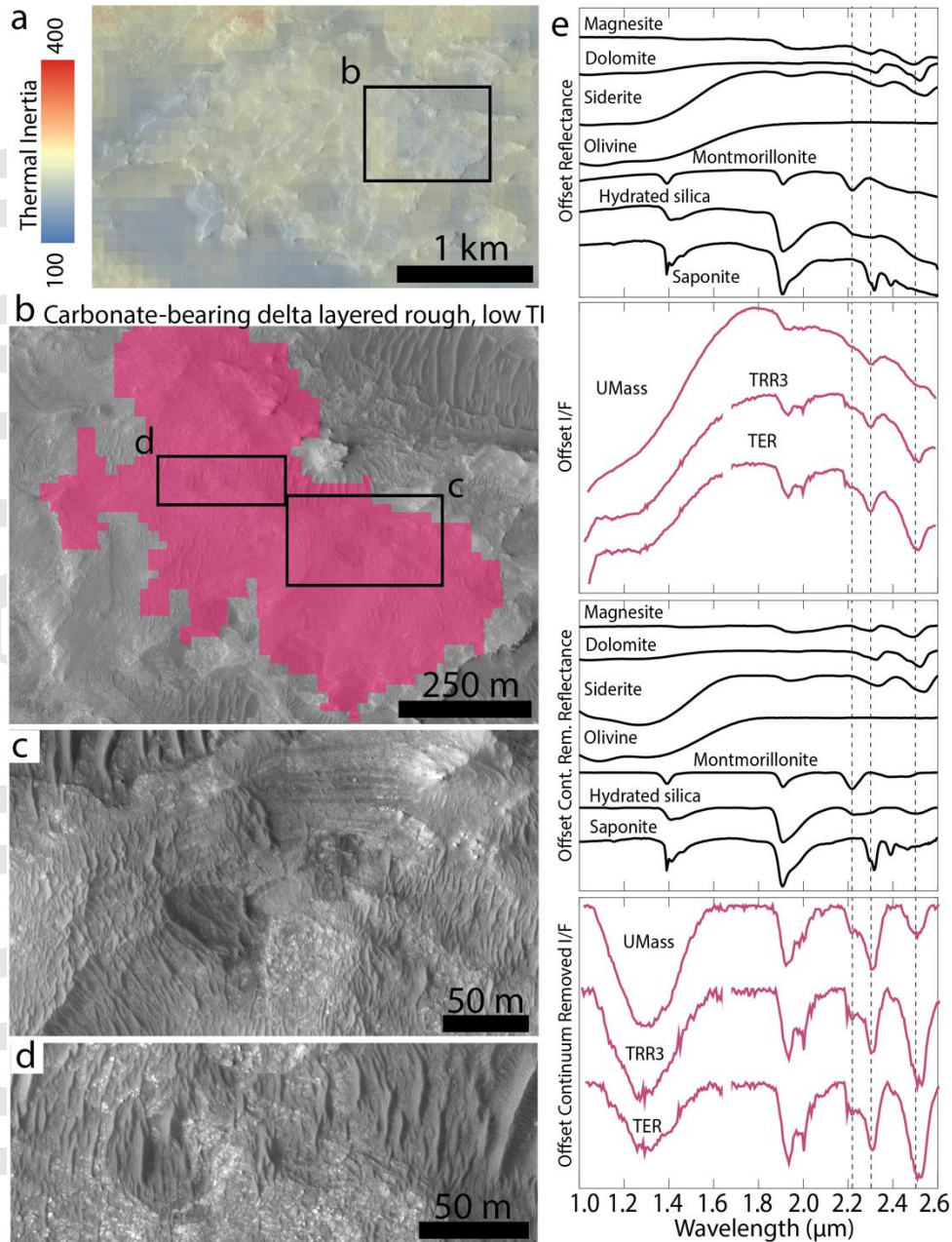


Figure 8 | Carbonate and phyllosilicate-bearing rock in the northern Jezero delta layered rough unit with low thermal inertia. (a) THEMIS thermal inertia map from Edwards and Buz, (2021) covering region of interest. (b) Regional view of reported compositional detections from CRISM pixels shown in pink, which cover the northern delta low thermal inertia surface component. (c) Enlarged view of layered rocks in low thermal inertia northern delta, covered by aeolian bedforms. (d) Enlarged view of light-toned rocks in low thermal inertia northern delta, covered by aeolian bedforms. (e) UMass, TRR3, And TER CRISM spectra from pink pixels shown in (b). The spectral interpretation is the same as described in Figure 5, but is present on a different deltaic unit.

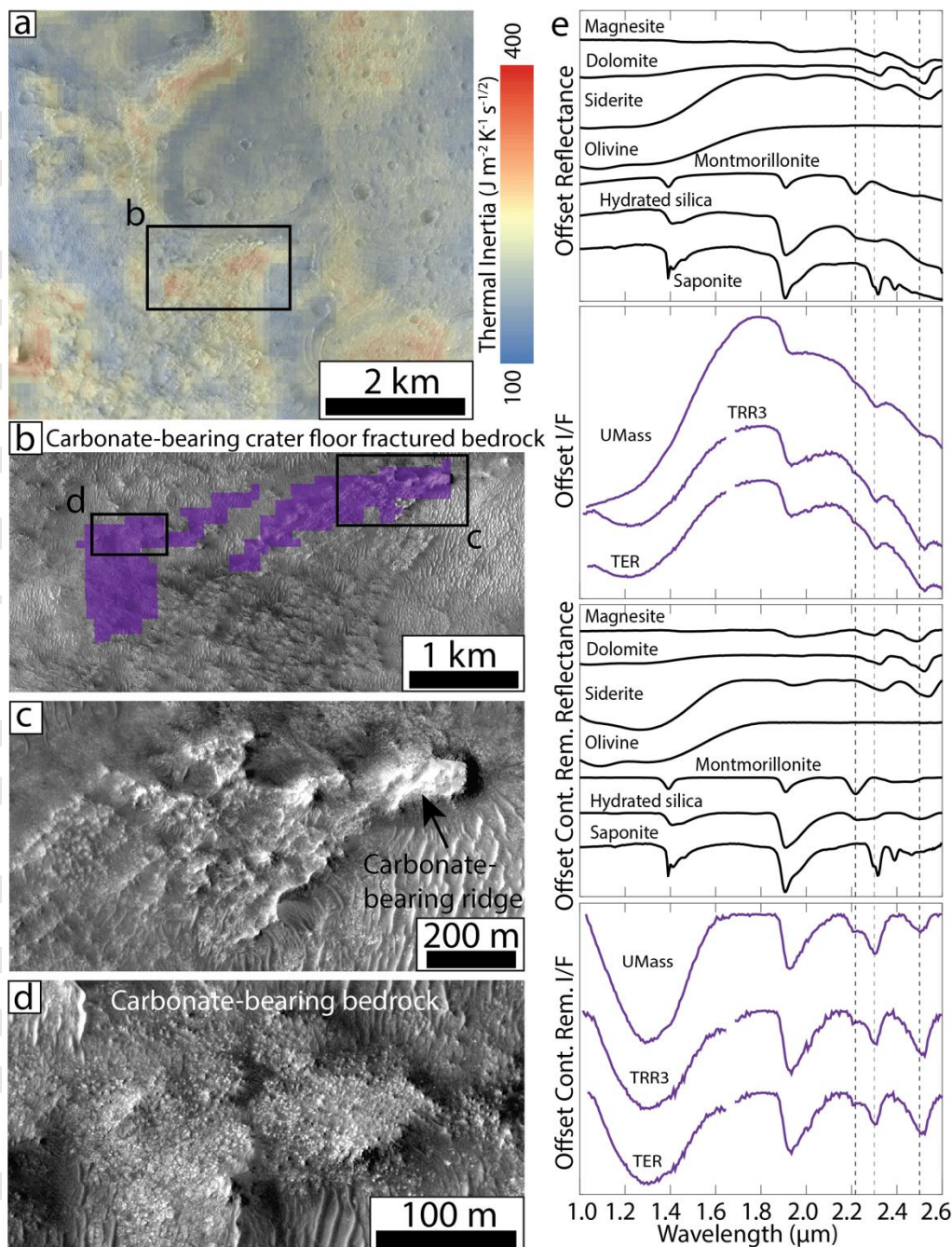


Figure 9 | Carbonate, silica, and olivine-bearing bedrock. (a) THEMIS thermal inertia map from Edwards and Buz, (2021) covering region of interest, coregistered to CTX and HiRISE mosaics by Dickson et al. (2018). Warmer colors correspond to more consolidated (warmer colors) and less consolidated (cooler colors) materials. (b) CRISM pixels (purple) on HiRISE image from which the spectra shown in (e) are derived. The CRISM pixels were selected based on THEMIS thermal inertia and HiRISE data to cover bedrock in the crater floor fractured 2 unit. (c) Enlarged view of a ridge in the crater floor fractured 2 unit (Stack et al. 2020). (d) Enlarged view of rubbly bedrock in the crater floor fractured 2 unit. (e) Spectra from UMass, TRR3, And TER processed

CRISM data (purple) extracted from the pixels shown in (b) and compared to laboratory spectra of dolomite (RELAB ID C1CY07) and hydrated silica. The spectra are consistent with the presence of carbonate-bearing rock based on the presence of 2.3 and 2.5 μm features. The ratio of 2.3/2.5 μm band depth and narrow shape of the 2.3 μm feature are also consistent with the presence of phyllosilicate-bearing rock. The absorption at 2.2 μm , which combines with the 2.3 μm absorption to create a broad band, is consistent with the presence of hydrated silica and/or Al-phyllosilicate. The absorption centered at 1.0 μm is consistent with the presence of olivine-bearing rock, which is widespread throughout this unit. Hydrated silica is a product of carbonation of olivine (Falk & Kelemen, 2015). The thermal inertia, visible texture and topography, geologic context, and VNIR spectra of this outcrop are consistent with carbonate, hydrated silica, and olivine-bearing bedrock.

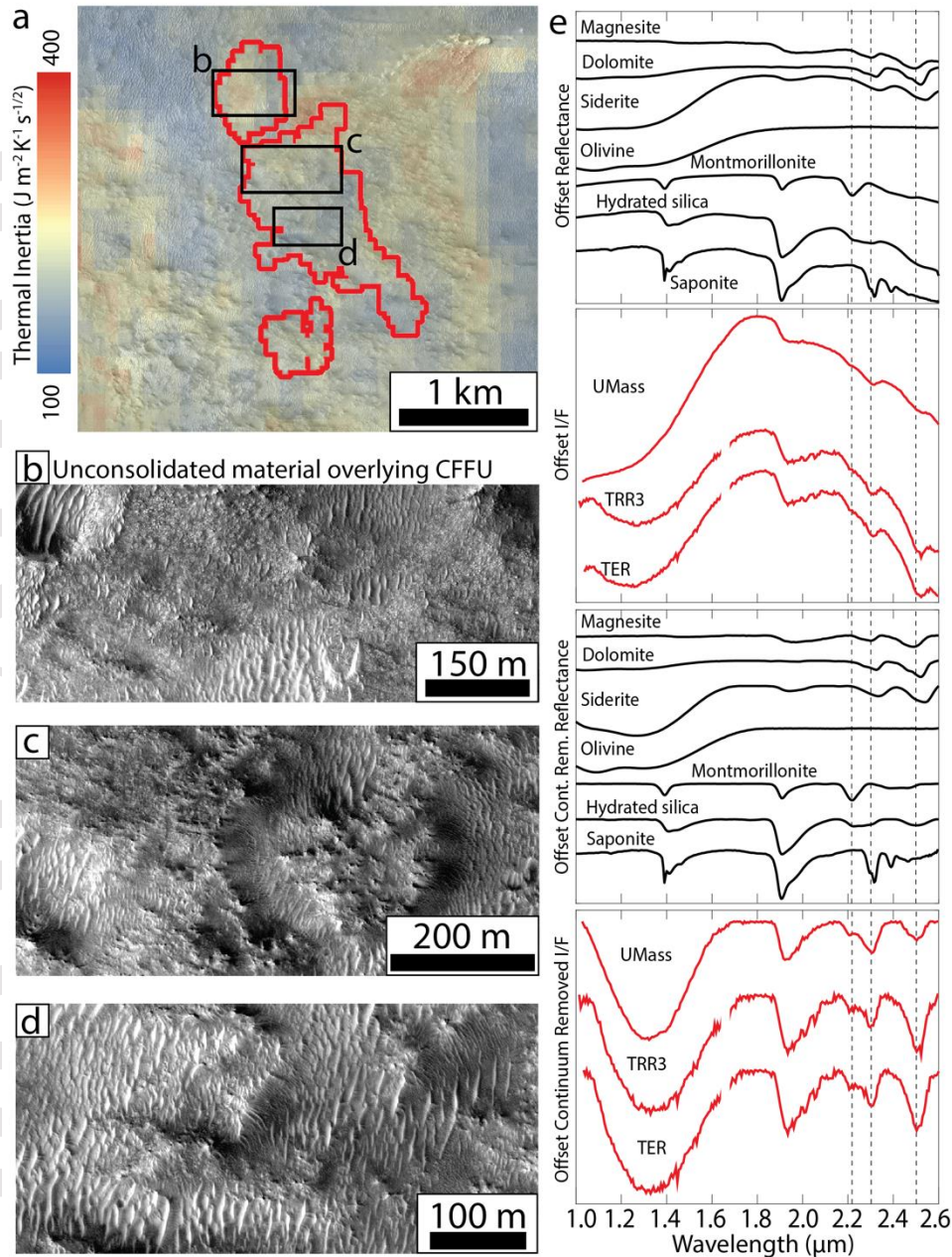


Figure 10 | Olivine, carbonate, phyllosilicate, and silica-bearing unconsolidated material in crater floor fractured 2 unit. (a) THEMIS thermal inertia map from Edwards and Buz, (2021) covering region of interest. The CRISM pixels for the spectra in (e), which are within the red outlines, cover dunes and unconsolidated dark-toned material that has low thermal inertia. (b) Enlarged view of dunes and dark-toned unconsolidated dark-toned material overlying bedrock, which in some locations protrudes through this material. (c) Enlarged view of dunes and knobby bedrock that is covered by dark-toned unconsolidated material. (d) Enlarged view of dunes and unconsolidated dark-toned material overlying bedrock. (e) UMass, TRR3, and TER processed CRISM spectra from pixels shown in (b) compared to library spectra of dolomite and hydrated silica. The spectral features are the same as those described for bedrock in Figure 9, implying

that the dunes and unconsolidated dark-toned material are locally sourced and have the same composition as the proximal and underlying crater floor fractured 2 unit bedrock.

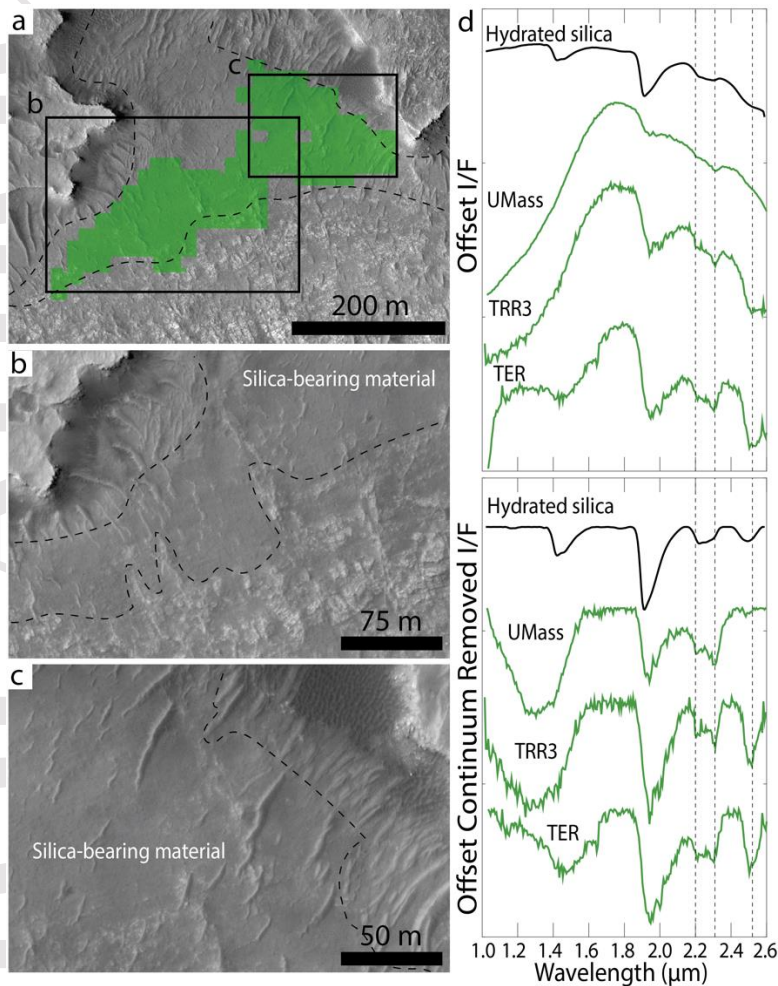


Figure 11 | Smooth dark-toned silica-bearing material overlying crater floor fractured unit. (a) CRISM pixels (green) for the spectra shown in (d). These pixels cover the smooth dark-toned material reported to be silica-bearing by Tarnas et al. (2019). (b) Enlarged view of smooth dark-toned silica-bearing material overlying the crater floor fractured unit. (c) Another enlarged view of smooth dark-toned silica-bearing material overlying the crater floor fractured unit. (d) UMass, TRR3, And TER CRISM spectra from green pixels shown in (a). These spectra are consistent with hydrated silica and the Jezero crater hydrated silica detections reported in this material in different locations by Tarnas et al. (2019).

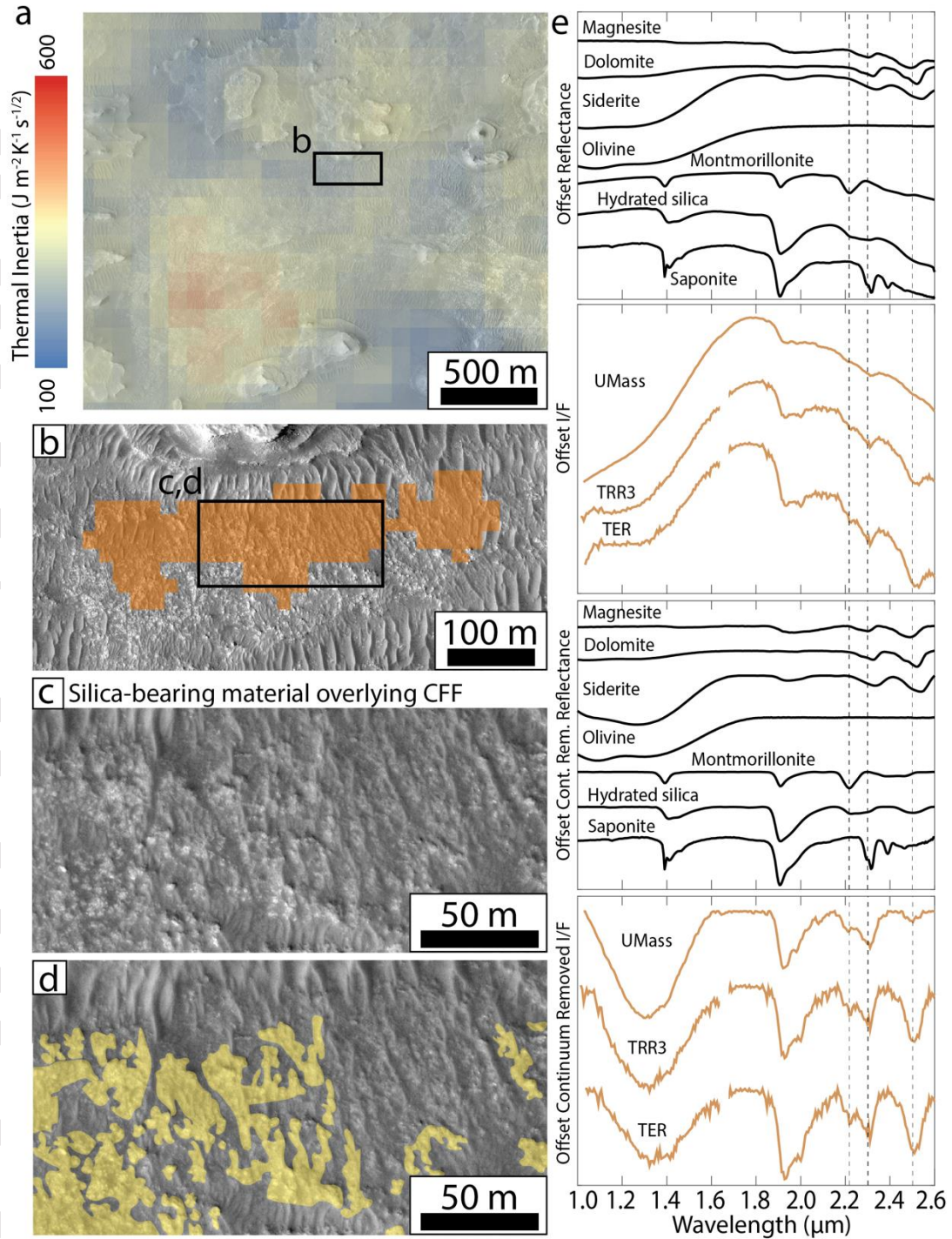


Figure 12 | Silica-bearing material overlying crater floor fractured unit. (a) THEMIS thermal inertia map from Edwards and Buz, (2021) covering region of interest. The area of interest (within the black outline) has moderate thermal inertia. (b) CRISM pixels for the spectra in (e) shown in orange. (c) Enlarged view of dark-toned unconsolidated material overlying crater floor fractured unit bedrock. (d) Same image as (c), but with crater floor fractured unit bedrock mapped in yellow. Most of the area covered by the CRISM pixels shown in (a) is comprised of dark-toned unconsolidated material. (e) UMass, TRR3, And TER CRISM spectra of pixels shown

in (a). The broad 2.2 μm feature is consistent with the presence of hydrated silica, which was also reported in smooth dark-toned material in Jezero crater by Tarnas et al. (2019). The additional 2.3 μm absorption that merges with the 2.2 μm features is consistent with the presence of phyllosilicate-bearing material. The geologic context, visible properties, and spectra of this outcrop are consistent with hydrated silica-bearing dark-toned unconsolidated material overlying phyllosilicate-bearing crater floor fractured unit bedrock.

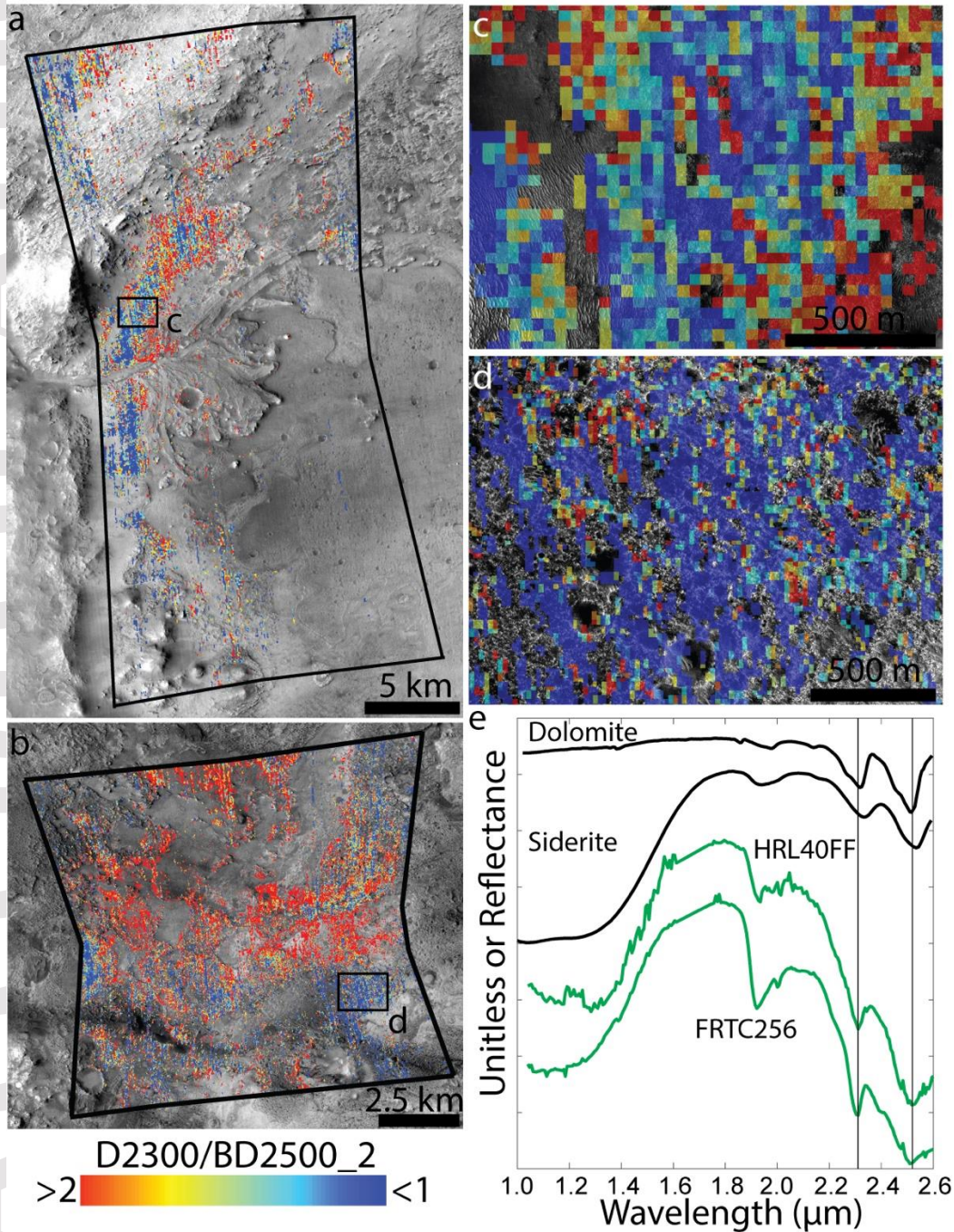


Figure 13 | Comparison of carbonate spectral properties in Jezero crater and elsewhere in the Nili Fossae region. (a) Ratio of the 2.3 and 2.5 μm absorptions (D_{2300}/BD_{2500_2}) in CRISM pixels of image HRL000040FF with $BD_{2500_2} \geq 0.005$. As noted by Horgan et al., (2020a), the most widespread collection of pixels with the lowest 2.3/2.5 μm absorption band depth ratio is associated with the margin fractured unit. However, the 2.3/2.5 μm band depth ratio is also low in the ROB unit immediately outside of Jezero crater. The black outline shows the extent of CRISM image HRL000040FF. (b) Ratio of the 2.3 and 2.5 μm absorptions (D_{2300}/BD_{2500_2}) in CRISM pixels of image FRT0000C256 with $BD_{2500_2} \geq 0.005$. There are large outcrops of carbonate with similar 2.3/2.5 μm band depth ratios as the margin fractured unit. All pixels shown here are associated with the ROB unit. Figure S14 shows an expanded view of 2.3/2.5 μm band depth ratios in this region, mosaicing multiple CRISM images. (c) Enlarged view of box shown in (a). (d) Enlarged view of box shown in (b). (e) Spectral endmembers of pixels shown in (a) and (b) calculated via HySime (green, Section 3.1) compared to library spectra of carbonates (black). Both endmembers are consistent with a mixture of carbonate, phyllosilicate(s), and olivine.

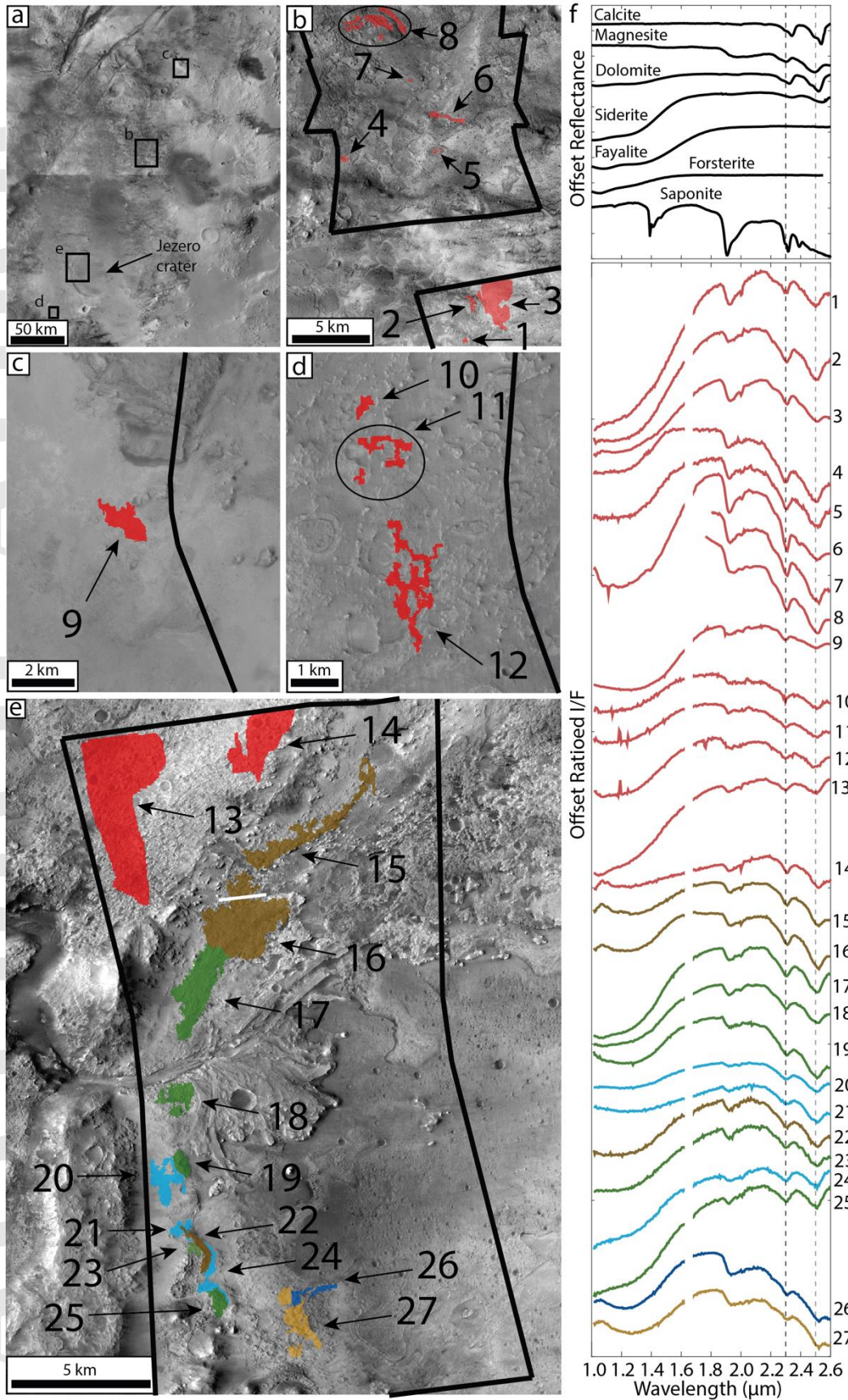


Figure 14 | VNIR carbonate spectra from within and outside of Jezero crater. (a) Overview of investigated area in the Nili Fossae region. (b) Enlarged view of box from (a) showing CRISM pixels (red) associated with the corresponding numbered carbonate spectra in (f) extracted from outside of Jezero crater. The combined coverage of the analyzed CRISM images in this area (FRT0000C256, FRT000095FE, and FRT000028BA) is outlined in black. (c) Same as (b), but for CRISM image FRT0000C968. (d) Same as (d), but for CRISM image FRT00016A73. (e) Same as (b), but for carbonate spectra extracted both from outside (13-14) and inside (15-27) Jezero crater from CRISM image HRL000040FF. (f) The CRISM spectra extracted from each labeled pixel cluster in (b-e) compared to mineral spectra measured in the laboratory. These spectra show evidence for carbonate, Fe/Mg-phyllsilicate, olivine, and either hydrated silica or Al-phyllsilicate. The carbonate spectra extracted from within and outside of Jezero crater are also qualitatively similar.

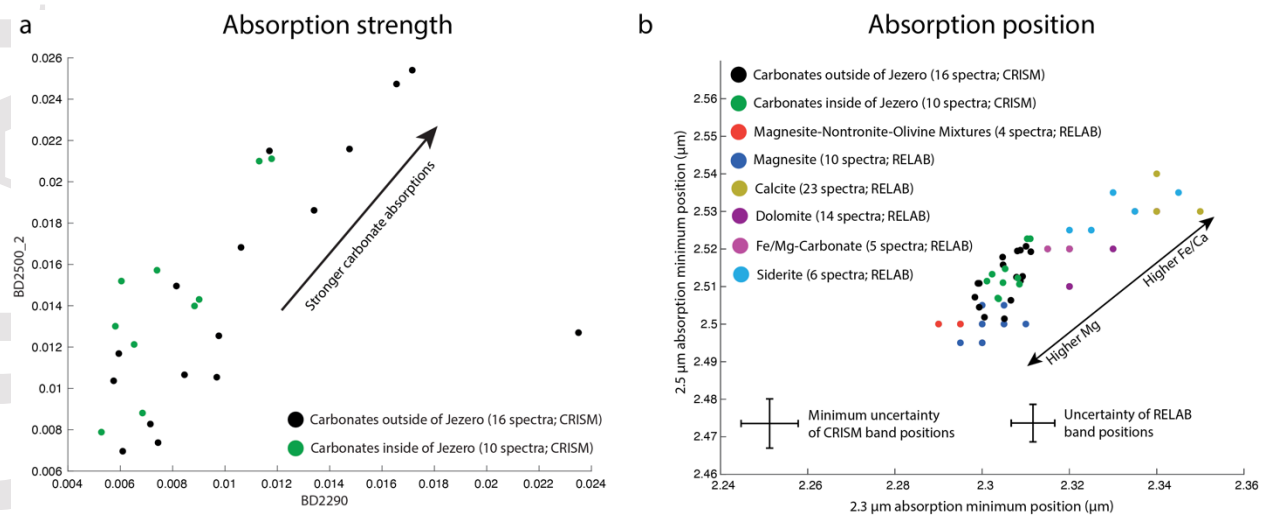


Figure 15 | Quantification of absorption band depths and minimum wavelength positions from within and outside of Jezero crater. (a) Measured CRISM band parameters BD2290 and BD2500_2 (Viviano-Beck et al., 2014) for the spectra displayed in Figure 14f. Carbonate band depths in Jezero crater are within the range of carbonate band depths extracted from outside of Jezero crater. (b) Measured absorption minima wavelength positions for the spectra displayed in Figure 14f compared to those of Ca-carbonate, Mg-carbonate, Fe-carbonate, (Fe,Mg)-carbonate, (Ca,Mg)-carbonate, and magnesite-nontronite-olivine mixtures measured in RELAB. The labeled uncertainties correspond to the spectra sampling of each spectrometer (6.55 nm for CRISM, 5 nm for these RELAB spectra). Estimated chemistries for carbonates within and outside of Jezero crater range from Mg-rich carbonate to (Fe,Mg)-rich carbonates based on these results.

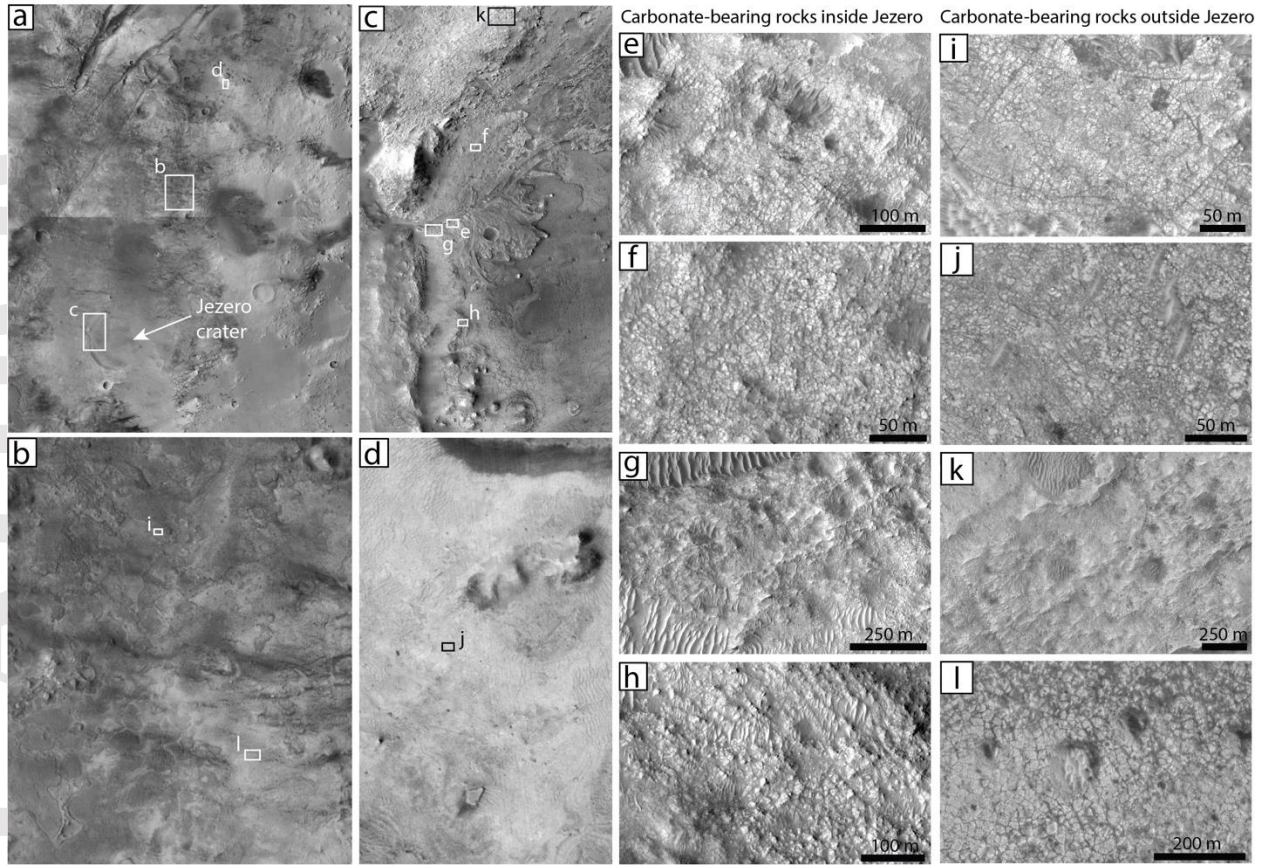


Figure 16 | Morphologies of carbonate-bearing rocks inside and outside of Jezero crater. (a) Overview of Jezero crater and surrounding Nili Fossae region. (c-d) Enlarged views of boxes shown in (a), which correspond to the locations of extracted carbonate spectra in Figure 14. (e-h) Enlarged views of boxes shown in (c) of carbonate-bearing rocks inside of Jezero crater. (i-l) Enlarged views of boxes shown in (c-d) of carbonate-bearing rocks outside of Jezero crater. The morphologies of carbonate-bearing rocks within and outside of Jezero crater are distinctly similar.

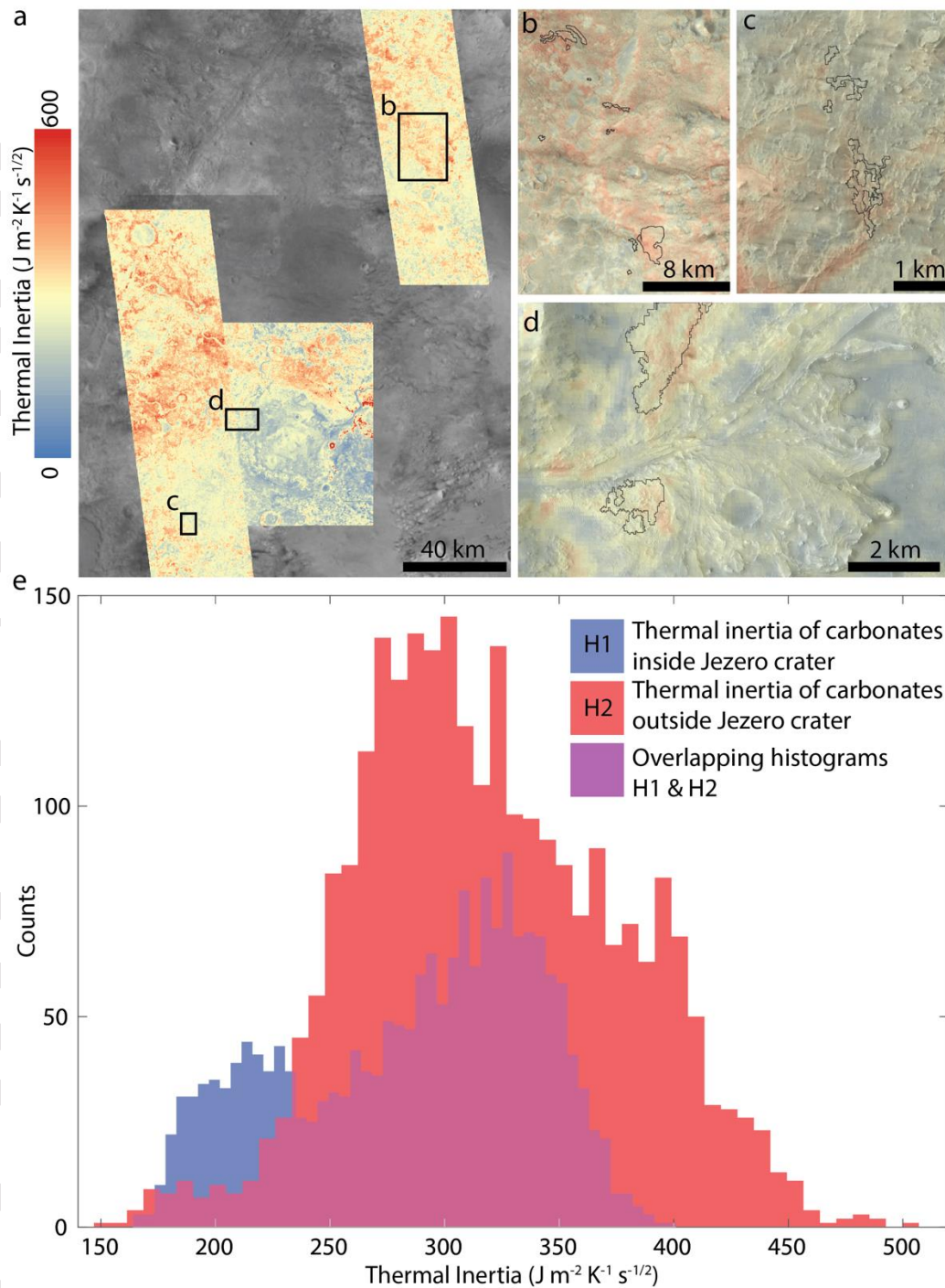


Figure 17 | Thermal inertia values for carbonates within and outside of Jezero crater. (a) Overview map of investigated area with THEMIS thermal inertia maps overlain. The scale bar for thermal inertia colors is the same for parts (a-d). The thermal inertia map covering Jezero crater is from (Edwards and Buz, 2021). (b) Enlarged view of the box labeled in (a), with the outlines of CRISM pixel clusters from Figure 14 shown in black over the thermal inertia map. These CRISM pixel clusters are from FRT0000C256, FRT000095FE, and FRT000028BA. (c) Same as (b), but for CRISM image FRT00016A73. (d) Same as (b), but for CRISM image HRL000040FF

inside of Jezero crater. (e) Histogram of thermal inertia values for all CRISM pixel clusters inside (H1, blue) and outside (H2, red) of Jezero crater shown in Figure 14. The histogram color is purple where the H1 (blue) and H2 (red) histograms overlap. Each histogram has 50 bins. The carbonates in Jezero crater have thermal inertia values within the range of carbonates outside of Jezero crater, but with more low thermal inertia values that are likely associated with dunes and unconsolidated material shown in Figures 4, 10, S6-S7.

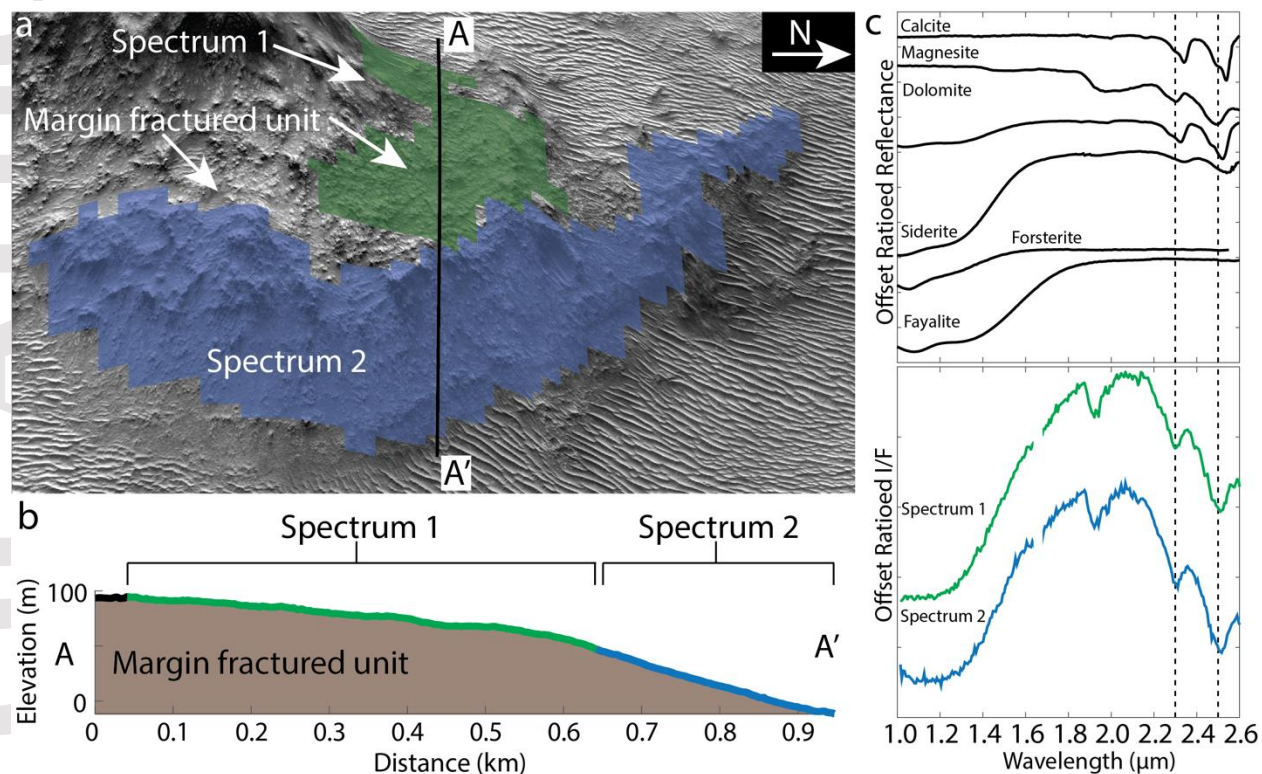


Figure 18 | Cross section of carbonate-bearing rocks inside Jezero crater. (a) HiRISE DTM (Ferguson et al., 2020) of carbonate-bearing rocks in Jezero crater in the margin fractured unit. The green and blue colors are CRISM pixel clusters from which the spectra in (c) were extracted. (b) Elevation profile of cross section shown in (a), with the areas covered by the CRISM pixel clusters labeled. (c) CRISM spectra of the pixel clusters shown in (a) compared to library spectra, showing that this entire outcrop cross section is carbonate-bearing.

References

Alfredsson, H.A., Oelkers, E.H., Hardarsson, B.S., Franzson, H., Gunnlaugsson, E., Gislason, S.R., 2013. The geology and water chemistry of the Hellisheidi, SW-Iceland carbon storage site. *International Journal of Greenhouse Gas Control* 12, 399–418. <https://doi.org/10.1016/j.ijggc.2012.11.019>

- Amador, E.S., Bandfield, J.L., Brazelton, W.J., Kelley, D., 2017. The Lost City Hydrothermal Field: A Spectroscopic and Astrobiological Analogue for Nili Fossae, Mars. *Astrobiology* 17, 1138–1160. <https://doi.org/10.1089/ast.2016.1606>
- Arvidson, R.E., Bell, J.F., Catalano, J.G., Clark, B.C., Fox, V.K., Gellert, R., Grotzinger, J.P., Guinness, E.A., Herkenhoff, K.E., Knoll, A.H., Lapotre, M.G.A., McLennan, S.M., Ming, D.W., Morris, R.V., Murchie, S.L., Powell, K.E., Smith, M.D., Squyres, S.W., Wolff, M.J., Wray, J.J., 2015. Mars Reconnaissance Orbiter and Opportunity observations of the Burns formation: Crater hopping at Meridiani Planum. *Journal of Geophysical Research: Planets* 120, 429–451. <https://doi.org/10.1002/2014JE004686>
- Arvidson, R.E., Christian, J.C., 2020. Use of CRISM, CTX, and HiRISE Data to Map Bedrock Sources and Wind-Blown Ripple Field Mineralogy On and Near the Jezero Crater Delta 51, 1194.
- Bandfield, J.L., Christensen, P.R., Smith, M.D., 2000. Spectral data set factor analysis and end-member recovery: Application to analysis of Martian atmospheric particulates. *Journal of Geophysical Research: Planets* 105, 9573–9587. <https://doi.org/10.1029/1999JE001094>
- Bandfield, J.L., Edgett, K.S., Christensen, P.R., 2002. Spectroscopic study of the Moses Lake dune field, Washington: Determination of compositional distributions and source lithologies. *Journal of Geophysical Research: Planets* 107, 2-1-2–15. <https://doi.org/10.1029/2000JE001469>
- Bandfield, J.L., Glotch, T.D., Christensen, P.R., 2003. Spectroscopic Identification of Carbonate Minerals in the Martian Dust. *Science* 301, 1084–1087. <https://doi.org/10.1126/science.1088054>
- Beinlich, A., Plümper, O., Boter, E., Müller, I.A., Kourim, F., Ziegler, M., Harigane, Y., Lafay, R., Kelemen, P.B., 2020. Ultramafic Rock Carbonation: Constraints From Listvenite Core BT1B, Oman Drilling Project. *Journal of Geophysical Research: Solid Earth* 125, e2019JB019060. <https://doi.org/10.1029/2019JB019060>
- Beyer, R.A., Alexandrov, O., McMichael, S., 2018. The Ames Stereo Pipeline: NASA’s Open Source Software for Deriving and Processing Terrain Data. *Earth and Space Science* 5, 537–548. <https://doi.org/10.1029/2018EA000409>
- Bibring, J.-P., Soufflot, A., Berthé, M., Langevin, Y., Gondet, B., Drossart, P., Bouyé, M., Combes, M., Puget, P., Semery, A., 2004. OMEGA: Observatoire pour la Minéralogie, l’Eau, les Glaces et l’Activité, in: *Mars Express: The Scientific Payload*. pp. 37–49.
- Bioucas-Dias, J.M., Nascimento, J.M.P., 2008. Hyperspectral Subspace Identification. *IEEE Transactions on Geoscience and Remote Sensing* 46, 2435–2445. <https://doi.org/10.1109/TGRS.2008.918089>
- Bishop, J.L., Perry, K.A., Dyar, M.D., Bristow, T.F., Blake, D.F., Brown, A.J., Peel, S.E., 2013a. Coordinated spectral and XRD analyses of magnesite-nontronite-forsterite mixtures and implications for carbonates on Mars. *Journal of Geophysical Research: Planets* 118, 635–650. <https://doi.org/10.1002/jgre.20066>
- Bishop, J.L., Tirsch, D., Tornabene, L.L., Jaumann, R., McEwen, A.S., McGuire, P.C., Ody, A., Poulet, F., Clark, R.N., Parente, M., McKeown, N.K., Mustard, J.F., Murchie, S.L., Voigt, J., Aydin, Z., Bamberg, M., Petau, A., Michael, G., Seelos, F.P., Hash, C.D., Swayze, G.A., Neukum, G., 2013b. Mineralogy and morphology of geologic units at Libya Montes, Mars: Ancient aqueously derived outcrops, mafic flows, fluvial features, and impacts. *Journal of Geophysical Research: Planets* 118, 487–513. <https://doi.org/10.1029/2012JE004151>
- Borg, L.E., Connelly, J.N., Nyquist, L.E., Shih, C.-Y., Wiesmann, H., Reese, Y., 1999. The Age of the Carbonates in Martian Meteorite ALH84001. *Science* 286, 90–94. <https://doi.org/10.1126/science.286.5437.90>
- Bosak, T., Moore, K.R., Gong, J., Grotzinger, J.P., 2021. Searching for biosignatures in sedimentary rocks from early Earth and Mars. *Nat Rev Earth Environ* 1–17. <https://doi.org/10.1038/s43017-021-00169-5>

- Boynton, W.V., Ming, D.W., Kounaves, S.P., Young, S.M.M., Arvidson, R.E., Hecht, M.H., Hoffman, J., Niles, P.B., Hamara, D.K., Quinn, R.C., Smith, P.H., Sutter, B., Catling, D.C., Morris, R.V., 2009. Evidence for Calcium Carbonate at the Mars Phoenix Landing Site. *Science* 325, 61–64. <https://doi.org/10.1126/science.1172768>
- Bramble, M.S., Mustard, J.F., Salvatore, M.R., 2017. The geological history of Northeast Syrtis Major, Mars. *Icarus* 293, 66–93. <https://doi.org/10.1016/j.icarus.2017.03.030>
- Bridges, J.C., Grady, M.M., 2000. Evaporite mineral assemblages in the nakhlite (martian) meteorites. *Earth and Planetary Science Letters* 176, 267–279. [https://doi.org/10.1016/S0012-821X\(00\)00019-4](https://doi.org/10.1016/S0012-821X(00)00019-4)
- Bristow, T.F., Milliken, R.E., 2011. TERRESTRIAL PERSPECTIVE ON AUTHIGENIC CLAY MINERAL PRODUCTION IN ANCIENT MARTIAN LAKES. *Clays and Clay Minerals* 59, 339–358. <https://doi.org/10.1346/CCMN.2011.0590401>
- Brown, A.J., Hook, S.J., Baldridge, A.M., Crowley, J.K., Bridges, N.T., Thomson, B.J., Marion, G.M., de Souza Filho, C.R., Bishop, J.L., 2010. Hydrothermal formation of Clay-Carbonate alteration assemblages in the Nili Fossae region of Mars. *Earth and Planetary Science Letters* 297, 174–182. <https://doi.org/10.1016/j.epsl.2010.06.018>
- Brown, A.J., Viviano, C.E., Goudge, T.A., 2020. Olivine-Carbonate Mineralogy of the Jezero Crater Region. *Journal of Geophysical Research: Planets* 125, e2019JE006011. <https://doi.org/10.1029/2019JE006011>
- Bultel, B., Viennet, J.-C., Poulet, F., Carter, J., Werner, S.C., 2019. Detection of Carbonates in Martian Weathering Profiles. *Journal of Geophysical Research: Planets* 124, 989–1007. <https://doi.org/10.1029/2018JE005845>
- Cannon, K.M., Mustard, J.F., Parman, S.W., Sklute, E.C., Dyar, M.D., Cooper, R.F., 2017. Spectral properties of Martian and other planetary glasses and their detection in remotely sensed data. *Journal of Geophysical Research: Planets* 122, 249–268. <https://doi.org/10.1002/2016JE005219>
- Carrozzo, F.G., Di Achille, G., Salese, F., Altieri, F., Bellucci, G., 2017. Geology and mineralogy of the Auki Crater, Tyrrhena Terra, Mars: A possible post impact-induced hydrothermal system. *Icarus* 281, 228–239. <https://doi.org/10.1016/j.icarus.2016.09.001>
- Carter, J., Poulet, F., 2012. Orbital identification of clays and carbonates in Gusev crater. *Icarus* 219, 250–253. <https://doi.org/10.1016/j.icarus.2012.02.024>
- Carter, J., Viviano-Beck, C., Loizeau, D., Bishop, J., Le Deit, L., 2015. Orbital detection and implications of akaganéite on Mars. *Icarus* 253, 296–310. <https://doi.org/10.1016/j.icarus.2015.01.020>
- Catling, D.C., 1999. A chemical model for evaporites on early Mars: Possible sedimentary tracers of the early climate and implications for exploration. *Journal of Geophysical Research: Planets* 104, 16453–16469. <https://doi.org/10.1029/1998JE001020>
- Christensen, P.R., Bandfield, J.L., Hamilton, V.E., Ruff, S.W., Kieffer, H.H., Titus, T.N., Malin, M.C., Morris, R.V., Lane, M.D., Clark, R.L., Jakosky, B.M., Mellon, M.T., Pearl, J.C., Conrath, B.J., Smith, M.D., Clancy, R.T., Kuzmin, R.O., Roush, T., Mehall, G.L., Gorelick, N., Bender, K., Murray, K., Dason, S., Greene, E., Silverman, S., Greenfield, M., 2001. Mars Global Surveyor Thermal Emission Spectrometer experiment: Investigation description and surface science results. *Journal of Geophysical Research: Planets* 106, 23823–23871. <https://doi.org/10.1029/2000JE001370>
- Christensen, P.R., Jakosky, B.M., Kieffer, H.H., Malin, M.C., McSween, H.Y., Nealson, K., Mehall, G.L., Silverman, S.H., Ferry, S., Caplinger, M., Ravine, M., 2004. The Thermal Emission Imaging System (THEMIS) for the Mars 2001 Odyssey Mission. *Space Science Reviews* 110, 85–130. <https://doi.org/10.1023/B:SPAC.0000021008.16305.94>
- Clark, R.N., King, T.V.V., Gorelick, N., 1987. Automatic continuum analysis of reflectance spectra. Presented at the JPL Proceedings of the 3rd Airborne Imaging Spectrometer Data Analysis Workshop.

- Clenet, H., Pinet, P., Ceuleneer, G., Daydou, Y., Heuripeau, F., Rosemberg, C., Bibring, J.-P., Bellucci, G., Altieri, F., Gondet, B., 2013. A systematic mapping procedure based on the Modified Gaussian Model to characterize magmatic units from olivine/pyroxenes mixtures: Application to the Syrtis Major volcanic shield on Mars. *Journal of Geophysical Research: Planets* 118, 1632–1655. <https://doi.org/10.1002/jgre.20112>
- Corrigan, C.M., Harvey, R.P., 2004. Multi-generational carbonate assemblages in martian meteorite Allan Hills 84001: Implications for nucleation, growth, and alteration. *Meteoritics & Planetary Science* 39, 17–30. <https://doi.org/10.1111/j.1945-5100.2004.tb00047.x>
- Costello, L.J., Filiberto, J., Crandall, J.R., Potter-McIntyre, S.L., Schwenzer, S.P., Miller, M.A., Hummer, D.R., Olsson-Francis, K., Perl, S., 2020. Habitability of hydrothermal systems at Jezero and Gusev Craters as constrained by hydrothermal alteration of a terrestrial mafic dike. *Geochemistry* 80, 125613. <https://doi.org/10.1016/j.chemer.2020.125613>
- Day, M., Dorn, T., 2019. Wind in Jezero Crater, Mars. *Geophysical Research Letters* 46, 3099–3107. <https://doi.org/10.1029/2019GL082218>
- de Obeso, J.C., Kelemen, P.B., 2018. Fluid rock interactions on residual mantle peridotites overlain by shallow oceanic limestones: Insights from Wadi Fins, Sultanate of Oman. *Chemical Geology* 498, 139–149. <https://doi.org/10.1016/j.chemgeo.2018.09.022>
- Dickson, J.L., Ehlmann, B.L., Kerber, L., Fassett, C.I., Hare, T.M., Quinn, D.P., Plesea, L., Noss, D., 2020. The Global CTX Mosaic of Mars: Lessons for the Construction and Dissemination of Massive Imaging Data Sets 51, 2309.
- Drake, H., Heim, C., Roberts, N.M.W., Zack, T., Tillberg, M., Broman, C., Ivarsson, M., Whitehouse, M.J., Åström, M.E., 2017. Isotopic evidence for microbial production and consumption of methane in the upper continental crust throughout the Phanerozoic eon. *Earth and Planetary Science Letters* 470, 108–118. <https://doi.org/10.1016/j.epsl.2017.04.034>
- Dundar, M., Ehlmann, B.L., Leask, E.K., 2019. Machine-Learning-Driven New Geologic Discoveries at Mars Rover Landing Sites: Jezero and NE Syrtis. arXiv:1909.02387 [astro-ph, stat].
- Dupraz, C., Reid, R.P., Braissant, O., Decho, A.W., Norman, R.S., Visscher, P.T., 2009. Processes of carbonate precipitation in modern microbial mats. *Earth-Science Reviews, Microbial Mats in Earth's Fossil Record of Life: Geobiology* 96, 141–162. <https://doi.org/10.1016/j.earscirev.2008.10.005>
- Dupraz, C., Visscher, P.T., Baumgartner, L.K., Reid, R.P., 2004. Microbe–mineral interactions: early carbonate precipitation in a hypersaline lake (Eleuthera Island, Bahamas). *Sedimentology* 51, 745–765. <https://doi.org/10.1111/j.1365-3091.2004.00649.x>
- Edwards, C.S., Buz, J., 2021. THEMIS-derived Thermal Inertia of Jezero Crater, Mars. <https://doi.org/10.5281/zenodo.4931348>
- Edwards, C.S., Ehlmann, B.L., 2015. Carbon sequestration on Mars. *Geology* 43, 863–866. <https://doi.org/10.1130/G36983.1>
- Edwards, C.S., Piqueux, S., Hamilton, V.E., Ferguson, R.L., Herkenhoff, K.E., Vasavada, A.R., Bennett, K.A., Sacks, L., Lewis, K., Smith, M.D., 2018. The Thermophysical Properties of the Bagnold Dunes, Mars: Ground-Truthing Orbital Data. *Journal of Geophysical Research: Planets* 123, 1307–1326. <https://doi.org/10.1029/2017JE005501>
- Ehlmann, B.L., Mustard, J.F., 2012. An in-situ record of major environmental transitions on early Mars at Northeast Syrtis Major. *Geophysical Research Letters* 39. <https://doi.org/10.1029/2012GL051594>
- Ehlmann, B.L., Mustard, J.F., Fassett, C.I., Schon, S.C., Head Iii, J.W., Des Marais, D.J., Grant, J.A., Murchie, S.L., 2008a. Clay minerals in delta deposits and organic preservation potential on Mars. *Nature Geoscience* 1, 355–358. <https://doi.org/10.1038/ngeo207>

- Ehlmann, B.L., Mustard, J.F., Murchie, S.L., Poulet, F., Bishop, J.L., Brown, A.J., Calvin, W.M., Clark, R.N., Marais, D.J.D., Milliken, R.E., Roach, L.H., Roush, T.L., Swayze, G.A., Wray, J.J., 2008b. Orbital Identification of Carbonate-Bearing Rocks on Mars. *Science* 322, 1828–1832. <https://doi.org/10.1126/science.1164759>
- Ehlmann, B.L., Mustard, J.F., Swayze, G.A., Clark, R.N., Bishop, J.L., Poulet, F., Marais, D.J.D., Roach, L.H., Milliken, R.E., Wray, J.J., Barnouin-Jha, O., Murchie, S.L., 2009. Identification of hydrated silicate minerals on Mars using MRO-CRISM: Geologic context near Nili Fossae and implications for aqueous alteration. *Journal of Geophysical Research: Planets* 114. <https://doi.org/10.1029/2009JE003339>
- El-Shenawy, M.I., Niles, P.B., Ming, D.W., Socki, R., Righter, K., 2020. Oxygen and carbon stable isotope composition of the weathering Mg-carbonates formed on the surface of the LEW 85320 ordinary chondrite: Revisited. *Meteoritics & Planetary Science* 55. <https://doi.org/10.1111/maps.13553>
- Fairén, A.G., Dohm, J.M., Baker, V.R., de Pablo, M.A., Ruiz, J., Ferris, J.C., Anderson, R.C., 2003. Episodic flood inundations of the northern plains of Mars. *Icarus* 165, 53–67. [https://doi.org/10.1016/S0019-1035\(03\)00144-1](https://doi.org/10.1016/S0019-1035(03)00144-1)
- Falk, E.S., Kelemen, P.B., 2015. Geochemistry and petrology of listvenite in the Samail ophiolite, Sultanate of Oman: Complete carbonation of peridotite during ophiolite emplacement. *Geochimica et Cosmochimica Acta* 160, 70–90. <https://doi.org/10.1016/j.gca.2015.03.014>
- Fassett, C.I., Head, J.W., 2005. Fluvial sedimentary deposits on Mars: Ancient deltas in a crater lake in the Nili Fossae region. *Geophysical Research Letters* 32. <https://doi.org/10.1029/2005GL023456>
- Ferguson, R.L., Christensen, P.R., Kieffer, H.H., 2006. High-resolution thermal inertia derived from the Thermal Emission Imaging System (THEMIS): Thermal model and applications. *Journal of Geophysical Research: Planets* 111. <https://doi.org/10.1029/2006JE002735>
- Ferguson, R.L., Hare, T.M., Mayer, D.P., Galuszka, D.M., Redding, B.L., Smith, E.D., Shinaman, J.R., Cheng, Y., Otero, R.E., 2020. Mars 2020 Terrain Relative Navigation Flight Product Generation: Digital Terrain Model and Orthorectified Image Mosaic 51, 2020.
- Fischer, P.D., Brown, M.E., Hand, K.P., 2015. SPATIALLY RESOLVED SPECTROSCOPY OF EUROPA: THE DISTINCT SPECTRUM OF LARGE-SCALE CHAOS. *AJ* 150, 164. <https://doi.org/10.1088/0004-6256/150/5/164>
- Fraeman, A.A., Ehlmann, B.L., Arvidson, R.E., Edwards, C.S., Grotzinger, J.P., Milliken, R.E., Quinn, D.P., Rice, M.S., 2016. The stratigraphy and evolution of lower Mount Sharp from spectral, morphological, and thermophysical orbital data sets. *Journal of Geophysical Research: Planets* 121, 1713–1736. <https://doi.org/10.1002/2016JE005095>
- Gaffey, S.J., 1987. Spectral reflectance of carbonate minerals in the visible and near infrared (0.35–2.55 μm): Anhydrous carbonate minerals. *Journal of Geophysical Research: Solid Earth* 92, 1429–1440. <https://doi.org/10.1029/JB092iB02p01429>
- Given, R.K., Wilkinson, B.H., 1985. Kinetic control of morphology, composition, and mineralogy of abiotic sedimentary carbonates. *Journal of Sedimentary Research* 55, 109–119. <https://doi.org/10.1306/212F862A-2B24-11D7-8648000102C1865D>
- Glotch, T.D., Bandfield, J.L., 2006. Determination and interpretation of surface and atmospheric Miniature Thermal Emission Spectrometer spectral end-members at the Meridiani Planum landing site. *Journal of Geophysical Research: Planets* 111. <https://doi.org/10.1029/2005JE002671>
- Glotch, T.D., Rogers, A.D., 2013. Evidence for magma-carbonate interaction beneath Syrtis Major, Mars. *Journal of Geophysical Research: Planets* 118, 126–137. <https://doi.org/10.1029/2012JE004230>
- Gooding, J.L., Wentworth, S.J., Zolensky, M.E., 1991. Aqueous alteration of the Nakhla meteorite. *Meteoritics* 26, 135–143. <https://doi.org/10.1111/j.1945-5100.1991.tb01029.x>

- Goudge, T.A., Milliken, R.E., Head, J.W., Mustard, J.F., Fassett, C.I., 2017. Sedimentological evidence for a deltaic origin of the western fan deposit in Jezero crater, Mars and implications for future exploration. *Earth and Planetary Science Letters* 458, 357–365. <https://doi.org/10.1016/j.epsl.2016.10.056>
- Goudge, T.A., Mohrig, D., Cardenas, B.T., Hughes, C.M., Fassett, C.I., 2018. Stratigraphy and paleohydrology of delta channel deposits, Jezero crater, Mars. *Icarus* 301, 58–75. <https://doi.org/10.1016/j.icarus.2017.09.034>
- Goudge, T.A., Mustard, J.F., Head, J.W., Fassett, C.I., Wiseman, S.M., 2015. Assessing the mineralogy of the watershed and fan deposits of the Jezero crater paleolake system, Mars. *Journal of Geophysical Research: Planets* 120, 775–808. <https://doi.org/10.1002/2014JE004782>
- Greeley, R., Foing, B.H., McSween, H.Y., Neukum, G., Pinet, P., Kan, M. van, Werner, S.C., Williams, D.A., Zegers, T.E., 2005. Fluid lava flows in Gusev crater, Mars. *Journal of Geophysical Research: Planets* 110. <https://doi.org/10.1029/2005JE002401>
- Greely, R., Guest, J., 1987. Geologic map of the eastern equatorial region of Mars.
- Halevy, I., Fischer, W.W., Eiler, J.M., 2011. Carbonates in the Martian meteorite Allan Hills 84001 formed at 18 ± 4 °C in a near-surface aqueous environment. *PNAS* 108, 16895–16899. <https://doi.org/10.1073/pnas.1109444108>
- Hays, L.E., Graham, H.V., Des Marais, D.J., Hausrath, E.M., Horgan, B., McCollom, T.M., Parenteau, M.N., Potter-McIntyre, S.L., Williams, A.J., Lynch, K.L., 2017. Biosignature Preservation and Detection in Mars Analog Environments. *Astrobiology* 17, 363–400. <https://doi.org/10.1089/ast.2016.1627>
- Hoefen, T.M., Clark, R.N., Bandfield, J.L., Smith, M.D., Pearl, J.C., Christensen, P.R., 2003. Discovery of Olivine in the Nili Fossae Region of Mars. *Science* 302, 627–630. <https://doi.org/10.1126/science.1089647>
- Horgan, B.H.N., Anderson, R.B., Dromart, G., Amador, E.S., Rice, M.S., 2020a. The mineral diversity of Jezero crater: Evidence for possible lacustrine carbonates on Mars. *Icarus* 339, 113526. <https://doi.org/10.1016/j.icarus.2019.113526>
- Horgan, B.H.N., Johnson, J.R., Fraeman, A.A., Rice, M.S., Seeger, C., Bell, J.F., Bennett, K.A., Cloutis, E.A., Edgar, L.A., Frydenvang, J., Grotzinger, J.P., L’Haridon, J., Jacob, S.R., Mangold, N., Rampe, E.B., Rivera-Hernandez, F., Sun, V.Z., Thompson, L.M., Wellington, D., 2020b. Diagenesis of Vera Rubin Ridge, Gale Crater, Mars, From Mastcam Multispectral Images. *Journal of Geophysical Research: Planets* 125, e2019JE006322. <https://doi.org/10.1029/2019JE006322>
- Hundal, C.B., Mustard, J.F., Kremer, C.H., 2020. Origin of the Pitted Capping Unit in Nili Fossae, Mars 51, 1629.
- Itoh, Y., Parente, M., 2021. A new method for atmospheric correction and de-noising of CRISM hyperspectral data. *Icarus* 354, 114024. <https://doi.org/10.1016/j.icarus.2020.114024>
- Ivarsson, M., Bach, W., Broman, C., Neubeck, A., Bengtson, S., 2018. Fossilized Life in Subseafloor Ultramafic Rocks. *Geomicrobiology Journal* 35, 460–467. <https://doi.org/10.1080/01490451.2017.1370517>
- Ivarsson, M., Bengtson, S., Belivanova, V., Stampanoni, M., Marone, F., Tehler, A., 2012. Fossilized fungi in subseafloor Eocene basalts. *Geology* 40, 163–166. <https://doi.org/10.1130/G32590.1>
- Jain, N., Chauhan, P., 2015. Study of phyllosilicates and carbonates from the Capri Chasma region of Valles Marineris on Mars based on Mars Reconnaissance Orbiter-Compact Reconnaissance Imaging Spectrometer for Mars (MRO-CRISM) observations. *Icarus* 250, 7–17. <https://doi.org/10.1016/j.icarus.2014.11.018>
- Jones, J.B., Segnit, E.R., 1971. The nature of opal I. nomenclature and constituent phases. *Journal of the Geological Society of Australia* 18, 57–68. <https://doi.org/10.1080/00167617108728743>

- Jull, A.J.T., Cheng, S., Gooding, J.L., Velbel, M.A., 1988. Rapid Growth of Magnesium-Carbonate Weathering Products in a Stony Meteorite from Antarctica. *Science* 242, 417–419. <https://doi.org/10.1126/science.242.4877.417>
- Kah, L.C., Lyons, T.W., Chesley, J.T., 2001. Geochemistry of a 1.2 Ga carbonate-evaporite succession, northern Baffin and Bylot Islands: implications for Mesoproterozoic marine evolution. *Precambrian Research* 111, 203–234. [https://doi.org/10.1016/S0301-9268\(01\)00161-9](https://doi.org/10.1016/S0301-9268(01)00161-9)
- Kastner, M., Keene, J.B., Gieskes, J.M., 1977. Diagenesis of siliceous oozes—I. Chemical controls on the rate of opal-A to opal-CT transformation—an experimental study. *Geochimica et Cosmochimica Acta* 41, 1041–1059. [https://doi.org/10.1016/0016-7037\(77\)90099-0](https://doi.org/10.1016/0016-7037(77)90099-0)
- Kelemen, P.B., Evans, O., Ghiorso, M., Mustard, J., Ehlmann, B.L., Spiegelman, M., 2020. Carbonate in Olivine-Rich Unit(s) on Mars May Have Formed at Low P(H₂O) 51, 1213.
- Kelemen, P.B., Matter, J., Streit, E.E., Rudge, J.F., Curry, W.B., Blusztajn, J., 2011. Rates and Mechanisms of Mineral Carbonation in Peridotite: Natural Processes and Recipes for Enhanced, in situ CO₂ Capture and Storage. *Annual Review of Earth and Planetary Sciences* 39, 545–576. <https://doi.org/10.1146/annurev-earth-092010-152509>
- Kieffer, H.H., 2013. Thermal model for analysis of Mars infrared mapping. *Journal of Geophysical Research: Planets* 118, 451–470. <https://doi.org/10.1029/2012JE004164>
- Klein, F., Bach, W., Humphris, S.E., Kahl, W.-A., Jöns, N., Moskowitz, B., Berquó, T.S., 2014. Magnetite in seafloor serpentinite—Some like it hot. *Geology* 42, 135–138. <https://doi.org/10.1130/G35068.1>
- Klein, F., Humphris, S.E., Guo, W., Schubotz, F., Schwarzenbach, E.M., Orsi, W.D., 2015. Fluid mixing and the deep biosphere of a fossil Lost City-type hydrothermal system at the Iberia Margin. *PNAS* 112, 12036–12041. <https://doi.org/10.1073/pnas.1504674112>
- Knauth, L.P., Brilli, M., Klonowski, S., 2003. Isotope geochemistry of caliche developed on basalt. *Geochimica et Cosmochimica Acta* 67, 185–195. [https://doi.org/10.1016/S0016-7037\(02\)01051-7](https://doi.org/10.1016/S0016-7037(02)01051-7)
- Koeppen, W.C., Hamilton, V.E., 2008. Global distribution, composition, and abundance of olivine on the surface of Mars from thermal infrared data. *Journal of Geophysical Research: Planets* 113. <https://doi.org/10.1029/2007JE002984>
- Kremer, C.H., Mustard, J.F., Bramble, M.S., 2019. A widespread olivine-rich ash deposit on Mars. *Geology* 47, 677–681. <https://doi.org/10.1130/G45563.1>
- Lane, M.D., Dyar, M.D., Bishop, J.L., 2004. Spectroscopic evidence for hydrous iron sulfate in the Martian soil. *Geophysical Research Letters* 31. <https://doi.org/10.1029/2004GL021231>
- Laskar, J., Correia, A.C.M., Gastineau, M., Joutel, F., Levrard, B., Robutel, P., 2004. Long term evolution and chaotic diffusion of the insolation quantities of Mars. *Icarus* 170, 343–364. <https://doi.org/10.1016/j.icarus.2004.04.005>
- Lin, H., Tarnas, J.D., Mustard, J.F., Zhang, X., Wei, Y., Wan, W., Klein, F., Kellner, J.R., 2021. Dynamic aperture factor analysis/target transformation (DAFA/TT) for Mg-serpentine and Mg-carbonate mapping on Mars with CRISM near-infrared data. *Icarus* 355, 114168. <https://doi.org/10.1016/j.icarus.2020.114168>
- Lin, H., Tarnas, J.D., Mustard, J.F., Zhang, X., Wei, Y., Wan, W., Klein, F., Kellner, J.R., 2020. Dynamic aperture factor analysis/target transformation (DAFA/TT) for Mg-serpentine and Mg-carbonate mapping on Mars with CRISM near-infrared data. *Icarus* 114168. <https://doi.org/10.1016/j.icarus.2020.114168>
- Malin, M.C., Bell, J.F., Cantor, B.A., Caplinger, M.A., Calvin, W.M., Clancy, R.T., Edgett, K.S., Edwards, L., Haberle, R.M., James, P.B., Lee, S.W., Ravine, M.A., Thomas, P.C., Wolff, M.J., 2007. Context Camera Investigation on board the Mars Reconnaissance Orbiter. *Journal of Geophysical Research: Planets* 112. <https://doi.org/10.1029/2006JE002808>

- Mandon, L., Quantin-Nataf, C., Thollot, P., Mangold, N., Lozac'h, L., Dromart, G., Beck, P., Dehouck, E., Breton, S., Millot, C., Volat, M., 2020. Refining the age, emplacement and alteration scenarios of the olivine-rich unit in the Nili Fossae region, Mars. *Icarus* 336, 113436. <https://doi.org/10.1016/j.icarus.2019.113436>
- Matherne, C., Skok, J.R., Mustard, J.F., Karunatillake, S., Doran, P., 2020. Multistage ice-damming of volcanic flows and fluvial systems in Northeast Syrtis Major. *Icarus* 340, 113608. <https://doi.org/10.1016/j.icarus.2019.113608>
- Matter, J.M., Kelemen, P.B., 2009. Permanent storage of carbon dioxide in geological reservoirs by mineral carbonation. *Nature Geoscience* 2, 837–841. <https://doi.org/10.1038/ngeo683>
- McCoy, T.J., Sims, M., Schmidt, M.E., Edwards, L., Tornabene, L.L., Crumpler, L.S., Cohen, B.A., Soderblom, L.A., Blaney, D.L., Squyres, S.W., Arvidson, R.E., Rice, J.W., Tréguier, E., d'Uston, C., Grant, J.A., McSween, H.Y., Golombek, M.P., Haldemann, A.F.C., Souza, P.A. de, 2008. Structure, stratigraphy, and origin of Husband Hill, Columbia Hills, Gusev Crater, Mars. *Journal of Geophysical Research: Planets* 113. <https://doi.org/10.1029/2007JE003041>
- McEwen, A.S., Eliason, E.M., Bergstrom, J.W., Bridges, N.T., Hansen, C.J., Delamere, W.A., Grant, J.A., Gulick, V.C., Herkenhoff, K.E., Keszthelyi, L., Kirk, R.L., Mellon, M.T., Squyres, S.W., Thomas, N., Weitz, C.M., 2007. Mars Reconnaissance Orbiter's High Resolution Imaging Science Experiment (HiRISE). *Journal of Geophysical Research: Planets* 112. <https://doi.org/10.1029/2005JE002605>
- McKinley, F.W., T.O. Stevens, 2000. Microfossils and Paleoenvironments in Deep Subsurface Basalt Samples. *Geomicrobiology Journal* 17, 43–54. <https://doi.org/10.1080/014904500270486>
- McMahon, S., Bosak, T., Grotzinger, J.P., Milliken, R.E., Summons, R.E., Daye, M., Newman, S.A., Fraeman, A., Williford, K.H., Briggs, D.E.G., 2018. A Field Guide to Finding Fossils on Mars. *Journal of Geophysical Research: Planets* 123, 1012–1040. <https://doi.org/10.1029/2017JE005478>
- McSween, H.Y., 1994. What we have learned about Mars from SNC meteorites. *Meteoritics* 29, 757–779. <https://doi.org/10.1111/j.1945-5100.1994.tb01092.x>
- McSween, H.Y., Harvey, R.P., 1998. An Evaporation Model for Formation of Carbonates in the ALH84001 Martian Meteorite. *International Geology Review* 40, 774–783. <https://doi.org/10.1080/00206819809465238>
- McSween, H.Y., Ruff, S.W., Morris, R.V., Gellert, R., Klingelhöfer, G., Christensen, P.R., McCoy, T.J., Ghosh, A., Moersch, J.M., Cohen, B.A., Rogers, A.D., Schröder, C., Squyres, S.W., Crisp, J., Yen, A., 2008. Mineralogy of volcanic rocks in Gusev Crater, Mars: Reconciling Mössbauer, Alpha Particle X-Ray Spectrometer, and Miniature Thermal Emission Spectrometer spectra. *Journal of Geophysical Research: Planets* 113. <https://doi.org/10.1029/2007JE002970>
- Michalski, J.R., Cuadros, J., Niles, P.B., Parnell, J., Deanne Rogers, A., Wright, S.P., 2013. Groundwater activity on Mars and implications for a deep biosphere. *Nature Geoscience* 6, 133–138. <https://doi.org/10.1038/ngeo1706>
- Michalski, J.R., Dobrea, E.Z.N., Niles, P.B., Cuadros, J., 2017. Ancient hydrothermal seafloor deposits in Eridania basin on Mars. *Nature Communications* 8, 15978. <https://doi.org/10.1038/ncomms15978>
- Michalski, J.R., Niles, P.B., 2010. Deep crustal carbonate rocks exposed by meteor impact on Mars. *Nature Geoscience* 3, 751–755. <https://doi.org/10.1038/ngeo971>
- Moody, J.B., 1976. Serpentinization: a review. *Lithos* 9, 125–138. [https://doi.org/10.1016/0024-4937\(76\)90030-X](https://doi.org/10.1016/0024-4937(76)90030-X)
- Morris, R.V., Blake, D.F., Bish, D., Ming, D.W., Agresti, D.G., Treiman, A.H., Steele, A., Amundsen, H.E.F., Amase Team, 2011. A Terrestrial Analogue from Spitsbergen (Svalbard, Norway) for the Comanche Carbonate at Gusev Crater, Mars 1699.

- Morris, R.V., Ruff, S.W., Gellert, R., Ming, D.W., Arvidson, R.E., Clark, B.C., Golden, D.C., Siebach, K., Klingelhöfer, G., Schröder, C., Fleischer, I., Yen, A.S., Squyres, S.W., 2010. Identification of Carbonate-Rich Outcrops on Mars by the Spirit Rover. *Science* 329, 421–424. <https://doi.org/10.1126/science.1189667>
- Murchie, S., Arvidson, R., Bedini, P., Beisser, K., Bibring, J.-P., Bishop, J., Boldt, J., Cavender, P., Choo, T., Clancy, R.T., Darlington, E.H., Marais, D.D., Espiritu, R., Fort, D., Green, R., Guinness, E., Hayes, J., Hash, C., Heffernan, K., Hemmler, J., Heyler, G., Humm, D., Hutcheson, J., Izenberg, N., Lee, R., Lees, J., Lohr, D., Malaret, E., Martin, T., McGovern, J.A., McGuire, P., Morris, R., Mustard, J., Pelkey, S., Rhodes, E., Robinson, M., Roush, T., Schaefer, E., Seagrave, G., Seelos, F., Silvergate, P., Slavney, S., Smith, M., Shyong, W.-J., Strohbahn, K., Taylor, H., Thompson, P., Tossman, B., Wirzburger, M., Wolff, M., 2007. Compact Reconnaissance Imaging Spectrometer for Mars (CRISM) on Mars Reconnaissance Orbiter (MRO). *Journal of Geophysical Research: Planets* 112. <https://doi.org/10.1029/2006JE002682>
- Mustard, J.F., Ehlmann, B.L., Murchie, S.L., Poulet, F., Mangold, N., Head, J.W., Bibring, J.-P., Roach, L.H., 2009. Composition, Morphology, and Stratigraphy of Noachian Crust around the Isidis basin. *Journal of Geophysical Research: Planets* 114. <https://doi.org/10.1029/2009JE003349>
- Mustard, J.F., Murchie, S.L., Pelkey, S.M., Ehlmann, B.L., Milliken, R.E., Grant, J.A., Bibring, J.-P., Poulet, F., Bishop, J., Dobreá, E.N., Roach, L., Seelos, F., Arvidson, R.E., Wiseman, S., Green, R., Hash, C., Humm, D., Malaret, E., McGovern, J.A., Seelos, K., Clancy, T., Clark, R., Marais, D.D., Izenberg, N., Knudson, A., Langevin, Y., Martin, T., McGuire, P., Morris, R., Robinson, M., Roush, T., Smith, M., Swayze, G., Taylor, H., Titus, T., Wolff, M., 2008. Hydrated silicate minerals on Mars observed by the Mars Reconnaissance Orbiter CRISM instrument. *Nature* 454, 305–309. <https://doi.org/10.1038/nature07097>
- Newman, S.A., Lincoln, S.A., O'Reilly, S., Liu, X., Shock, E.L., Kelemen, P.B., Summons, R.E., 2020. Lipid Biomarker Record of the Serpentinite-Hosted Ecosystem of the Samail Ophiolite, Oman and Implications for the Search for Biosignatures on Mars. *Astrobiology* 20, 830–845. <https://doi.org/10.1089/ast.2019.2066>
- Niles, P.B., Catling, D.C., Berger, G., Chassefière, E., Ehlmann, B.L., Michalski, J.R., Morris, R., Ruff, S.W., Sutter, B., 2013. Geochemistry of Carbonates on Mars: Implications for Climate History and Nature of Aqueous Environments. *Space Sci Rev* 174, 301–328. <https://doi.org/10.1007/s11214-012-9940-y>
- Oelkers, E.H., Gislason, S.R., Matter, J., 2008. Mineral Carbonation of CO₂. *Elements* 4, 333–337. <https://doi.org/10.2113/gselements.4.5.333>
- Onstott, T. c., Ehlmann, B. I., Sapers, H., Coleman, M., Ivarsson, M., Marlow, J. j., Neubeck, A., Niles, P., 2019. Paleo-Rock-Hosted Life on Earth and the Search on Mars: A Review and Strategy for Exploration. *Astrobiology* 19, 1230–1262. <https://doi.org/10.1089/ast.2018.1960>
- Palumbo, A.M., Head, J.W., 2018. Impact cratering as a cause of climate change, surface alteration, and resurfacing during the early history of Mars. *Meteoritics & Planetary Science* 53, 687–725. <https://doi.org/10.1111/maps.13001>
- Palumbo, A.M., Head, J.W., Wordsworth, R.D., 2018. Late Noachian Icy Highlands climate model: Exploring the possibility of transient melting and fluvial/lacustrine activity through peak annual and seasonal temperatures. *Icarus* 300, 261–286. <https://doi.org/10.1016/j.icarus.2017.09.007>
- Pens, M., Andreani, M., Daniel, I., Perrillat, J.-P., Cardon, H., 2016. Contrasted effect of aluminum on the serpentinization rate of olivine and orthopyroxene under hydrothermal conditions. *Chemical Geology* 441, 256–264. <https://doi.org/10.1016/j.chemgeo.2016.08.007>
- Poulet, F., Bibring, J.-P., Mustard, J.F., Gendrin, A., Mangold, N., Langevin, Y., Arvidson, R.E., Gondet, B., Gomez, C., 2005. Phyllosilicates on Mars and implications for early martian climate. *Nature* 438, 623–627. <https://doi.org/10.1038/nature04274>

- Putzig, N.E., Mellon, M.T., 2007. Apparent thermal inertia and the surface heterogeneity of Mars. *Icarus* 191, 68–94. <https://doi.org/10.1016/j.icarus.2007.05.013>
- Quinn, D.P., Ehlmann, B.L., 2019. The Deposition and Alteration History of the Northeast Syrtis Major Layered Sulfates. *Journal of Geophysical Research: Planets* 124, 1743–1782. <https://doi.org/10.1029/2018JE005706>
- Rampe, E.B., Ming, D.W., Blake, D.F., Bristow, T.F., Chipera, S.J., Grotzinger, J.P., Morris, R.V., Morrison, S.M., Vaniman, D.T., Yen, A.S., Achilles, C.N., Craig, P.I., Des Marais, D.J., Downs, R.T., Farmer, J.D., Fendrich, K.V., Gellert, R., Hazen, R.M., Kah, L.C., Morookian, J.M., Peretyazhko, T.S., Sarrazin, P., Treiman, A.H., Berger, J.A., Eigenbrode, J., Fairén, A.G., Forni, O., Gupta, S., Hurowitz, J.A., Lanza, N.L., Schmidt, M.E., Siebach, K., Sutter, B., Thompson, L.M., 2017. Mineralogy of an ancient lacustrine mudstone succession from the Murray formation, Gale crater, Mars. *Earth and Planetary Science Letters* 471, 172–185. <https://doi.org/10.1016/j.epsl.2017.04.021>
- Rapin, W., Dromart, G., Rubin, D., Deit, L.L., Mangold, N., Edgar, L.A., Gasnault, O., Herkenhoff, K., Le Mouélic, S., Anderson, R.B., Maurice, S., Fox, V., Ehlmann, B.L., Dickson, J.L., Wiens, R.C., 2021. Alternating wet and dry depositional environments recorded in the stratigraphy of Mount Sharp at Gale crater, Mars. *Geology* 49, 842–846. <https://doi.org/10.1130/G48519.1>
- Rempfert, K.R., Miller, H.M., Bompard, N., Nothaft, D., Matter, J.M., Kelemen, P., Fierer, N., Templeton, A.S., 2017. Geological and Geochemical Controls on Subsurface Microbial Life in the Samail Ophiolite, Oman. *Front. Microbiol.* 8. <https://doi.org/10.3389/fmicb.2017.00056>
- Rogers, A.D., Warner, N.H., Golombek, M.P., Head, J.W., Cowart, J.C., 2018. Areal Extensive Surface Bedrock Exposures on Mars: Many Are Clastic Rocks, Not Lavas. *Geophysical Research Letters* 45, 1767–1777. <https://doi.org/10.1002/2018GL077030>
- Ruff, S.W., Hamilton, V.E., Rogers, A.D., Edwards, C.S., Horgan, B., 2019. Olivine-Rich, Carbonate-Bearing Ash Deposits Link Jezero and Gusev Craters. *LPI 2775*.
- Ruff, S.W., Niles, P.B., Alfano, F., Clarke, A.B., 2014. Evidence for a Noachian-aged ephemeral lake in Gusev crater, Mars. *Geology* 42, 359–362. <https://doi.org/10.1130/G35508.1>
- Saranathan, A.M., Parente, M., 2021. Adversarial feature learning for improved mineral mapping of CRISM data. *Icarus* 355, 114107. <https://doi.org/10.1016/j.icarus.2020.114107>
- Scheller, E.L., Ehlmann, B.L., 2020. Composition, Stratigraphy, and Geological History of the Noachian Basement Surrounding the Isidis Impact Basin. *Journal of Geophysical Research: Planets* 125, e2019JE006190. <https://doi.org/10.1029/2019JE006190>
- Schon, S.C., Head, J.W., Fassett, C.I., 2012. An overfilled lacustrine system and progradational delta in Jezero crater, Mars: Implications for Noachian climate. *Planetary and Space Science* 67, 28–45. <https://doi.org/10.1016/j.pss.2012.02.003>
- Sholes, S.F., Dickeson, Z.I., Montgomery, D.R., Catling, D.C., 2021. Where are Mars' Hypothesized Ocean Shorelines? Large Lateral and Topographic Offsets Between Different Versions of Paleoshoreline Maps. *Journal of Geophysical Research: Planets* 126, e2020JE006486. <https://doi.org/10.1029/2020JE006486>
- Smith, M.D., Bandfield, J.L., Christensen, P.R., 2000. Separation of atmospheric and surface spectral features in Mars Global Surveyor Thermal Emission Spectrometer (TES) spectra. *Journal of Geophysical Research: Planets* 105, 9589–9607. <https://doi.org/10.1029/1999JE001105>
- Squyres, S.W., Arvidson, R.E., Ruff, S., Gellert, R., Morris, R.V., Ming, D.W., Crumpler, L., Farmer, J.D., Marais, D.J.D., Yen, A., McLennan, S.M., Calvin, W., Bell, J.F., Clark, B.C., Wang, A., McCoy, T.J., Schmidt, M.E., Souza, P.A. de, 2008. Detection of Silica-Rich Deposits on Mars. *Science* 320, 1063–1067. <https://doi.org/10.1126/science.1155429>
- Stack, K.M., Williams, N.R., Calef, F., Sun, V.Z., Williford, K.H., Farley, K.A., Eide, S., Flannery, D., Hughes, C., Jacob, S.R., Kah, L.C., Meyen, F., Molina, A., Nataf, C.Q., Rice, M., Russell, P., Scheller, E.,

- Seeger, C.H., Abbey, W.J., Adler, J.B., Amundsen, H., Anderson, R.B., Angel, S.M., Arana, G., Atkins, J., Barrington, M., Berger, T., Borden, R., Boring, B., Brown, A., Carrier, B.L., Conrad, P., Dypvik, H., Fagents, S.A., Gallegos, Z.E., Garczynski, B., Golder, K., Gomez, F., Goreva, Y., Gupta, S., Hamran, S.-E., Hicks, T., Hinterman, E.D., Horgan, B.N., Hurowitz, J., Johnson, J.R., Lasue, J., Kronyak, R.E., Liu, Y., Madariaga, J.M., Mangold, N., McClean, J., Miklusicak, N., Nunes, D., Rojas, C., Runyon, K., Schmitz, N., Scudder, N., Shaver, E., SooHoo, J., Spaulding, R., Stanish, E., Tamppari, L.K., Tice, M.M., Turenne, N., Willis, P.A., Aileen Yingst, R., 2020. Photogeologic Map of the Perseverance Rover Field Site in Jezero Crater Constructed by the Mars 2020 Science Team. *Space Sci Rev* 216, 127. <https://doi.org/10.1007/s11214-020-00739-x>
- Steele, A., Fries, M.D., Amundsen, H.E.F., Mysen, B.O., Fogel, M.L., Schweizer, M., Boctor, N.Z., 2007. Comprehensive imaging and Raman spectroscopy of carbonate globules from Martian meteorite ALH 84001 and a terrestrial analogue from Svalbard. *Meteoritics & Planetary Science* 42, 1549–1566. <https://doi.org/10.1111/j.1945-5100.2007.tb00590.x>
- Sun, V.Z., Stack, K.M., 2020. Geologic map of Jezero crater and the Nili Planum region, Mars [WWW Document]. URL <https://pubs.er.usgs.gov/publication/sim3464> (accessed 2.12.21).
- Tarnas, J.D., Mustard, J.F., Lin, H., Goudge, T.A., Amador, E.S., Bramble, M.S., Kremer, C.H., Zhang, X., Itoh, Y., Parente, M., 2019. Orbital Identification of Hydrated Silica in Jezero Crater, Mars. *Geophysical Research Letters* 46, 12771–12782. <https://doi.org/10.1029/2019GL085584>
- Tarnas, J.D., Mustard, J.F., Sherwood Lollar, B., Bramble, M.S., Cannon, K.M., Palumbo, A.M., Plesa, A.-C., 2018. Radiolytic H₂ production on Noachian Mars: Implications for habitability and atmospheric warming. *Earth and Planetary Science Letters* 502, 133–145. <https://doi.org/10.1016/j.epsl.2018.09.001>
- Treiman, A.H., Amundsen, H.E.F., Blake, D.F., Bunch, T., 2002. Hydrothermal origin for carbonate globules in Martian meteorite ALH84001: a terrestrial analogue from Spitsbergen (Norway). *Earth and Planetary Science Letters* 204, 323–332. [https://doi.org/10.1016/S0012-821X\(02\)00998-6](https://doi.org/10.1016/S0012-821X(02)00998-6)
- van Berk, W., Fu, Y., 2011. Reproducing hydrogeochemical conditions triggering the formation of carbonate and phyllosilicate alteration mineral assemblages on Mars (Nili Fossae region). *Journal of Geophysical Research: Planets* 116. <https://doi.org/10.1029/2011JE003886>
- Viviano, C.E., Moersch, J.E., McSween, H.Y., 2013. Implications for early hydrothermal environments on Mars through the spectral evidence for carbonation and chloritization reactions in the Nili Fossae region. *Journal of Geophysical Research: Planets* 118, 1858–1872. <https://doi.org/10.1002/jgre.20141>
- Viviano-Beck, C.E., Seelos, F.P., Murchie, S.L., Kahn, E.G., Seelos, K.D., Taylor, H.W., Taylor, K., Ehlmann, B.L., Wiseman, S.M., Mustard, J.F., Morgan, M.F., 2014. Revised CRISM spectral parameters and summary products based on the currently detected mineral diversity on Mars. *Journal of Geophysical Research: Planets* 119, 1403–1431. <https://doi.org/10.1002/2014JE004627>
- Warren, P.H., 1998. Petrologic evidence for low-temperature, possibly flood evaporitic origin of carbonates in the ALH84001 meteorite. *Journal of Geophysical Research: Planets* 103, 16759–16773. <https://doi.org/10.1029/98JE01544>
- Webb, G.E., 1996. Was Phanerozoic reef history controlled by the distribution of non-enzymatically secreted reef carbonates (microbial carbonate and biologically induced cement)? *Sedimentology* 43, 947–971. <https://doi.org/10.1111/j.1365-3091.1996.tb01513.x>
- Werner, S.C., 2008. The early martian evolution—Constraints from basin formation ages. *Icarus* 195, 45–60. <https://doi.org/10.1016/j.icarus.2007.12.008>
- Whiffin, V.S., Paassen, L.A. van, Harkes, M.P., 2007. Microbial Carbonate Precipitation as a Soil Improvement Technique. *Geomicrobiology Journal* 24, 417–423. <https://doi.org/10.1080/01490450701436505>

- Wray, J.J., Murchie, S.L., Bishop, J.L., Ehlmann, B.L., Milliken, R.E., Wilhelm, M.B., Seelos, K.D., Chojnacki, M., 2016. Orbital evidence for more widespread carbonate-bearing rocks on Mars. *Journal of Geophysical Research: Planets* 121, 652–677. <https://doi.org/10.1002/2015JE004972>
- Zamanian, K., Pustovoytov, K., Kuzyakov, Y., 2016. Pedogenic carbonates: Forms and formation processes. *Earth-Science Reviews* 157, 1–17. <https://doi.org/10.1016/j.earscirev.2016.03.003>
- Zastrow, A.M., Glotch, T.D., 2021. Distinct Carbonate Lithologies in Jezero Crater, Mars. *Geophysical Research Letters* 48, e2020GL092365. <https://doi.org/10.1029/2020GL092365>